ROYAUME DU MAROC
Université Mohammed V - RABAT -
جامعة محمد الخامس – الرباط –
Faculté des sciences
كلية العلوم
CENTRE D'ETUDES DOCTORALES - SCIENCES ET TECHNOLOGIES

N° of order: 3589

THESIS

In order to obtain: ***Doctorate degree***

Research structure: *Laboratory of condensed matter and interdisciplinary sciences*
Discipline: *Physics*
Specialty: *Materials science and modeling of energy systems*

Presented and defended on 15/01/2022 :

Nora BAAALLA

Organic-inorganic hybrid materials and transition metal oxide materials for photovoltaic and optoelectronic applications.

JURY

Mohammed LOULIDI	PES, Faculty of sciences, Mohammed V University in Rabat.	President / Reviewer
Abdellah REZZOUK	PES, Faculty of sciences Dhar El Mahraz, Sidi Mohammed Ben Abdellah University– Fès.	Reviewer
Hamid EZ-ZAHRAOUY	PES, Faculty of sciences, Mohammed V University in Rabat.	Reviewer
Najib BENZAKOUR	PES, Faculty of sciences Dhar El Mahraz, Sidi Mohammed Ben Abdellah University– Fès.	Examiner
Abdelilah BENYOUSSEF	PES, Hassan II academy of sciences and techniques, Rabat.	Expert
El-Kebir HLIL	PES, CNRS, Néel Institute, Grenoble Alpes University, France.	Examiner / Thesis co-director
Rachid MASROUR	PH, Faculty of sciences Dhar El Mahraz, Sidi Mohammed Ben Abdellah University– Fès.	Examiner /Thesis co-director
Abdallah EL KENZ	PES, Faculty of sciences, Mohammed V University in Rabat.	Thesis Director

Academic year: 2021/2022

Acknowledgements

This thesis work has been carried out at the laboratory of Condensed Matter and Interdisciplinary Sciences (LaMCScI) of the Faculty of Science, Mohammed V University Rabat, under the supervision of professor Abdallah El Kenz, from Mohammed V University in Rabat - Faculty of Science in a collaboration with other professors who have greatly contributed to my work and enriched my life. However, this work would not be possible without support of many people.

First and foremost praises and thanks go to Allah, the almighty, for his unlimited and uncountable blessings in my whole life and throughout my research work especially.
I would like to express my deep acknowledgment to my supervisor professor Abdallah El Kenz for giving me his advices, and full support in making my PhD research possible and successful. I have the privilege to learn so much knowledge and skills from his guidance.

My sincere thanks go to professor El-Kebir Hlil, from Grenoble university, and researcher at Institut Néel CNRS, Alpes - France for his idea to work with different and complicated structures, and trying new concepts that finally leaded to the creation of an original works. His encouraging comments, and beneficial suggestions during our discussions, his guidance and methodology in working, his excellent assistance to give me positive energy during my bad days, without his constant care and understanding. Honestly, my research would not have been possible. I'll never forget the time you gave me, and I've been most fortunate to be your student.

Sincere thanks and gratitude to Professor Rachid Masrour, from Sidi Mohammed Ben Abdellah University - Fès, for his useful critiques to value my thesis, and his help in my first step to make my computations easier and accessible. And his availability each time I need help.

I would like also to show my greatest appreciation to Professor Abdelilah Benyoussef expert from Hassan II Academy of sciences and techniques of Rabat, for his scientific discussion in order to enrich my work, your professionalism professor deserves a respect.

I am deeply indebted to my collaborator Doctor Yassine Ammari, from Carthage university, Faculty of Science Bizert, Tunisia, for his professional and constructive remarks on our work, his remarks pushed me to reach a higher level than would otherwise have been possible.

I would also like to thank the thesis committee for reviewing my thesis and for giving me their useful suggestions. Foremost, I would like to thank my Professor Mohammed Loulidi, from Mohammed V University in Rabat - Faculty of Science, chairman of this jury.

I would also like to offer my thanks to the reviewers of this thesis, namely; Professor Abdellah REZZOUK, from Sidi Mohammed Ben Abdellah University - Fès, for having agreed to report this thesis work.

My deepest gratitude for Professor Hamid Ez-Zahraouy, from Mohammed V University in Rabat - Faculty of Science, for having accepted to report this thesis work.

I also would like to thank Professor Najib Benzakour, from Sidi Mohammed Ben Abdellah University - Fès, for his pertinent remarks and for having also agreed to examine and this thesis.

During my years in PhD, I fortunately have a lot of nice colleagues from the laboratory (LaMCScI). I wish to express my thanks to Dr. Rachida Lamouri, Dr. Hanan Absike, Khadija Daoudi, Dr. Ismael Benabdellah and Dr. Naima Enassiri. We discussed a lot of kind of subjects and we exchanged feelings and thoughts, and I will not forget the numerous activities we had together and the moments we shared. All these interesting memories will remain in my mind for as long as I live.

For technical support I would like to thank Ayoub El Mouzazi, Wafae Anana, Smahane Dahbi, Iliyas Haidouri, for the moral support and their encouragement throughout my PhD candidature. At Last, I would like to express my immense love and gratitude to my mother Amina BAALA, and my father Idriss BAAALLA, and my sisters, Fatima-zahrae, Khadija, and Maroua for their love and care. They give kind advices, trust me all the time, encourage me no matter what decision I made in life. Nothing of this would be possible without you.

Abstract

Organic-inorganic hybrid materials and transition metal oxide materials have attracted intensive interest due to their multifunctional properties. This present thesis work was focused on well-understanding the different properties of these materials. We have explored the possibilities of organic-inorganic hybrids and transition metal oxide materials for diverse applications such as photovoltaics and optoelectronic devices. Those materials could be of interest for applications in cheap and printable single-use electronics that require both data storage and data processing. Moreover, this combination of unique parameters is rarely observed in conventional materials and is, therefore, also from a fundamental point of view, an interesting place to start the exploration of the field of organic-inorganic hybrids and transition metal materials.

This thesis is of scientific interest and considers a study of the correlation between the electronic structure of materials and their efficiency in a photovoltaic device. By calculating the open-circuit voltage Voc and the short circuit current Jsc with the density functional theory. This new method opens the possibility to rapidly estimate the efficiency of a given material without the necessity to realize a photovoltaic device as well as to optimize the size of an already existing photovoltaic device.

The first part of this thesis deals with the modeling of the structural, electronic, and optical properties of hybrid organic-inorganic materials. The calculations are based on the ab-initio method within the framework of the density functional (DFT) implemented in the WIEN2K code. The results found are in agreement with the experimental measurements. This demonstrates that these materials are promising in optoelectronic and photovoltaic applications.

The objective of the second part of this thesis is to study the electronic, optical, magnetic and thermoelectric properties of sodium manganese (II) arsenate $NaMnAsO_4$ using DFT. The density of state, as well as the band structure calculation, revealed that the studied material can be identified as a ferromagnetic semiconductor. Optical properties show that $NaMnAsO_4$ has potential application in optoelectronics. The electrical conductivity obtained as well as the figure of merit suggests that this material could be new potential for an optoelectronic-thermoelectric device.

Keywords: Organic- Inorganic hybrid, Transition metal TM-oxide, DFT, electronic and optical properties, thermoelectrical properties, DFT, BoltzTraP.

Résumé

Les matériaux hybrides organiques-inorganiques et les oxydes de métal de transition ont suscité un vif intérêt en raison de leurs propriétés multifonctionnelles. Ce présent travail de thèse s'est concentré sur la compréhension des différentes propriétés de ces matériaux. Nous avons exploré les possibilités des hybrides organiques-inorganiques et des matériaux d'oxyde de métaux de transition pour diverses applications telles que le photovoltaïque et les dispositifs optoélectroniques. Ces matériaux pourraient être intéressants pour des applications dans des appareils électroniques à usage unique et imprimables qui nécessitent à la fois le stockage et le traitement de données. De plus, cette combinaison de paramètres est rarement observée dans les matériaux conventionnels, et constitue donc d'un point de vue fondamental également, un point de départ pour commencer l'exploration du domaine des hybrides organiques-inorganiques et des matériaux de métaux de transition.

Cette thèse est d'intérêt scientifique et envisage une étude de la corrélation entre la structure électronique des matériaux et leur efficacité dans un dispositif photovoltaïque. En calculant la tension en circuit ouvert V_{oc} et le courant de court-circuit J_{sc} avec la théorie fonctionnelle de la densité. Cette nouvelle méthode ouvre la possibilité d'estimer rapidement l'efficacité d'un matériau donné sans qu'il soit nécessaire de réaliser un dispositif photovoltaïque ainsi que d'optimiser la taille d'un dispositif photovoltaïque déjà existant.

La première partie de cette thèse porte sur la modélisation des propriétés structurales, électroniques et optiques de matériaux hybrides organiques-inorganiques. Les calculs sont basés sur la méthode ab-initio dans le cadre de la fonctionnelle de densité (DFT) implémentée dans le code WIEN2K. Les résultats trouvés sont en accord avec les mesures expérimentales. Cela démontre que ces matériaux sont prometteurs dans les applications optoélectroniques et photovoltaïques.

L'objectif de la deuxième partie de cette thèse est d'étudier les propriétés électroniques, optiques, magnétiques et thermoélectriques de l'arséniate de sodium manganèse (II) $NaMnAsO_4$ à l'aide de la DFT. La densité d'état, ainsi que le calcul de la structure de bande, ont révélé que le matériau étudié peut être identifié comme un semi-conducteur ferromagnétique. Les propriétés optiques montrent que $NaMnAsO_4$ a une application potentielle en optoélectronique. La conductivité électrique obtenue ainsi que le facteur de mérite suggèrent que ce matériau pourrait être un nouveau potentiel pour un dispositif optoélectronique-thermoélectrique.

Mots clés : Les matériaux Hybride organiques-inorganiques, les matériaux d'oxyde de métal de transition, DFT, propriétés électroniques, propriétés optiques, propriétés thermoélectriques, BoltzTraP.

Résumé détaillé

Cette thèse s'intéresse à l'étude de différentes propriétés des matériaux hybrides organiques-inorganiques et les matériaux d'oxyde de métal de transition, qui ont suscité un vif intérêt en raison de leurs propriétés multifonctionnelles. Ce présent travail de thèse s'est concentré sur la bonne compréhension des différentes propriétés de ces matériaux. Nous avons exploré les possibilités des hybrides organiques-inorganiques et des matériaux d'oxyde de métaux de transition pour diverses applications telles que le photovoltaïque et les dispositifs opto-électroniques. Ces matériaux pourraient être intéressants pour le marché des applications dans l'électronique à usage unique et imprimable qui nécessitent à la fois le stockage et le traitement des données. En outre, cette combinaison de paramètres uniques est rarement observée dans les matériaux conventionnels, nous a donné l'envie d'explorer ces types de matériaux de point de vie fondamental.

Un intérêt particulier a été porté dans la première partie de cette thèse, à la pérovskite $CH_3NH_3PbI_3$ grâce à son efficacité et le nombre des articles scientifiques publiés sur ce derniers. Son choix comme référence a été très important pour valider notre méthode de calcul. Notre calcul a été focalisé sur la corrélation entre la structure électronique du matériau $CH_3NH_3PbI_3$ et son efficacité dans un dispositif photovoltaïque, en calculant la tension en circuit ouvert V_{oc} et le courant de court-circuit J_{sc} avec la théorie fonctionnelle de la densité. Cette méthode ouvre la possibilité d'estimer rapidement l'efficacité d'un matériau donné sans réaliser le dispositif photovoltaïque. Cette méthode permet également, d'optimiser la taille d'un dispositif photovoltaïque déjà existant.

Les calculs ab initio ont été aussi effectués afin d'étudier les propriétés électroniques et optiques du nouveau matériau organique-inorganique hybride $(C_6H_{10}N_2)_2[Co(H_2O)_4P_2Mo_5O_{23}].6H_2O$. Les valeurs des paramètres de réseau ont été obtenus en utilisant la diffraction des rayons X (XRD). Nos résultats montrent que la bande interdite théorique de ce matériau est de 1.8 eV, cela est en bon accord avec les résultats expérimentaux. Une analyse de densité d'état a montré que la contribution la plus élevée provient de l'orbital 3d de l'atome de Co.

La corrélation entre le gap expérimental et le gap calculé avec la DFT pour le complexe trans-[Cu(L-Arg)$_2$(ReO_4)$_2$] (CuLARe) révèle que le coefficient est plus important dans la direction xx, indiquant que ce complexe est un bon candidat pour les applications optoélectroniques.

La densité d'états montre que le complexe trans-[Cu(L-Arg)$_2$(ReO_4)$_2$], (CuLARe), présente un comportement magnétique, dû à la présence d'atomes de Cu. La structure de bande pour le spin majeur et mineur confirme la transition indirecte pour le matériau CuLARe. La bande interdite expérimentale estimée à partir de la réflectance mesurée à l'aide de l'équation de Tauc est conforme à la bande interdite calculée théoriquement. De plus, sur la base de l'approche semi-empirique de Kubelka-Munk, le coefficient de diffusion de transport S est estimé pour les directions xx et zz respectivement. Les résultats obtenus montrent le potentiel de ce matériau comme candidat prometteur pour les dispositifs optoélectroniques.

Les propriétés électroniques, optiques, magnétiques et thermoélectriques des phases monoclinique et orthorhombique de l'agrégat $NaMnAsO_4$ d'arséniate de sodium et de manganèse (II) sont étudiées. Les approches GGA et GGA+U ont été réalisées par le logiciel Wien2k. La polarisation de spin est incluse dans les calculs pour étudier les propriétés électroniques et magnétiques de ce matériau pour les deux phases monoclinique et orthorhombique. La densité d'état, outre le calcul de structure de bande, a révélé que le matériau étudié peut être identifié comme un semi-conducteur ferromagnétique avec une énergie de bandes interdites optiques qui varient de 1,53 eV à 0.83 eV respectivement 1.27 eV et 1.59 eV pour les deux phases monoclinique et orthorhombique avec l'approche GGA, respectivement avec l'approche GGA+U. Les propriétés optiques telles que le coefficient d'absorption, la fonction diélectrique et la réflectivité montrent que $NaMnAsO_4$ a une application potentielle dans l'optoélectronique. Les propriétés thermoélectriques des deux structures ont également été étudiées à l'aide du package BoltzTraP. La conductivité électrique obtenue, ainsi que le facteur de mérite, suggèrent que $NaMnAsO_4$ pourrait ouvrir la voie à de nouvelles recherches expérimentales sur les applications optoélectroniques-thermoélectriques.

List of Publications

Articles on the topic of the thesis:

1- **Baaalla, N**., Ammari, Y., Hlil, E. K., Masrour, R., El Kenz, A., & Benyoussef, A. (2020). Study of optical, electrical and photovoltaic properties of CH3NH3PbI3 perovskite: ab initio calculations. *Physica Scripta*, *95*(9), 095104.

2- **Baaalla, N**., Ammari, Y., Hlil, E. K., Abid, S., Masrour, R., Benyoussef, A., & El Kenz, A. (2021). The novel material based on strandberg-type hybrid complex (C6H10N2)2[Co(H2O)4P2Mo5O23]. 6H2O: Experimental and simulations investigation on electronic, optical, and magnetocaloric properties. *Ceramics International*, *47*(2), 2338-2346.

3- **Baaalla, N**., Hemissi, H., Hlil, E. K., Masrour, R., Benyoussef, A., & El Kenz, A. (2021). Electronic and optical properties of organic-inorganic (CuII/ReVII)-heterobimetallic L-Arginine complex: Experimental and Computational studies. *Journal of Molecular Structure*, *1246*, 131153.

4- **Baaalla, N**., Absike, H., Ammari, Y., Hlil, E. K., Masrour, R., El Kenz, A., & Benyoussef, A. An extensive investigation of structural, electronic, optical, magnetic, and thermoelectric properties of $NaMnAsO_4$ cluster by first-principles calculations. *International Journal of Energy Research* **(Under Review).**

Articles in collaboration:

5- Ammari, Y**., Baaalla, N**., Hlil, E. K., & Abid, S. (2020). Structure, optical and magnetic properties of a novel homometallic coordination polymers: Experimental and Computational studies. *Scientific reports*, *10*(1), 1-12.

6- Absike, H., Essalhi, Z., Labrim, H., Hartiti, B., **Baaalla, N**., Tahiri, M., ... & Ez-zahraouy, H. (2021). Synthesis of CuO thin films based on Taguchi design for solar absorber. *Optical Materials*, *118*, 111224.

7- Absike, H., **Baaalla, N**., Attou, L., Labrim, H., Hartiti, B., & Ez-zahraouy, H. (2022). Theoretical investigations of structural, electronic, optical and thermoelectric properties of oxide halide perovskite ACoO3 (A= Nd, Pr or La). *Solid State Communications*, 114684.

8- Absike, H., **Baaalla, N**., Lamouri, R, Labrim, H., Ez-zahraouy, H. "Optoelectronic and photovoltaic properties of Cs_2AgBiX_6 (X = Br, Cl or I) halide double perovskite for solar cells: insight from DFT". *International Journal of Energy Research* **(Under Review).**

9- **Baaalla, N**., Absike, H., Hlil, E. K., Masrour, R., El Kenz, A., & Benyoussef, A. First-principles study of structural, electronic, optical, and thermoelectrical properties of new quadruple perovskite $Ag_2Mo_3SeO_{12}$. *journal of optical materials* **(submitted).**

10- Ammari, Y., **Baaalla, N.,** Abid, S., Hlil, E. K., Structure and magneto-optical studies of trivial and non-trivial properties of novel 2D POMs based material. *Journal of Inorganic chemistry*. **(Under Review).**

List of communications

- Poster communication at the 1st IMSEGEC-17 Conference –May 10-12, 2017, Ifran, Morocco.
- Poster communication at the doctoral journey Conference –July 20, 2017, Rabat, Morocco.
- Poster communication at AMT'2018 Conference – April 18-19, 2018, Safi, Morocco
- Poster communication at the 2nd IMSEGEC-18 Conference –April 25-27, 2018, Rabat, Morocco.
- Oral communication at AETEEMS-2018 Conference –December 13-14, 2018, El Jadida, Morocco.
- Poster communication at NANOSMAT MEDITERRANE Conference – May 02-04, 2019, Rabat, Morocco.
- Poster communication at AMPSECA Conference –October/ November 30-01, 2019, Marrakech, Morocco.
- Oral communication at the second annual Inter-lab-LaMCScI-LERMA-meeting – December 11-12, 2019, Rabat, Morocco.
- Poster communication at TRAMP 2019 Conference –November 07-09, 2019, Marrakech, Morocco.
- Oral communication at Nano-TN Conference – February 19-22, 2020, Marrakech, Morocco.

Table of Content

Chapter III: Study of optical, electrical, and photovoltaic properties of $CH_3NH_3PbI_3$ perovskite

Chapter IV: Electronic, optical, and magnetocaloric properties of $(C_6H_{10}N_2)_2[Co(H_2O)_4P_2Mo_5O_{23}].6H_2O$

Chapter V: Electronic, and optical properties of organic-inorganic (Cu^{II} /Re^{VII})-heterobimetallic L-Arginine complex

Chapter VI: The structural, electronic, optical, magnetic, and thermoelectric properties of $NaMnAsO_4$ cluster

List of figures

List of tables

List of Abbreviations

AM: Air Mass

APW: Augmented-Plane-Wave

BHJ : Bulk-heterojunction

c : Speed of light

CMOS: Complementary metal oxide semiconductor

DFT: Density Functional Theory

DSSCs : Dye-sensitized solar cells

e : Elementary charge

EQE : External Quantum Efficiency

FF : Fill Factor

FP-LAPW: Full Potential Linearized-Augmented-Plane-Wave

GGA: Generalized Gradient Approximation

GWp : Global warming potential

h : Planck constant

IPCE : Incident Photon to Current Efficiency

ISI: Institute for Scientific Information

ISMs: Inorganic semiconductor materials

J : Current

J_{SC}: Short-circuit current

k_B : Boltzmann constant.

KS: Khon Sham

L : Length of the light traveled across the atmosphere

L_0 : Length of the light that would travel normal to the surface of the earth at sea level.

LAPW: Linearized-Augmented-Plane-Wave

LSDA: Local Spin Density Approximation

M_{pp} : Maximum power point

MT: Muffin-Tin

OLED: Organic light-emitting diodes

OPV : Organic photovoltaics

OSMs: Organic semiconductor materials

PBE: Perdew-Bruker-Ernzerhof

PCE : Power Conversion Efficiency

P_{in} : Power input

P_{out}: Power output

PSCs: Perovskite solar cells.

PV: Photovoltaic

RRAM: Resistive random-access memory

SCF: self-consistent field

SMs: Semiconductors

SPE : Solar Power Europe

T: Temperature

TMOs: Transition metal oxides

V : voltage

VCSELs: Vertical-cavity surface-emitting lasers

V_{OC}: Open-circuit voltage

Wh: Watt-hours

λ: Wavelength

General introduction

The demand for energy is increasing globally. A rise of 60% in world energy demand is expected by 2030 [1-3]. In parallel with this, CO_2 emissions are increasing as a result of human activities and our climate is getting warmer. The Intergovernmental Panel on Climate Change predicts there will be an increase in temperature of between 1.8°C and 4.0°C by the end of the century if no action is taken [4]. This temperature increase is extremely likely to have vast effects, including sea levels rising by 18−59 cm and an increased intensity of tropical storms [5,6]. The technology of photovoltaics, whereby energy from the sun is converted into electricity, offers the possibility of a clean source of electricity without the pollution concerns of gas or coal-fired power stations, or the safety concerns associated with nuclear energy. However, the excessive cost of conventional solar cells based on inorganic semi-conductors has prohibited this technology from having a significant impact on global energy production. Although crystalline silicon and multijunction gallium based solar cells have demonstrated efficiencies of up to 25% and 32% respectively [7], commercially available silicon solar cells have efficiencies from 12% to 15%. Fabrication of such devices is expensive, and the payback time can be up to a decade [8-10]. Thus, an important research area is the development of new materials for solar cells. Ideally these materials will lead to devices which are cheaper to fabricate and require less energy to produce than silicon solar cells. Photovoltaic technology would be of particular interest if the cost per unit of power produced were reduced significantly. The ideal photovoltaic material would be abundant, inexpensive, easily processed, thermally nonconductive, electrically conductive, durable, and nonreactive. The photovoltaic and optoelectronic properties of materials can be improved through a variety of other strategies, including doping, solution processing, morphology control, nano-structuring, and production of new organic-inorganic hybrid and transition metal oxide materials. Traditionally, inorganic materials have been used for photovoltaics and optoelectronics, but they are costly, rare, toxic,

and brittle, as well as highly thermally conductive. Organic materials tend to be abundant, inexpensive, easily tuned and processed, as well as thermally nonconductive, though they usually have poor electrical conductivities, yielding lower power production compared to inorganic thermoelectric materials. Organic-inorganic hybrid materials offer the unique opportunity to combine desirable properties of both classes of compounds, as well as properties that may not exist in either material. Hybrid materials may yield inexpensive, low-toxicity, tunable, processable, thermally non-conductive, electrically conductive, flexible, and durable material that is desired for these applications. Besides, the unusual properties of transition metal oxide materials are clearly due to the unique nature of the d-states of the metal atoms, which make them a fascinating materials for different applications.

In this thesis, I will concentrate on the study of the organic-inorganic hybrid and the transition metal oxide materials for photovoltaic and optoelectronic applications, and the development of a new method to calculate a requested parameter by the industry using ab initio outputs, to target experimental research.

Chapter I:
State of the Art

I.1 Introduction

This introductory chapter provides a general overview of solar cells history and a general look at a promising material that can be used for photovoltaic applications and optoelectronic devices fabrication. First, a short history of the utilization of the solar cells over the years, and solar cells technologies are described, followed by outlining the notable achievements of the organic-inorganic hybrid materials including perovskite materials for the optical and photovoltaic technologies. Then a small review of the transition metal oxide. Additionally, the exceptional optoelectronic properties of this class of materials. Finally, an outline of the thesis is provided.

I.2 Solar Energy

Solar energy is one of the most abundant clean energy sources. The same energy that is currently contributing to the heating effect on the planet could generate a large amount of clean and renewable energy. On average, around 1 zetta watt-hours (Wh) of energy per year (1 billion TWh) falls onto the surface of the planet; humanity needs about 100.000 TWh, which mean that we will expand almost 10.000 times before needing another resource [11].

This provides the upper limit when a significant portion of this energy is used into driving the natural processes around us: providing nature with the energy it needs, heating our oceans, and growing our food supplies. Despite this being an extreme upper limit, it is amazing how much energy is accessible to humanity purely from solar processes.

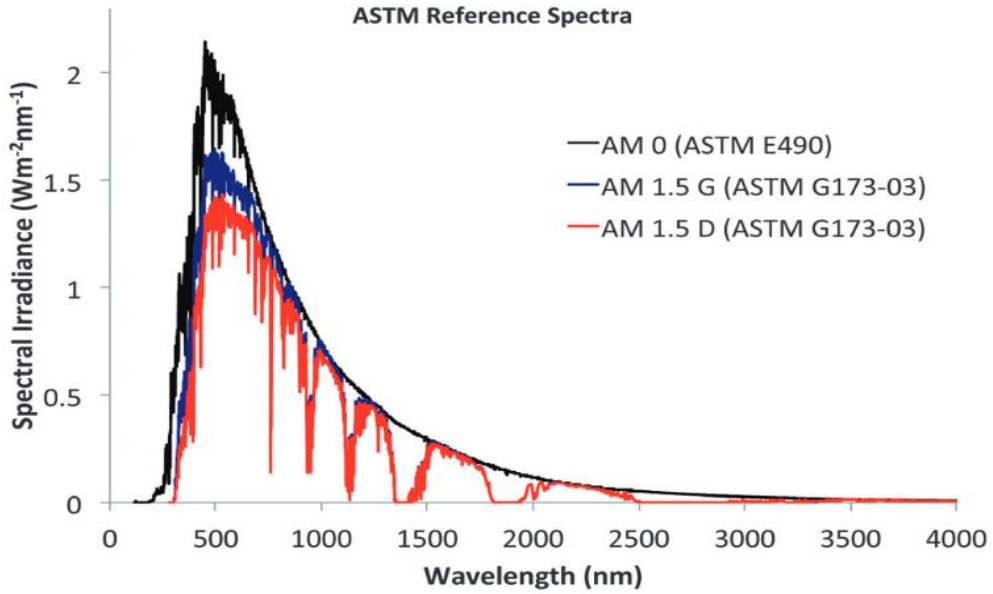

Figure I-1: AM 0 (black), AM 1.5 G (blue), and AM 1.5 D (red) solar spectra [12].

Unfortunately, solar power is not an ideal energy source. As shown in Figure. I.1, the energy delivered to the earth is spectrally dependent. This means that the solar spectrum has its energy distributed over a range of wavelengths. Classically we can approximate this distribution as perfect blackbody radiation, employing the energy of the incoming photons follows:

$$E_\lambda(\lambda, T) = \frac{2hc^2}{\lambda^5} \frac{1}{e^{\frac{hc}{\lambda k_B T}} - 1} \qquad (1)$$

Where E is the wavelength dependent energy, λ is the wavelength, T is the temperature of the emitter, h is the Planck constant, c is the speed of light in the medium (here vacuum), and k_B is the Boltzmann constant. Named Planck's law, this equation defines the energy of a photon with a given wavelength generated by the emitter at a known temperature. For our sun, if it were a perfect blackbody emitter, we could treat it as a black body with a temperature of 5777K. However, the actual distribution deviates from this significantly, as the emissions depend on the atomistic make-up of the sun. We see a further deviation from this as the solar flux interacts with the atmosphere. Because of this, we generally rely on the reference spectrum called the air-mass 1.5 (AM1.5) index. The definition of air-mass is:

$$AM = \frac{L}{L_0} \qquad (2)$$

Where L is the length of the light traveled across the atmosphere and L_0 is the length of the light that would travel normal to the surface of the earth at sea level. More precisely, AM1.5 is the spectrum that the majority of ground-level observers will see. This spectrum gives researchers a clear understanding of the energetic makeup of photons that make it to the terrestrial level. Both the black body radiation and the actual solar spectrum are seen in Figure. I.1. Examination of this figure reveals that a significant amount of energy is lost before the possible point of capture.

There are two main methods for transforming this energy spectrum into usable work: solar thermal and solar photovoltaic (PV). In this thesis, we are focused on promising materials for solar photovoltaic application.

I.3 The utilization of the solar cells over the years

Solar cells use semiconductor materials to convert sunlight directly into electricity through the photovoltaic (PV) effect. Despite the fact that PV installation has increased significantly in recent years, with total power installed capacity in the world reaching 233GWp

by the end of 2015 [13] and will be between 396-540 GW_p by the end of 2019 [14] (Figure I.2). The growth of photovoltaic technologies has been long and irregular. In the following sections, a short historical overview of PV technologies will be presented.

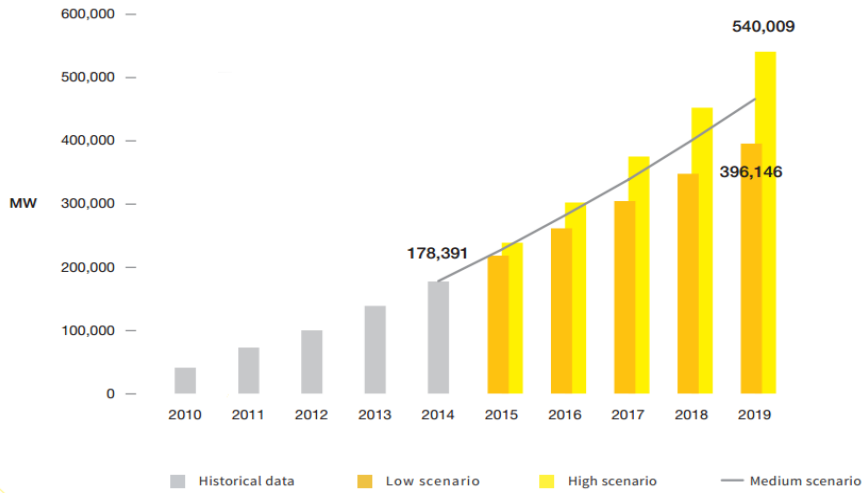

Figure I-2: World solar PV cumulative market scenarios until 2019. Source: Solar Power Europe (SPE) [14].

The photovoltaic effect was discovered by A. E. Becquerel in 1839 where silver halides coated electrodes improved the generated current in the presence of blue and violet light [15]. W.G. Adams and R.E. Day both observed the generation of a current between two platinum wires connected at the edges of a vitreous selenium cylinder in 1877 [16], i.e. The first demonstration of the PV effect in a solid-state device. A. Mouchot demonstrated the first solar power generator at the Universal Exhibition in Paris in 1878.

In 1883, C. Fritts was able to fabricate a thin film solar cell by sandwiching 25-125 µm of Se between a metal and a gold leaf manually pressed to the Se surface [17]. Despite the fact that these Se thin film PV prototypes were (<1% Power Conversion Efficiency, PCE), it is worth to mention the overall configuration was quite similar to the current silicon solar cell technology. C. Fritts was the first to demonstrate the capabilities of this field, describing the use of low-cost materials and processes, as well as power storage, as critical points for the future growth of these technologies [18], being both topics are still essential nowadays.

After several decades, a revival in PV technologies occurred in the early 1930s as a result of copper-cuprous oxide junctions (Cu-Cu_2O). For this junction couple, nearly 40 scientific works were reported in Grondahl's review in 1933 [19]. A typical configuration of the original Cu-Cu_2O photovoltaic cells consisted of cuprous oxide grown over metallic copper; a Pb wire was pressed to cuprous oxide with a glass plate [18]. For the first time, a transparent side in a layered architecture was described to allow the light to come into the cell.

Taking advantage of the Cu-Cu_2O impulse, solar cells based on selenium were investigated and improved, converting in the dominant variety of photovoltaics those days [20]. During that decade, more precisely in 1832, the PV effect in Cadmium selenide (CdSe) was demonstrated by Audobert and Stora. In 1839, Nix and Treptwo reported thallous sulphide (Tl2S) as a semiconductor for photovoltaic devices [21].

I.4 Photovoltaic and solar cells technologies

I.4.1 Inorganic solar cells

The technology used to fabricate the majority of the solar cells produced thus far is highly influenced by the microelectronics industry, where silicon is the dominant semiconductor. The first silicon solar cell was developed by the Bell Telephone Lab in 1954, showing efficiency of 6% [22].

Because silicon is a safe element and the second most abundant element on Earth, much study has been conducted. First generation solar cells are crystalline solar cells, either monocrystalline or polycrystalline. Their maximum efficiencies, 25.0% and 20.4% (Figure.I.3, SunPower, Solibro), respectively, are close to the Shockley–Queisser theoretical limit, *i.e.* 33% [23].

Despite the fact that crystalline silicon solar cells dominate the photovoltaic market, one significant disadvantage of this type of photovoltaic cell is the difficulty in obtaining pure silicon. The high production costs of such modules inspired engineers and scientists to look for 2nd generation solar cells that addressed factors such as simple and low-cost production as well as high performance.

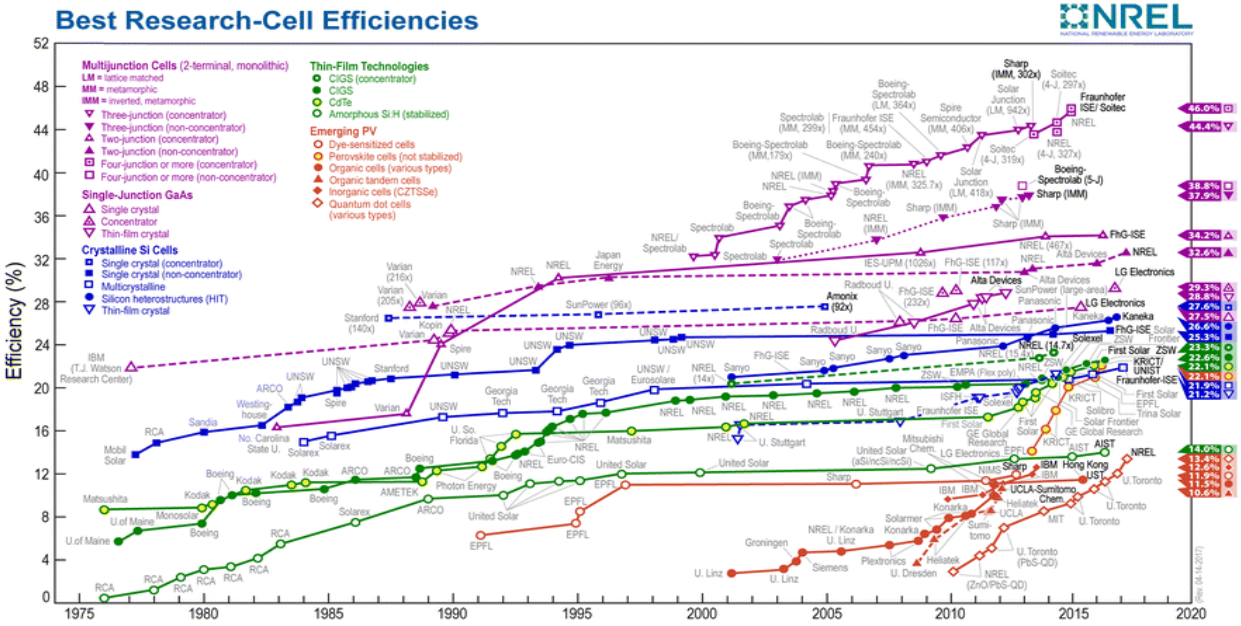

Figure I-3: Historical trends in cell efficiency for different photovoltaic technologies (this plot is courtesy of the National Renewable Energy Laboratory, Golden, CO, USA).

2nd generation, thin film inorganic solar cells appeared in the early 60s (although they did not raise too much expectations until the 90s), as a result of the growth of cost-efficient thin film technologies [24]. Nowadays they have proved to be a strong alternative to classical silicon photovoltaics. Modules based primarily on chemical vapor deposited amorphous silicon (maximum efficiency of 13.4%, Figure 3, LG Electronics), as well as polycrystalline InSe, CdTe (maximum efficiency of 21.5%, Figure. I.3, First Solar), CuInGaSe2 (known as CIGS) (maximum efficiency of 21.7%, Figure. I.3, ZSW) have yielded outstanding performances. They are less efficient, but also less costly when compared to 1st generation solar cells. Thin film solar cells are intended to use less material, resulting in less expensive manufacturing processes. Some disadvantages, such as resource scarcity and the toxicity of active materials, prompted studies on 3rd generation solar cells over the last two decades.

Highly effective solar cells of the latter generation are made from environmentally friendly materials, allowing for low-cost solvent-based fabrication methods. Low-cost, thin-film solar cells based on novel concepts such as hot carrier solar cells, multiple exciton generation, tandem or multijunction solar cells are prime examples [25].
The Shockley-Queisser limit, which was specified for first generation solar cells, is predicted to be bypassed by these cells [26].

I.4.2 Organic solar cells

All-organic photovoltaics and hybrid solar cells are also called 3rd generation devices because of their low cost, stability, ease of fabrication, and versatility [27-30]. Many common dyes, such as methylene blue, as well as many essential biological molecules such as carotenes and chlorophylls, as well as other porphyrins and related synthetic analogues such as phthalocyanines, were found to have semiconducting properties in the late 1950s and early 1960s. These dyes were among the first organic materials to demonstrate photovoltaic properties. Kearns et al. noted the photovoltaic effect of a cell based on a single layer (Schottky or monolayer solar cell) of magnesium phthalocyanine with a photovoltage of 200 mV as early as 1958 [30].

Since then, organic materials have gained the public's interest and several new concepts related to the configuration of the device have been presented Tang used a two-component, donor/acceptor active layer (planar bilayer heterojunction, PHJ, or p-n solar cell, Figure I.4a)

in 1986 [31]. This structural modification benefits from the facile formation of the charge carriers (electrons and holes) by electron transfer from the photoexcited donor to the acceptor component. Furthermore, the separated charge transport layers guarantee connectivity with the correct electrode while giving separated charge carriers only a small chance of recombining with their counterparts. The drawback is that only excitons (electron-hole pairs formed by light excitation) formed very close to the interface between donor and acceptor layers are able to dissociate. Yu et al, presented the concept of bulk-heterojunction (BHJ, Figure I.4b) to overcome this structural problem, in which a mix of a donor and an acceptor with a bi-continual phase separation is created [32-34]. The large interface area of this type of cell is advantageous if molecular mixing happens on a scale that makes for excellent contact between materials and allows most excitons to reach the p-n interface. Ultimately, another type of architectures called tandem solar cells (Figure I.4c), has received a lot of attention. They consist of a combination of two or more single junction cells (one on top of the other) that absorb in diverse wavelength ranges. Their advantage is that a combination of absorbing molecules can provide for a large spectral coverage with efficient absorption, which is difficult to achieve with a single heterojunction [35-42].

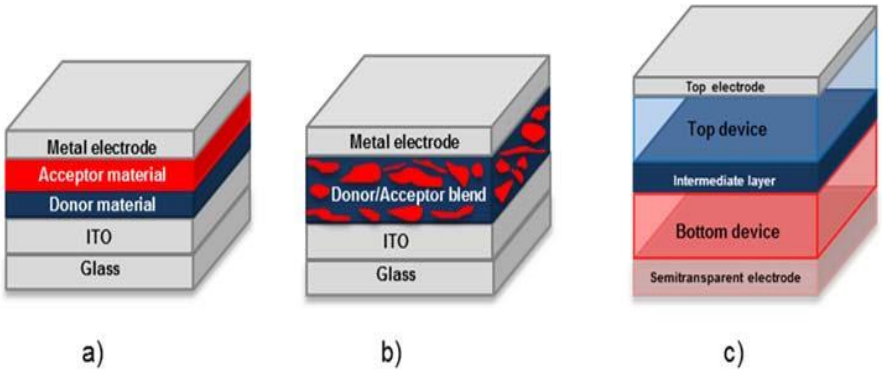

Figure I-4: Schematic representation of a) planar bilayer, b) bulk heterojunction and c) tandem solar cell.

From a different point of view, another classification of the organic solar cells based on the active material can be established: polymer-based photovoltaic cells, also known as plastic solar cells[43-47]**,** which are constituted by conjugated polymers; and small molecule-based photovoltaic devices, in which discrete chromophores form the active layer [48-56]. While polymeric tandem solar cells have achieved a conversion efficiency of 10.6 % (Figure I.3, UCLA-Sumitomo Chem.) [57], it is worth noting that Heliatek holds the record in multi-junction architectures [58], having recently reported a tandem oligomer-based device with a

verified power conversion efficiency of 12 %. Mitsubishi Chemical achieved the highest conversion efficiency for a single junction device, at a value of 11.7% [59].

I.4.3 Hybrid solar cells

The combinations of organic-inorganic materials have gained popularity in recent years. In this sense, the development of dye-sensitized solar cells (DSSCs) in the 1990s opened up new horizons in photovoltaics and dynamically joined the race for cost-efficient devices operating at the molecular and nanoscale levels [59,60].

In 1991, O'Regan and Grätzel published a seminal paper that introduced a pioneering architecture, an n-type DSSC, in which an organic light-absorbing dye is anchored to a mesoporous inorganic n-type semiconductor film (which acts as a photoanode) and filled with a redox-active electrolyte [62]. This type of DSSCs has demonstrated enormous potential and now is a real alternative to standard silicon photovoltaics, with efficiencies growing from 7% in the seminal report, with the obtained using ruthenium complexes as the dye, to the current 13.0% using porphyrins as sensitizers and removing the need for rare and costly, ruthenium-based sensitizers as a requirement for high efficiencies [63]. Alternatively, p-type DSSCs (an active photocathode) have been investigated, but they have not yet shown energy conversion values comparable to conventional DSSCs. This has been attributed to disadvantages associated with electrolytes and p-type semiconductors, and to date, there is just one example of comparable efficiency, *i.e.*2.51% [64]. Another pertinent point is the current trend toward developing all-solid-state devices rather than liquid-based DSSCs, which constitutes a step forward in future commercialization [65,66].

I.4.4 Solar cells characteristics

Plotting the measured current output J of the cell versus the voltage output V of the cell can be used to classify the properties of photovoltaic devices (J-V graph).
Because no current is flowing through the device and no potential is present in the dark, this J-V curve passes through the origin. When the photovoltaic device is exposed to light, the J-V curve changes downward, as shown in Figure I.5. This J-V curve contains the most significant photovoltaic device characteristic parameters.

Open-circuit voltage (V_{OC}): It is the highest voltage that can be applied to a photovoltaic device. When no current is flowing through the device, this is the voltage of the cell in sunlight.

Short-circuit current (J_{SC}): It is the current that flows through an illuminated solar cell when there is no external resistance *i.e.* when the electrodes are simply connected or short-

circuited. J_{SC} is the maximum current that a photovoltaic device is able to produce. Under un external load, the current will always be less than J_{SC} . The short-circuit current depends on a number of factors, such as the area of the solar cell. To remove the dependence of the solar cell area, it is more common to list the short-circuit current density (J_{SC} in mA/cm^2), rather than the short circuit current (J_{SC} in mA).

Maximum power point (M_{pp}): It is the point (V_m , J_m) on the J-V curve at which the maximum power is produced. Power is the product of current J and voltage V. This is represented in Figure I.5 as the area of the rectangle formed between a point on the J-V curve and the axes J and V. The maximum power point is that point on the J-V curve at which the area of the resulting rectangle, JxV, is largest.

Fill Factor (FF): This is the ratio of the actual potential power output to the estimated maximum power output if current and voltage are at their maximums, J_{SC} and V_{OC}, respectively. This is a critical property for determining the efficiency of photovoltaic devices. It is an indicator of the J-V curve's 'squareness.' Fill Factor FF can be written as follows(eq. 3):

$$\boldsymbol{FF = \frac{V_m * J_m}{V_{oc} * J_{sc}}} \qquad (3)$$

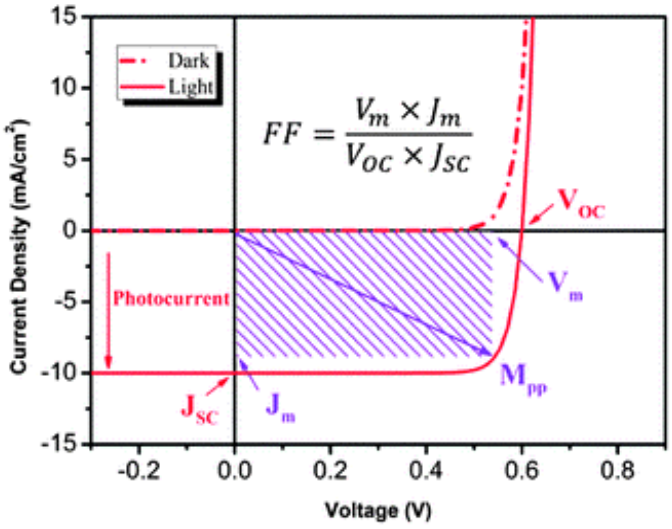

Figure I-5: Typical J-V curve for any type of solar cell in the dark and under illumination (the most important photovoltaic parameters are indicated).

Power Conversion Efficiency (PCE or η) : is defined as the ratio of power output (Pout) to the power input (Pin). PCE measures the amount of power produced by a photovoltaic device relative to the power available in the incident solar radiation. When solar simulators are used,

Pin is the number of all wavelengths and has a value of 100 mW/cm^2. This is the most general definition of a photovoltaic device's performance. PCE can be expressed as follows: (Eq. 4).

$$PCE = \frac{P_{out}}{P_{in}} * 100\% = \frac{J_m * V_m}{P_{in}} * 100\% = \frac{J_{sc} * V_{oc} * FF}{P_{in}} * 100\% \qquad (4)$$

PCE is one of the most important criteria for characterizing the efficiency of solar cells. Photovoltaic cells are all subjected to the same general test conditions in order to correlate findings from different systems, regardless of design or active content. At a temperature of 25 ºC, the cells are typically illuminated at a constant density of approximately 100 mW/cm, which is described as the normal ‘1 Light' value, with a spectrum consistent to an air-mass global value of 1.5 (AM 1.5G). The amount of atmosphere through which sunlight must travel to reach the Earth's surface is known as air mass, which defines the spectrum of radiation. This is abbreviated as AMx, where x is the reciprocal of the cosine of the sun’s zenith angle. The AM1.5G conditions mentioned above refer to the spectrum and irradiance of sunlight incident with a zenith angle of 48.2°(Figure I.6).

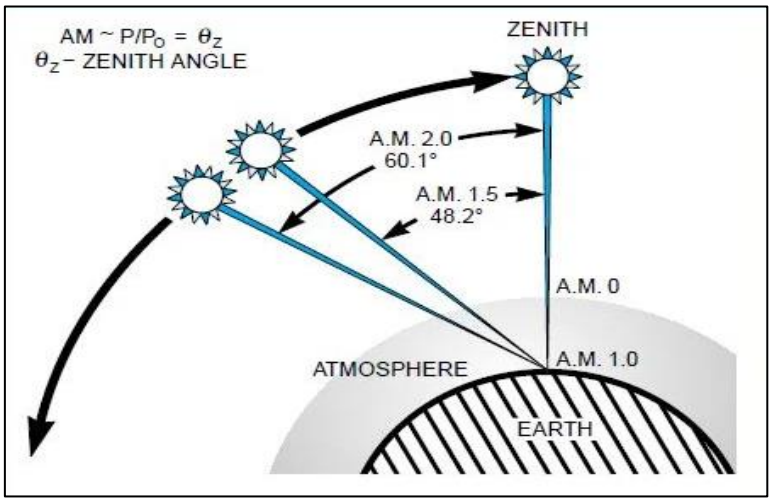

Figure I-6: The path length, in units of Air Mass, changes with the zenith angle. AM0 is the air-mass value that corresponds to insolation at sea level with the sun at its zenith. AM1.0 represents the sun at its zenith level above the Earth’s atmosphere. AM1.5 is the same, but with the sun at an oblique angle of 48.2°, which simulates a longer optical path through the Earth’s atmosphere; AM2.0 extends that oblique angle to 60.1°.

External Quantum Efficiency (EQE):

Also known as Incident Photon to Current Efficiency (IPCE), is another important parameter for solar cell characterization. It is calculated by the number of electrons extracted in an external circuit divided by the number of incident photons at a certain wavelength under short-circuit conditions. The formula for EQE is as follows (eq .5):

$$EQE = \frac{number\ of\ electrons}{number\ of\ incident\ photons} = \frac{J_{sc}(\lambda)/_{e}}{P_{in}(\lambda)/_{(hc/\lambda)}} = \frac{J_{sc}(\lambda)hc}{P_{in}(\lambda)e\lambda} \quad (5)$$

Where λ is the wavelength, e is the elementary charge, h is the Planck constant, and c is the speed of light in a vacuum.

I.5 Materials for solar cells

I.5.1 Presentation

Industrialization, a drastic rise in the population and globalization, has increased the demand for sustainable and clean energy sources manifold ever than before. Moreover, conventional energy resources are rapidly depleting and concurrently creating problems such as global warming/environmental pollution etc. In order to cope with these issues, clean and economical energy sources are in great demand as an alternative to oil and fossil fuels. Hence, researchers have shown considerable interests in exploring alternative energy resources. As a matter of fact, the sun is the source that provides an abundance of renewable solar energy and is a viable source to realize the dream of cheaper and green energy. Apparently, sunlight supplies approximately 10^4 times larger energy than our present needs. However, the biggest challenge is the conversion of solar energy into electrical energy in addressing the issue of world energy demands over a longer period of time through cheaper and environment-friendly technologies.

In resolving the issue, photovoltaic (PV) technology is the most practical and attractive approach to exploit the sustainable energy source at all levels as well as to overcome future energy crises. The demands on PV technology are rapidly increasing with time [67]. The key to exploiting PV technology is majorly relying on semiconductor materials (SMs) since solar energy is converted into electricity directly [68,69] by manipulating the potential of SM materials. Day by day, this technology is attracting more and more attention of the researchers towards exploring, tailoring and investigating the new and better SMs, which can realize the dream of green/sustainable energy. Although some SMs are already exploited in the technology, most of the modules are based on inorganic semiconductor materials (ISMs). Recently, researchers have diverted their interests to organic inorganic hybrid materials as well. It is due to the fact that the PV modules that are based on the conventional ISMs are very expensive if compared to the OSMs.

Moreover, optoelectronic device manufacturing based on organic inorganic hybrid materials are easier than the ISMs. Regardless of the advantages, the family of organic inorganic

materials-based device efficiency is rather low [70] . Hence, the study of OSMs generally seeks opportunities to dominate in PV technology with enhanced performance over the current market of conventional crystalline silicon and other ISMs.

The OSM-based device of organic photovoltaics (OPV) is thin, light and flexible. The versatility of OPV as the future energy efficient technology is paving towards replacing the utilization of conventional silicon in mass production. Some examples of OPV technology that have been introduced these days are OPV polymers, OPV DSSC (dye-sensitized solar cells) and OPV oligomers. OPV devices consist of one or several photoactive OSMs overlaid between two electrodes of cathode and anode [71]. Photoactive OSMs play a key role in the performance of optoelectronic/photovoltaic devices. Therefore, in order to determine suitable and efficient photoactive OSMs and attain their respective properties, comprehensive investigations on their electronic structure and optoelectronic properties are necessary. In this regard, the use of ab initio calculations in performing virtual experiments may lead to a cheaper experiment and a shorter developmental cycle.

Computational ab initio methodologies based on Density Functional Theory (DFT) are intensely used by theoretical researchers to solve complex problems. It was found to be more reliable and provides better results concerning the electronic structure calculations in designing and modeling new materials and tuning their properties without prior experimental knowledge. This feature of DFT has brought new insight into the investigation and education field.

I.5.2 Organic inorganic hybrid materials

According to Oxford's English Dictionary [72] a hybrid is a system that is "Derived from heterogeneous or incongruous sources; having a mixed character; composed of two diverse elements; mongrel." In practice, the term hybrid is used to denote (biological) inbreed, cars, laptops and (of course in the Netherlands) bikes [73,74]. Besides, within physics and chemistry "hybrid" is used in a variety of ways. It can refer to theoretical models [75] as well as macroscopic multilayer devices [76] and composites. In this thesis we use the term "organic-inorganic hybrid" for crystalline materials that incorporate inorganic and organic components to produce multifunctional materials. Organic materials largely consist of carbon and hydrogen atoms, with the option of added nitrogen, oxygen and sulfur. The components are denoted in the black circle in Figure I.7. They are the core ingredients in living organisms, from cellulose to hormones and fats! Organic products also have a number of commercial uses, such as plastics and dyes.

The raw organic materials that are used for these applications are (indirectly) derived from natural organic sources such as petroleum. Organic materials are often used in applications that require fast processing, low cost and reliability. These three special criteria have inspired research efforts to produce organic materials that are ideal for electronics. In recent years, the first organic electronic applications have been marketed in (flexible) displays and organic light emitting diodes (OLED) [77,78].

Inorganic simply means not-organic. Inorganic elements cover much of the periodic tables, see Figure I.**7**. Inorganic materials also require high-tech and high-power equipment to be processed. However, their durable and high-performance magnetic and electric properties are unequalled and thus inorganic materials are widely used in conventional electronic applications.

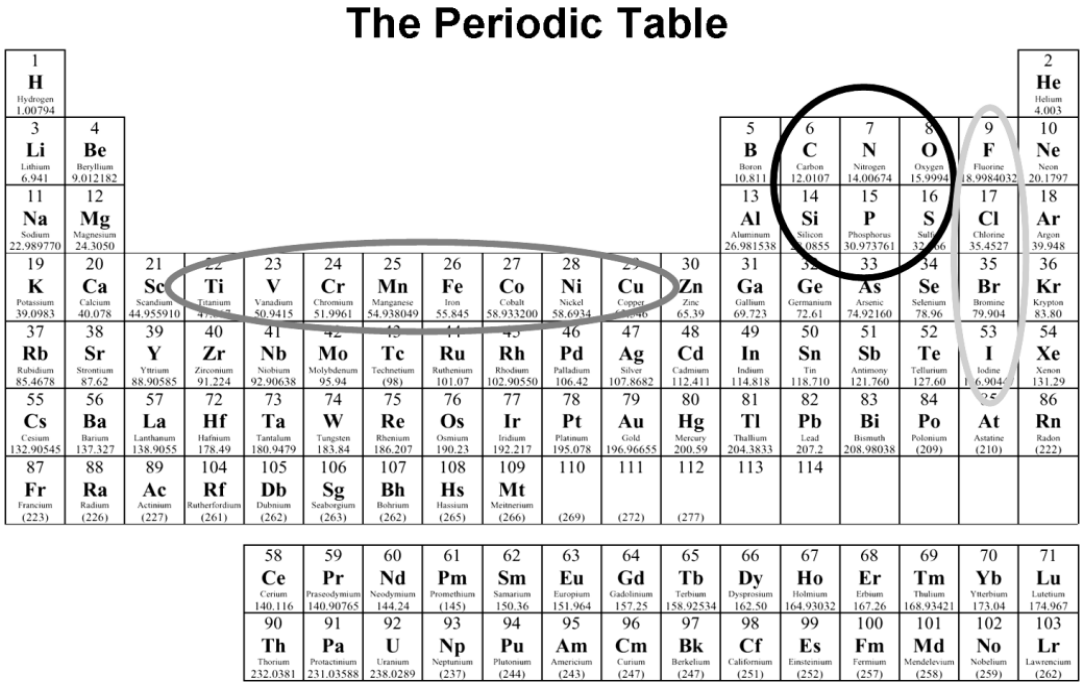

Figure I-7: The periodic table of elements. The elements in the black circle are the basis of most organic materials. In general, the other components are referred to as inorganic. The dark gray oval denotes the most important magnetic ions and the light gray oval denotes the halogen atoms used in the hybrids.

In this thesis, we present the ab initio of organic-inorganic hybrids, in which it is tried to well-understand different properties of the organic materials. We explore the possibilities of organic-inorganic hybrids for divers application such as photovoltaics and optoelectronic devices. Those materials could be of interest for applications in cheap and printable single-use

electronics that require both data storage and data processing. Moreover, this combination of unique parameters is rarely observed in conventional materials and is therefore, also from a fundamental point of view, an interesting place to start the exploration of the field of organic-inorganic hybrids.

I.5.3 Perovskite materials

Presentation

Perovskite is considered one of the most promising materials of the twenty-first century. In the past few decades, perovskite has attracted broad attention and made great progress in energy storage, pollutant degradation as well as optoelectronic devices due to its superior photoelectric and catalytic properties. The discovery of calcium titanate (CaTiO3) in 1839 by a German scientist, Gustav Rose, during a trip to Russia, in the Ural Mountains, which was named "perovskite," in honor of the Russian mineralogist Lev von Perovski, was considered to be the origin of perovskite, and materials with the same type of crystal structure as that of CaTiO3 were known as the perovskite materials [79]. approximately half a century later, H.L. Wells et al. at Sheffield Scientific School, a pre-World War I unit of Yale University, prepared the first synthetic halide perovskite based on cesium and lead, although its perovskite structure was determined only during the 1950s by C.K. Møller at the Royal Veterinary and Agricultural College in Copenhagen, Denmark. Møller also observed photoconductivity in this material. The general chemical formula for perovskite compounds is ABX_3, where 'A' and 'B' are two cations, often of very different sizes, and X is an anion (frequently oxide) that bonds to both cations.

The 'A' atoms are generally larger than the 'B' atoms (Figure I.8). The unique physical properties of perovskite materials such as high-absorption coefficient, long-range ambipolar charge transport, low exciton-binding energy, high dielectric constant, ferroelectric properties, etc. have gained a huge interest in these materials for optoelectronic and photovoltaic applications. Meanwhile, researchers at Philips (Eindhoven, the Netherlands) and Western Electric (New York, N.Y.) introduced oxide perovskites for use in condensers and electromechanical transducers. Starting in the 1950s, research and development related to oxide perovskites flourished, leading to the introduction of these materials in the fabrication of various products, such as fuel cells, glass-ceramic articles, catalysts, gas sensors, heating elements, lasers and superconducting devices [80,81]. Perovskite's notable crystal structure was first described by Victor Goldschmidt in 1926 in his work on tolerance factor [82]. The crystal structure was later published in 1945 from X-ray diffraction data on barium titanate by Helen Dick Megaw [83].

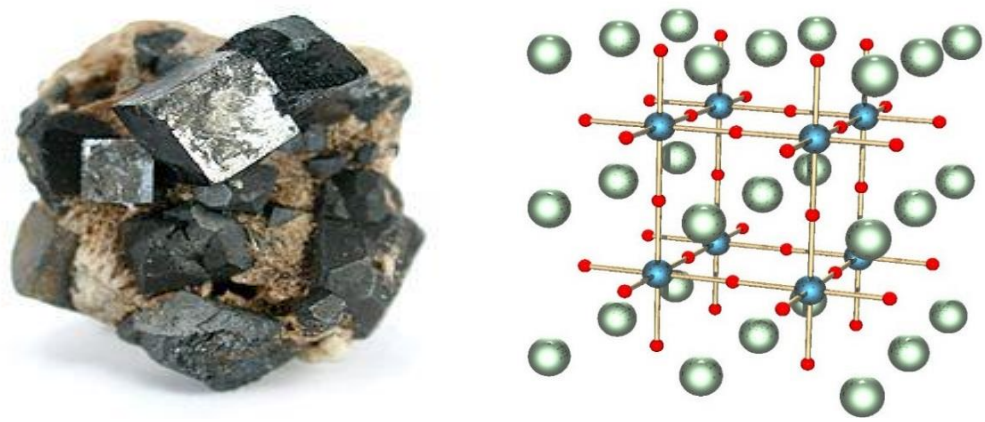

Figure I-8: (a) Crystals of perovskite on matrix, (b) Structure of perovskite with general chemical formula ABX_3.The red spheres are X atoms (usually oxygens), the blue spheres are B atoms (a smaller metal cation, such as Ti^{4+}), and the green spheres are the A atoms (a larger metal cation, such as Ca^{2+}).

Structure :

Perovskite structures are adopted by many oxides that have the chemical formula ABO_3. The idealized form is a cubic structure (space group Pm3m, no. 221) which is rarely encountered, the B cation in 6-fold coordination, surrounded by an octahedron of anions, and the A cation in 12-fold cuboctahedral coordination. The orthorhombic (e.g. space group Pnma, no. 62, or Amm2, no. 68) and tetragonal (e.g. space group I4/mcm, no. 140, or P4mm, no. 99) phases are the most common non-cubic variants. Although the perovskite structure is named after $CaTiO_3$, these mineral forms a non-idealized form. $SrTiO_3$ and $CaRbF_3$ are examples of cubic perovskites. Barium titanate is an example of a perovskite which can take on the rhombohedral (space group R3m, no. 160), orthorhombic, tetragonal and cubic forms depending on temperature [84].

Properties

Perovskite materials exhibit many interesting and intriguing properties from both the theoretical and the application point of view. Ferroelectricity, superconductivity, charge ordering, spin dependent transport, high thermopower and the interplay of structural, magnetic and transport properties are commonly observed features in this family. These compounds are used as sensors and catalyst electrodes in certain types of fuel cells [85,86] and are candidates for memory devices and spintronic applications [87], they are also some interests for solar cell application [88, 89].

Applications

Photovoltaics

Perovskite solar cells (PSCs) are the most emerging area of research among different new generation photovoltaic technologies due to their super power conversion efficiency (PCE). In 2009, Kojima et al. first prepared perovskite solar cells [90], which is an important step for the development of solar cells. Later, Burschka et al. fabricated the solar cells by a two-step continuous deposition method, and the photovoltaic conversion efficiency was increased to 15% [91]. And then, the performance was improved by changing device structure and optimizing the carrier transport layer, So far, the efficiency of perovskite solar cells has exceeded 22% [92]. The huge development of perovskite solar cells will provide the possibility for its commercialization.

Synthetic perovskites have been identified as possible inexpensive base materials for high-efficiency commercial photovoltaics [93], they showed a conversion efficiency of up to 25.5% reported in 2020 by NREL [94-96] and can be manufactured using the same thin-film manufacturing techniques as that used for thin film silicon solar cells [96]. In July 2016, a team of researchers led by Dr. Alexander Weber-Bargioni demonstrated that perovskite PV cells could reach a theoretical peak efficiency of 31 %[96]. Among the methylammonium halides studied so far the most common is the methylammonium lead triiodide ($CH_3NH_3PbI_3$). It has a high charge carrier mobility and charge carriers lifetime that allows light-generated electrons and holes to move far enough to be extracted as current, instead of losing their energy as heat within the cell. In fact, Methylammonium halides are deposited by low-temperature solution methods (typically spin-coating). Other low-temperature (below 100°C) solution-processed films tend to have considerably smaller diffusion lengths. Stranks et al. described nanostructured cells using a mixed methylammonium lead halide ($CH_3NH_3PbI_3{-}xCl_x$) and demonstrated one amorphous thin-film solar cell with an 11.4% conversion efficiency, and another that reached 15.4% using vacuum evaporation. The film thickness of about 500 to 600 nm implies that the electron and hole diffusion lengths were at least of this order. They measured values of the diffusion length exceeding 1 μm for the mixed perovskite, an order of magnitude greater than the 100 nm for the pure iodide. They also showed that carrier lifetimes in the mixed perovskite are longer than in the pure iodide."

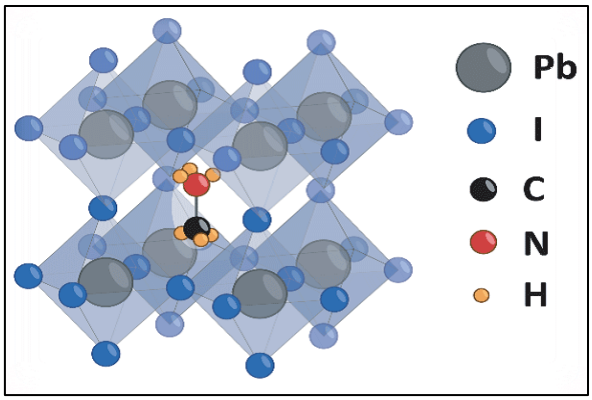

Figure I-9: Crystal structure of $CH_3NH_3PbX_3$ perovskites (X=I, Br and/or Cl). The methylammonium cation ($CH_3NH_3^+$) is surrounded by PbX_6 octahedra [97].

Figure I.10 shows some major milestones in the progress of PSCs, including the device evolution from dye-sensitized to planar structure and the advancements in solvent and compositional engineering techniques. This successful progress also stimulated great interest in this emerging PV technology, as the annual number of articles published with the topic of PSCs has increased from a single digit number in 2012 to ~2300 in 2016. this remarkable evolution mainly from the perspectives of device architecture and material deposition method by focusing on the early developments of the materials, notable devices with excellent performance, technical advances in preparation methods, and the future directions of the field.

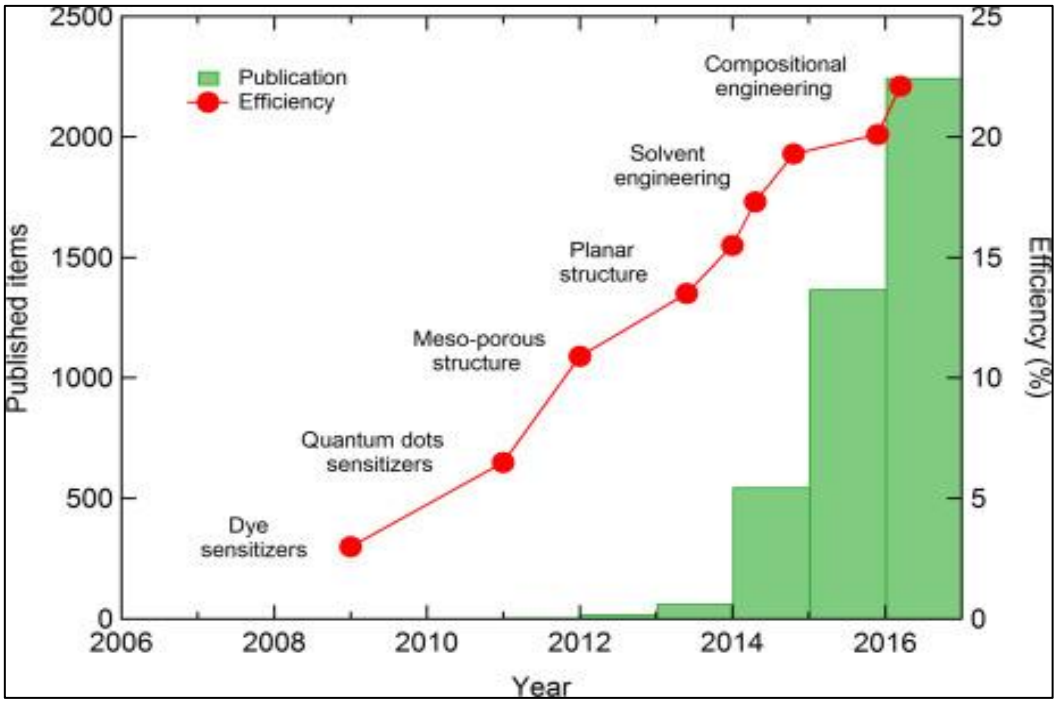

Figure I-10: Record efficiency and numbers of publications with the topic on perovskite solar cells (PSCs) from 2009 to 2016. The publication data is adapted from ISI web of science.

Perovskite solar cells stem from dye-sensitized solar cells (DSSCs), based on a semiconductor formed between a photo-sensitized anode and an electrolyte, a photoelectrochemical system. present a low-cost solar cell belonging to the group of thin film solar cells, have a promising solid-state structure as well as rapid efficiency leaps (Figure I.11), which have now reached 22.7% [95].

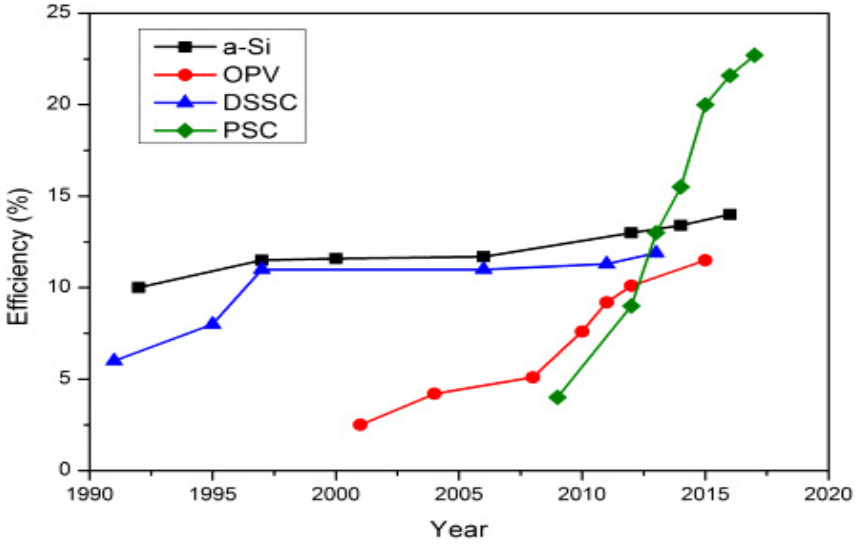

Figure I-11: Comparing the rate of increase in perovskite solar cell efficiencies with the other thin-film PV technologies.

Photo electrolysis

In September 2014, researchers at EPFL in Lausanne, Switzerland, reported achieving water electrolysis at 12.3% efficiency in a highly efficient and low-cost water-splitting cell using perovskite photovoltaics [98, 99].

Lasers

In 2008, researchers demonstrated that perovskite can generate laser light. $LaAlO_3$ doped with neodymium gave laser emission at 1080 nm [100]. In 2014 it was shown that mixed methylammonium lead halide ($CH_3NH_3PbI_3{-}xCl_x$) cells fashioned into optically pumped vertical-cavity surface-emitting lasers (VCSELs) convert visible pump light to near-IR laser light with a 70% efficiency [101].

Memory devices

Resistive memory (RRAM) is a non-volatile memory based on reversible conversion between high- and low-resistive states under the action of the applied electric field. Zhang et

al. were the first to demonstrate a 64-bit RRAM array utilizing perovskite oxide $Pr_{0.7}Ca_{0.3}MnO_3$ materials by a 500 nm CMOS process [102]. This RRAM array has a high/low resistance ratio larger than 1000. After that, multilayer-graphene transparent conductive electrodes were employed for flexible perovskite RRAMs [103].

I.5.4 Transition metal oxides Materials.

Transition metal oxides are attractive for many electronic applications because of their special ability to form different phases and properties by varying the metal to oxygen ratio. Stoichiometric TMOs such as MoO_3, WO_3, V_2O_5, CrO_3, and NiO are normally insulators. However, experimentally synthesized TMOs tend to have oxygen vacancies or metal vacancies, and slightly non-stoichiometric TMOs are semiconductors. Therefore, in most publications, they are referred to as MoO_x, WO_x, V_2O_x, CrO_x and NiO_x. Further reduction of the metal oxidation states could even lead to metallic properties. For example, MoO_2 is a metallic oxide and has a symmetrical monoclinic crystal structure [104,105]. MoO_3, WO_3, V_2O_5, CrO_3 and NiO are d^0 TMOs which share the property that the metal's d band is empty because the transition metal cation is fully oxidized. For MoO_x, WO_x, V_2O_x and CrO_x, the conduction band minima are primarily composed of the d-states of metal and the valence band maxima is dominated by O 2p states. The oxygen vacancies tend to fill the d-band of the metal cation, which forms occupied gap states. These states push the Fermi level close to the conduction band. Thus these sub-stoichiometric d^0 TMOs are found to be n-type semiconductors. Besides, these TMOs have a very high work function of $\geq$6 eV. Studies have shown that the increase of oxygen defects can cause a work function drop because: i) the oxygen defect states within the bandgap which serve as donor levels can cause the Fermi level shift or ii) the TMOs' electron chemical potential is altered by the lower electronegativity of the reduced metal oxidation states [105]. Different from MoO_x, WO_x, V_2O_x and CrO_x, NiO_x is intrinsically p-type because Ni vacancies move the Fermi level closer to the valence band, and the work function of NiOx is smaller. Either being n-type or p-type, these above mentioned TMOs manage to work as effective hole-selective contacts for silicon solar cells which is explained by Figure I.12.

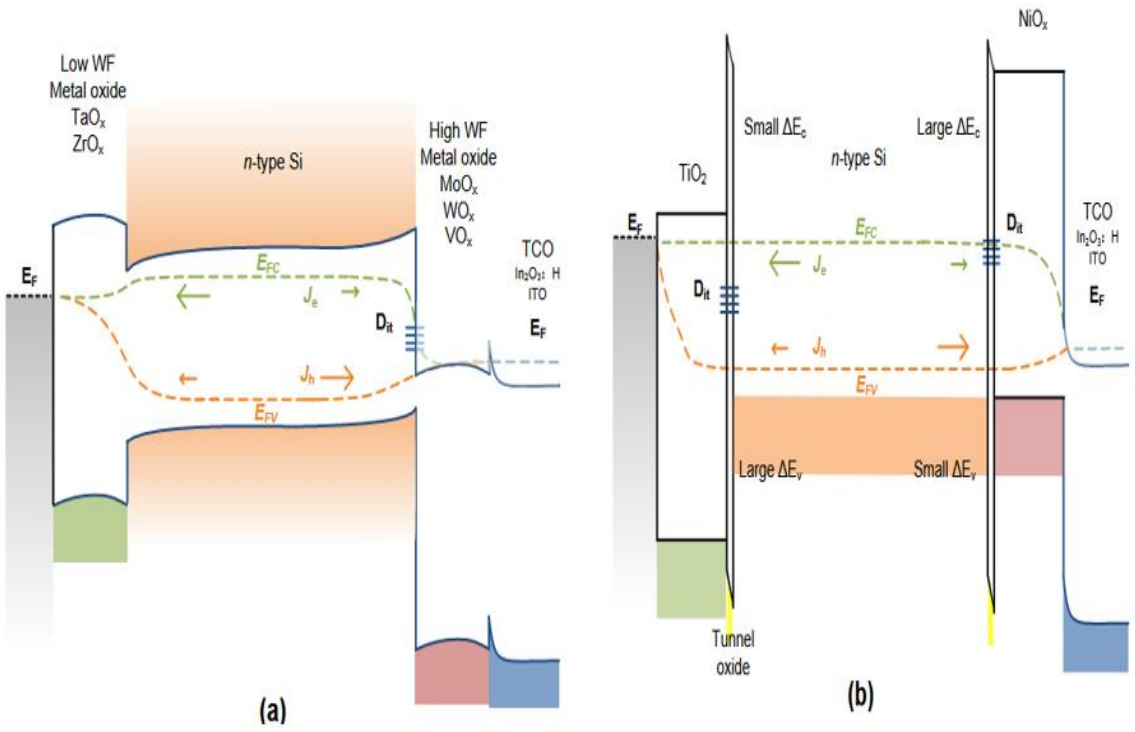

Figure I-12: Band diagram of a TMO-based carrier selective contact using (a) extreme work function TMOs to induce band-bending and (b) low valence band offset material TMOs for band alignment with c-Si. The graphs were adapted from Macco et al. [106].

On the other hand, TiO_x, Ta_2O_x and ZrO_x which have either a very low work function or a low conduction band offset with Si, are electron selective materials for silicon solar cells as is also shown in Figure I.12**.** [107].

Another outstanding merit of these TMOs is their high optical transparency. The optical bandgap for these materials is typically ≥3 eV [106,107]. This merit makes them perfect candidates to replace doped a-Si:H and work on the sunny side of a solar cell for high photocurrent. However, the optical absorption of these TMOs can increase by the introduction of defects [104]. Figure I.13. shows the band alignment schematic of these TMOs with Si.

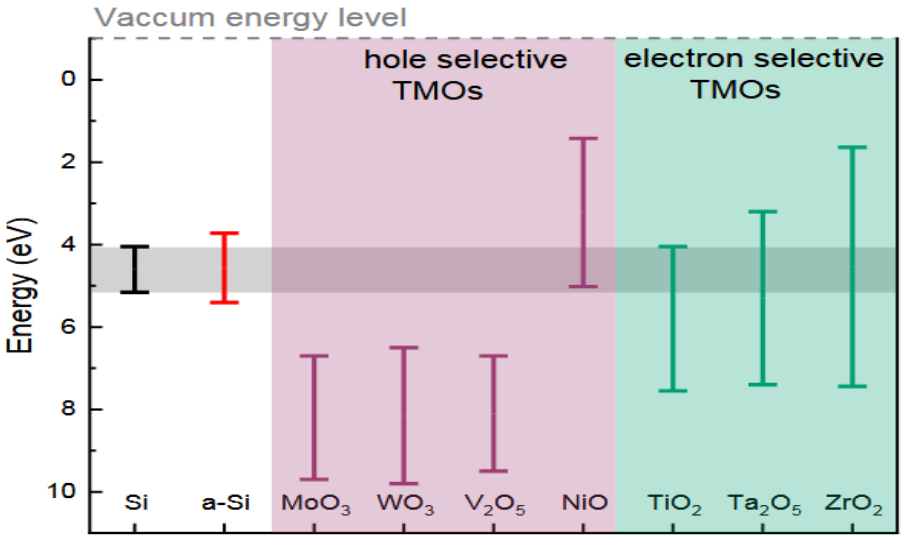

Figure I-13: Bandgap and band offset of several representative carrier selective TMOs with Si. A-Si is shown as comparison [104, 108-110].

The transition metal oxides materials present admirable physical, chemical, electronic, magnetic and thermoelectrical properties. These properties are making them a promising candidate for many applications, such as energy storage in Li-ion batteries, catalysis..., then the use of TMOs materials for photovoltaic application still limited, for that reason, we dedicated a study on the electronic, optical, magnetic and thermoelectric properties of the compound $NaMnAsO_4$ as one of the TMO materials, to show that this class of materials can be used as an active absorber in photovoltaic cells.

I.6 Conclusion

The organic-inorganic hybrid perovskites are new materials whose use is interesting for fundamental research and applied devices, due to their unique organic-inorganic combined attributes and the enhanced quantum confinement. On the other hand, transition metal oxide materials show great properties because of their special structure. Till now, there has been a lot of applications fabricated with organic-inorganic hybrid and transition metal oxide materials. The results are quite encouraging.

Chapter II:
Theoretical methods

II.1 Introduction

In this chapter, we introduce the theoretical approach used in this thesis to describe the structural, electronic, optical, magnetic, and thermoelectrical properties of molecular combinations. The main focus of this chapter is on the Density Functional Theory (DFT) whose main goal is to solve the well-known Schrödinger equation. This chapter presents the basic theories underlying DFT methods.

Ab initio calculations are used to predict the properties of materials by solving the equations of quantum mechanics without using any adjustable variables. Most prominently among the available ab initio methods, the ground state density functional theory (DFT), based on the Hohenberg-Kohn theorem [111], has simplified the electronic structure calculations by focusing on the density of the electronic system instead its wave function.

The most popular approach to DFT is the Kohn-Sham (KS) auxiliary system, which introduces non interacting electrons having the same density as the interacting system. In practice, DFT calculations are relatively light and provide an access to a large system. DFT gives new tools to study and understand the results of the calculations. This is why DFT is today the most used approach to the theoretical prediction of physical and chemical properties.

II.2 Schrödinger Equation

In 1926, Schrödinger [112] developed a time-independent equation that determines precisely the electronic structures of matter. For a system consisting of M nuclei and N electrons, this equation is described by the following equation [113,114]:

$$\hat{H}\,\Psi(r) = E\Psi(r) \qquad \textbf{(1)}$$

Where $\hat{H}$ is an operator that represents the total Hamiltonian, Ψ is the total wave function, and E is the total energy of the molecular system. The Hamiltonian includes the kinetic and potential energies of the many electron system as follows:

$$\hat{\mathrm{H}} = -\frac{\hbar}{2m_e}\sum_i^N \nabla_i^2 - \frac{\hbar}{2}\sum_A^M \frac{1}{M_A}\nabla_A^2 - \frac{e^2}{4\pi\varepsilon_0}\sum_i^N\sum_A^M \frac{Z_A}{r_{iA}} + \frac{e^2}{4\pi\varepsilon_0}\sum_i^N\sum_j^N \frac{1}{r_{ij}} + \frac{e^2}{4\pi\varepsilon_0}\sum_A^M\sum_B^M \frac{Z_A Z_B}{R_{AB}} \qquad \textbf{(2)}$$

Where m_e is the mass of the electron, M_A is the mass of the nucleus, ∇_i^2 is the Laplacian, Z_A is the nuclear charge of the atom A, r_{iA} is the distance between nucleus A and electron i, r_{ij} is the distance between electrons i and j, R_{AB} is the distance between nuclei A and B, ε_0 is

the permittivity of free space, and $\hbar$ is the Plank constant divided by 2π. Equation (2) can be rewritten as:

$$\hat{H} = \hat{T}_e + \hat{T}_n + \hat{V}_{n-e} + \hat{V}_{e-e} + \hat{V}_{n-n} \qquad \textbf{(3)}$$

Where $\hat{T}_e$ and $\hat{T}_n$ represent the electronic and nuclear kinetic energies respectively, $\hat{V}_{n-e}$ represents the attractive potential energy of nucleus-electron, $\hat{V}_{e-e}$ and $\hat{V}_{n-n}$ represent the repulsive potential energies of electron-electron and nucleus-nucleus respectively.

II.2.1 Born – Oppenheimer

In order to solve the Schrödinger equation that involves a problem with (3N + 3M) degrees of freedom, approximations are required. The most popular approximation that took advantage of the fact that nuclei move much more slowly than do electrons is known as Born-Oppenheimer (B.O) approximation. With the assumption that the nuclei are stationary relative to the electrons, the second and last terms of equation (3) are zero and constant respectively, resulting into the following electronic Schrödinger equation [115]:

$$\hat{H}^{elec}\Psi^{elec} = E^{elec}\Psi^{elec} \qquad \textbf{(4)}$$

Where, $\hat{H} = -\frac{\hbar}{2m_e}\sum_i^N \nabla_i^2 - \frac{e^2}{4\pi\varepsilon_0}\sum_i^N \sum_A^M \frac{Z_A}{r_{iA}} + \frac{e^2}{4\pi\varepsilon_0}\sum_i^N \sum_j^M \frac{1}{r_{ij}}$ **(5)**

Although the approximation made by B.O was successful in reducing the complexity of solving the many-body Schrödinger equation, equation (4) is still insolvable for the many-electron systems and further approximations are needed.

II.2.2 Hartree-Fock Method

Hartree-Fock (HF) method is the second approximation that is made to solve the Schrödinger equation by assuming that electrons move independently of each other and can only interact with the average field of other electrons [116,117]. This assumption requires that the individual electrons are described by functions called spin orbitals ψi. For fermions, the total (multiple-electron) wave function must be anti-symmetric upon interchange of electron coordinates to satisfy Pauli-Exclusion principle. In the HF approximation, the total wave function is often written in the form of a single determinant called the Slater determinant:

$$\Psi = \frac{1}{\sqrt{n!}} \begin{vmatrix} \Psi_1(1) & \Psi_2(1) & \dots & \Psi_n(1) \\ \Psi_1(2) & \Psi_2(2) & \dots & \Psi_n(2) \\ \dots & \dots & \dots & \dots \\ \Psi_1(n) & \Psi_2(n) & \dots & \Psi_n(n) \end{vmatrix} \quad \textbf{(6)}$$

Where $\frac{1}{\sqrt{n!}}$ is the normalization factor for an n-electron determinant. To describe the motional states that electrons have in molecules, linear combination of atomic orbitals (LCAO) approximation was introduced to HF method. Based on the LCAO approximation [118] molecular orbitals (ψi) are represented in terms of the atomic orbitals (ϕ):

$$\psi_i = \sum_{\mu} C_{\mu i} \phi_\mu \quad \textbf{(7)}$$

Where $C_{\mu i}$ are the molecular orbital coefficients. Applying both HF and LCAO approximations to the electronic Schrödinger equation lead to the HF operator equation:

$$\hat{f}\psi_i = \epsilon_i \psi_i \quad \textbf{(8)}$$

Where ϵi are the orbital energies and $f\wedge$ is the HF operator given by the following equation:

$$\hat{f} = \hat{h} + \sum_j^N (2\hat{J}_j - \hat{K}_j) \quad \textbf{(9)}$$

Where $\hat{h}$ represents the energy of a single electron including the kinetic and nucleus-electron potential energies, $\sum_j^N (2\hat{J}_j - \hat{K}_j)$ represents the electron-electron repulsion energy of a single electron with all other electrons, $\hat{J}_j$ and $\hat{K}_j$ are called the Coulomb and exchange operators, respectively. The HF equation (8) can be solved iteratively using the self-consistent field (SCF) method [119].

The main problem of HF method is that it is inadequate for calculating many observables due to an exclusion of the electron correlation in the HF approximation. The difference between the exact and HF energies is defined as electron correlation energy ($E_{corr}=E_{exact}- E_{HF}$). This correlation energy is due to the fact that the interaction of electrons with different spins is not included in the HF approximation. The major approaches (so called post HF methods) that include correlation energy are the configuration interactions (CI), Moller-Plesset perturbation theory (MP), and the coupled cluster theory (CC) [120].

However, these methods are extremely computationally intensive for large molecular systems. Hence, there is a great need for an efficient and less computationally intensive method that can describe their intermolecular properties accurately.

II.4 Density-Functional Theory

Density functional theory (DFT) is amongst the most widely used and computationally accessible post HF method that includes electron correlations. DFT employs the electron density, $\rho(x, y, z)$, instead of the many-electron wavefunction as the main variable. Using the B.O approximation, the DFT electronic energy is written as:

$$E_{elec}\left[\rho(r)\right] = T_e\left[\rho(r)\right] + V_{n-e}\left[\rho(r)\right] + V_{e-e}\left[\rho(r)\right] + Q_{e-e}\left[\rho(r)\right] \quad \textbf{(10)}$$

Where the terms represent the kinetic energy of the electrons, the nuclear-electron attractive energy, the electron repulsive energy, and the non-classical electron-electron repulsive energy respectively. The latter term is a correction to the self-repulsion included in the classical $V_{e-e}\left[\rho(r)\right]$. The middle terms in equation (10) are known and given as the following equations:

$$V_{n-e}\left[\rho(r)\right] = \sum_A \int \frac{Z_A}{|r - r_A|}\rho(r)\,dr \quad \textbf{(11)}$$

$$V_{e-e}\left[\rho(r)\right] = \frac{1}{2}\iint \frac{\rho(r_1)\rho(r_2)}{r_{12}} dr_1 dr_2 \quad \textbf{(12)}$$

Exact mathematical expressions for $T_e\left[\rho(r)\right]$ and $Q_{e-e}\left[\rho(r)\right]$ are not known and approximations must be used for them. Circa 1930, Thomas and Fermi developed a simple approximation to $T_e\left[\rho(r)\right]$ which is exact for uniform electron gas [121,122]. However, Thomas-Fermi method failed in many ways (e.g. it could not reproduce chemical bonds), and therefore, this method had been abandoned until the middle of 1960. The concept of Thomas-Fermi method was revived to motivate the DFT formalism [123,124].

II.4.1 Hohenberg-Kohn Theorems

In 1964, Hohenberg and Kohn formulated two fundamental theorems of DFT [111]. The first theorem (after called the existence theorem) states that all the ground state electron properties of a system are determined uniquely by the ground state electron density function $\rho_0(x, y, z)$ as obtained in the presence of an external potential v, and the ground state energy of a molecule is a functional of the $\rho_0(x, y, z)$:

$$E_0 = E_0\left[\rho_0\right] \quad \textbf{(13)}$$

The exact ground state energy functional is not known. The second theorem uses the energy variational principle that states that any trial electron density function ρ_t will give energy higher than or equal to true ground state energy calculated with ρ_0:

$$E_v[\rho_t] \geq E_0[\rho_0] \quad \textbf{(14)}$$

Where Ev is the electronic energy of the system.

II.4.2 Kohn-Sham Formalism

In 1965, Kohn and Sham proposed a practical approach that employed Hohenberg and Kohn theorems to obtain the electronic properties of molecular systems [125]. They solved the hindrance of not having accurate kinetic energy functionals by assuming that the kinetic energy describes a fictitious system of non-interacting electrons that has the same density as the original set of interacting electrons. The kinetic energy of the non-interacting electrons can be approximated by a single Slater determinant of Kohn-Sham orbitals (ψ_i^{ks}), and it is given by:

$$T_s\left[\{\psi_i^{KS}\}\right] = -\frac{1}{2}\sum_i \int \psi_i^{KS}(r)\nabla^2\psi_i^{KS}(r)dr \quad \textbf{(15)}$$

The Kohn-Sham orbitals give the electron density as follows:

$$\rho(r_i) = \sum_i^N \left|\psi_i^{KS}(r_1)\right|^2 \quad \textbf{(16)}$$

To obtain the Kohn-Sham orbitals, the variational principle, that requires the energy to be minimum with respect to ψ_i^{ks}, was used to obtain Kohn-Sham equations:

$$\hat{h}^{KS}\psi_i^{KS} = \epsilon_i\psi_i^{KS} \quad \textbf{(17)}$$

Where $\hat{h}^{KS}$ is the Kohn-Sham operator and it is represented as:

$$\hat{h}^{KS} = \hat{h} + \sum_j^N 2\hat{J}_j + v_{xc} \quad \textbf{(18)}$$

Where $\hat{h}$ is the energy of a single electron including the kinetic and nucleus-electron potential energies, $\hat{J}_j$ is the Coulomb operator, and v_{xc} is the exchange-correlation potential functional. The difference between Kohn-Sham operator in equation (18) and HF operator in equation (8) is v_{xc} which replaces the HF exchange operator. The exchange-correlation potential functional is given as the functional derivative of the exchange-correlation energy functional with respect to the electron density:

$$v_{xc} = \frac{\delta E_{xc}}{\delta\rho} \quad \textbf{(19)}$$

Where $E_{xc}[\rho]$ is the exchange-correlation energy functional (see below). Similar to HF equations, Kohn-Sham equations are solved iteratively using the SCF method.

Since the kinetic energy of the non-interacting system in equation (15) is not equal to $T_e[\rho(r)]$, the difference between both terms is added to the non-classical electronic repulsive energy $Q_{e\text{-}e}[\rho(r)]$ to define the exchange-correlation functional ($E_{XC}[\rho]$):

$$E_{xc} \equiv T_e[\rho(r)] - T_s[\{\psi_i^{KS}\}] + Q_e[\rho(r)] \qquad \textbf{(20)}$$

Therefore, based on Kohn-Sham DFT approach, equation (2.10) for the electronic energy of an N-electron system can be expressed as:

$$E_{elec} = -\frac{1}{2}\sum_i \int \psi_i^{KS}(r)\nabla^2 \psi_i^{KS}(r)dr + \sum_A \int \frac{Z_A}{|r-r_A|} + \frac{1}{2}\iint \frac{\rho(r_1)\rho(r_2)}{r_{12}} dr_1 dr_1 + E_{xc}[\rho] \quad \textbf{(21)}$$

The only unknown term in equation (21) is the exchange-correlation functional, hence, approximations are required. In the past 30 years, many accurate approximations to $E_{XC}[\rho]$ have been proposed, leading to a great accumulation of knowledge of electronic and structural properties in several areas in molecular and solid-state physics.

II.5 Exchange-correlation approximation

LDA Functionals

The local density approximation (LDA) forms the foundation for most of the other (more advanced) exchange-correlation functionals. The original LDA uses only the local density of a uniform electron gas in E_{XC}. In this model, the local exchange-correlation energy functional is often expressed as:

$$E_{xc}[\rho(r)] = \int \rho(r)\, \varepsilon_{xc}[\rho(r)]dr \qquad \textbf{(22)}$$

Where $\varepsilon_{xc}[\rho(r)]$is the energy density of a uniform electron gas and it is often represented as a sum exchange and correlation energies:

$$\varepsilon_{xc} = \varepsilon_x + \varepsilon_c \qquad \textbf{(23)}$$

The exact form of LDA exchange functional part for this model is given by:

$$E_{xc}^{LDA}[\rho(r)] = -\frac{3}{4}\left(\frac{3}{\pi}\right)^{\frac{1}{3}} \int [\rho(r)]^{3/4} dr \qquad \textbf{(24)}$$

The LDA correlation functional part has been approximated by Vosko, Wilk and Nusair "VWN" (it has a very complicated function many parameters functional form) [126]. For open shell systems, the electronic density is replaced by the spin electronic densities (ρ_α and ρ_β), and the method is often referred to as the local spin density approximation (LSDA). However, because most real systems have inhomogeneous density distributions, these functionals lead to inaccurate molecular properties [127].

Many different DFT approximations of the exchange-correlation functionals treat the individual exchange and correlation contributions separately. The various exchange-correlation functionals are classified based on their formulations.

GGA Functionals

The best-known approximation after LDA is the generalized gradient approximation (GGA). It uses both the local electron density (ρ) and the gradient of the electron density (∇_ρ) which accounts for the inhomogeneities in the density. Thus:

$$E_{xc}^{GGA}[\rho(r)] = \int \rho(r)\, \varepsilon_{xc}[\rho(r), \nabla\rho(r)]dr \qquad \textbf{(25)}$$

The general form of most GGA functionals, which includes the LDA functional, is given by :

$$\varepsilon_{xc}^{GGA}[\rho(r)] = \varepsilon_{xc}^{LDA}[\rho(r)] + \Delta\varepsilon_{xc}\left[\frac{\nabla\rho(r)}{\rho^{\frac{4}{3}}(r)}\right] \qquad \textbf{(26)}$$

Some of the most common GGA exchange functionals are PBE [128], B [129], and PW91 [130], while some of the most popular GGA correlation functionals are LYP [131], PBE [132], and PW91 [132]. These functionals can be combined to obtain GGA exchange-correlation functionals. Although GGA functionals include more information than LDA functionals, they are not always accurate, hence additional factors need to be considered for the exchange-correlation functional in order to improve the accuracy of DFT.

The introduction of these GGA-type functionalities led to the widespread use of DFT within the chemical community in the 1990s. The use of GGA-type functionals significantly increases the accuracy of the calculations compared to the description provided by the LDA, particularly, for the binding energy of the molecules. GGA-type functionals also provide a better description of the equilibrium volumes, moduli of elasticity and magnetic properties of the compounds compared to the LDA.

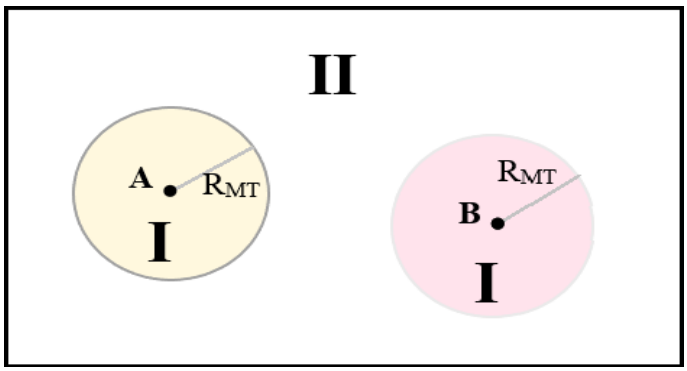

Figure II-1: Schematic illustration of two atomic spheres A and B with radius RMT (region I) and the interstitial region between the spheres (region II).

II.5.1 Solving Kohn-Sham equations

Various methods can be used to solve the Kohn-Sham equations. In this section, we will discuss the most popular methods to solve the Kohn-Sham equations, which are The Full-Potential Linearized Augmented Plane Wave (FP-LAPW) and the Pseudopotential methods.

Full-Potential Linearized Augmented Plane Wave (FP-LAPW)

The Full-Potential Linearized Augmented Plane Wave (FP-LAPW) method developed by Andersen is an improvement of the Augmented Plane Wave (APW) method developed by Slater [133, 134]. This method is based on the self-coherent solution of the Kohn-Sham equations in two arbitrarily defined regions of the elementary mesh (see Figure II.1).

- Region I: Corresponds to non-overlapping atomic spheres (A and B) of radius R_{MT} (MT=Muffin Tin), where a series of linear combinations of radial and angular functions are used.

- Region II: The interstitial region between the spheres, which can be described by plane wave expansions.

The convergence of this base is controlled by cut-off parameter "RMT*K_{max}", which is the product of the radius of the smallest Muffin-Tin sphere and the cut-off energy of the wave plane base.

This method allows the consideration of a realistic potential (FP ≡ Full-Potential), which is not restricted to the spherical component. In contrast to methods using pseudopotentials, the core electrons are included in the calculations. This gives a correct description of the wave functions near the nucleus. This is the most precise method, but it is heavy in computing time.

All works presented in this thesis was done using WIEN2K package developed by Blaha and Schwarz in 1990 and based on the Full-Potential Linearized Augmented Plane Wave method [135].

pseudo-potentials (Plane Wave) method

A plane wave base requires a very large number of waves to describe the system. One way to reduce the base is to remove the waves whose kinetic energy is greater in absolute value than a certain energy, which is called "$E_{cut-off}$". This base, although reduced, is however not well adapted because a very large number of plane waves are still needed to correctly describe the strongly bound orbitals of the core electrons.

Elements with few electrons with require few plane waves, while heavy elements or transition metals will require extremely powerful computing resources. However, in most cases,

valence electrons are the only one involved in chemical bonds. Core electrons therefore be grouped with nuclei: this approximation is called frozen core approximation; a pseudopotential is then introduced [136].

Phillips and Kleiman set up the first pseudopotentials in 1958. The pseudopotentials currently used are determined from “all electron” calculations, which make the method more accurate [137,138]. The pseudopotentials associated with high cut-off energies are called “Hard” compared to those called “Soft”. Vanderbilt has developed a smaller waveform base than these traditional pseudopotentials, with even lower cut-off energies, called “ultra-soft”. This has made it possible to consider systems that are more complex [139].

II.6 Calculation code

II.6.1 Wien2K code

The WIEN2k code based on FP-(L) APW method is used to solve the Kohn-Sham equations for present work. Its first public version was released by P. Blaha and K. Schwarz in 1990. It is in progress till now. There are two main parts of the WIEN2k code to perform calculations on the particular crystalline solid as shown in the figure below. These are the Initialization and the self-consistent field cycle (SCF). Each of these portions has numerous independent programs linked via shell scripts. There are several other analytical tools to determine a large number of physical properties e.g. charge density, band structure, and elastic properties et cetera. First section initializes the calculation by generating structure file and computing nearest neighbor distances. Also, it checks whether muffin tin spheres are overlapping. Afterwards a new structure file is generated supporting given space group. Next the symmetry operations are performed and the k-mesh is obtained in full brillouin zone. Finally, it estimates the input trial density for iterations. Second SCF cycle construct potential from input trial density for the Kohn-Sham equations. It gives eigenvectors and eigenvalues after one complete cycle. Latter valence and core charge densities are computed by integration over all valence and core states respectively. Then they are summed up to new electron charge density. It is then compared with the previous old charge density. If both are same then SCF cycle converges successfully. Otherwise same cycle is repeated with new electron density as input parameter until SCF cycle is converged. After the convergence of SCF cycle one can calculate the desired physical properties.

Results obtained with WIEN2k are considered to be most accurate, though they are most expensive in terms of computation. For bulk systems it behaves quiet well. However, for

supercell, constructed for magnetic configuration, it becomes quiet time consuming. Therefore, for such problem's parallelization become important. In this method parallelization is done over k points and every k point is calculated on single CPU.

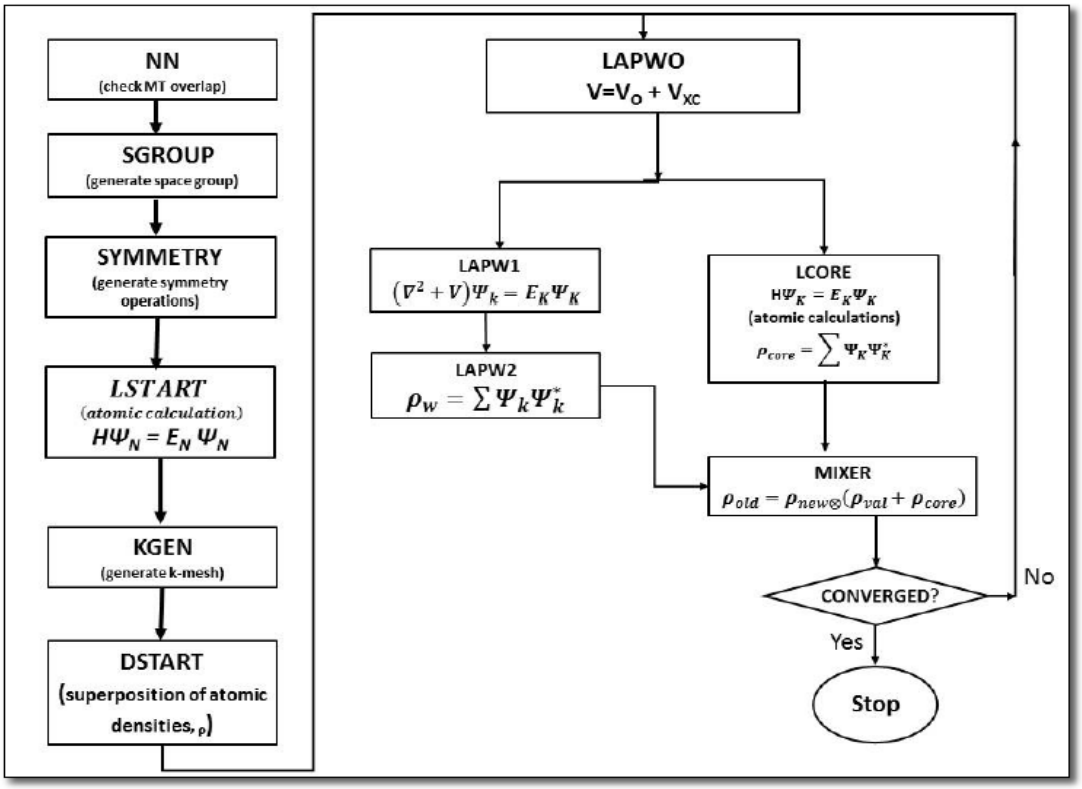

Figure II-2: Schematic flow chart for the WIEN2k code**.**

II.6.2 Boltzmann transport theory

The Boltzmann equation describes the statistical behavior of a fluid of electron which is not in thermodynamic equilibrium. Considering the relaxation time approximation, it is possible to derive analytical expressions for transport properties of interest: the electronic conductivity, the thermal conductivity and the Seebeck coefficient. The following explanations are directly inspired from References [140-142].

II.6.2.1 Boltzmann equation

Firstly, it is important to remember that the distribution function of an electron gas at equilibrium, i.e. the average occupation number by electrons of the state k with energy ε_k, is given by the following Fermi-Dirac distribution function:

$$f_{\mathbf{k}}^{0} = \frac{1}{e^{(\varepsilon_{\mathbf{k}}-\mu)/k_B T} + 1} \qquad (1)$$

Where k_B is the Boltzmann constant and $\boldsymbol{\mu}$ is the chemical potential.

In a more general way, the distribution function $f(\mathbf{r}, \mathbf{k}, t)$ of electrons with a wave vector **k** at the position **r**, at time t can vary due to three processes : the diffusion of electrons by temperature or concentration gradients, their acceleration by an external field and finally their scattering by phonons, lattice defects or impurities. The variation in time of the total distribution can be expressed as the sum of these three contributions:

$$\left(\frac{\partial f}{\partial t}\right) = \left(\frac{\partial f}{\partial t}\right)_{\mathbf{diffusion}} + \left(\frac{\partial f}{\partial t}\right)_{\mathbf{field}} + \left(\frac{\partial f}{\partial t}\right)_{\mathbf{scattering}} \qquad \mathbf{(2)}$$

First of all, one can consider an electron is not subject to scattering but experiences an external field **F**. It induces a variation of its wave vector k since the external field is expressed as:

$$\boldsymbol{F} = \hbar \frac{d\mathbf{k}}{dt} \qquad \mathbf{(3)}$$

During a time interval dt, the electron will move from one state (r- $\dot{r}$dt, k- $\dot{k}$dt, t-dt) to another (**r,k,t**). Since the scattering is left aside, the change rate of the distribution function represents the continuous flow of a particle taking into account the diffusion and the acceleration of the electrons. It is then called the drift term and can be expressed by:

$$\left(\frac{df}{dt}\right)_{\mathbf{drift}} = \frac{f(r-\dot{r}dr, k-\dot{k}dk, t-tdt) - f(r,k,t)}{dt} \qquad \mathbf{(4)}$$

The Taylor expansion of the first term allows one to express it as:

$$f(r - \dot{r}dr, k - \dot{k}dk, t - tdt) = f(r, k, t) - \left[\dot{k}.\frac{\partial \mathbf{f}}{\partial \mathbf{k}} + \dot{r}.\frac{\partial \mathbf{f}}{\partial \mathbf{r}} + \frac{\partial \mathbf{f}}{\partial \mathbf{t}}\right] dt + \cdots \qquad \mathbf{(5)}$$

Considering this Taylor expansion, the change of the wave vector under a force (3) and the velocity of the electron $\mathbf{v} = \dot{\boldsymbol{r}}$ the drift term can then be rewritten as:

$$\left(\frac{\mathbf{df}}{\mathbf{dt}}\right)_{\mathbf{drift}} = \left[\frac{\mathbf{1}}{\hbar}(\boldsymbol{F} * \boldsymbol{\nabla}_{\mathbf{k}} \boldsymbol{f} + \mathbf{v}.\boldsymbol{\nabla}_{\mathbf{r}} \boldsymbol{f} + \frac{\partial f}{\partial t}\right] \qquad \mathbf{(6)}$$

Even if left aside at first, one has to remember that the electron scattering also plays an important part in their distribution. To be correct, the distribution function has to satisfy the equilibrium condition which means that the sum of the contributions (2.3) has to be null at the steady state.

Since the drift term takes diffusion and acceleration into account, this steady state condition leads to

$$\left(\frac{df}{dt}\right)_{\mathbf{drift}} = \left(\frac{df}{dt}\right)_{\mathbf{scattering}} \qquad \mathbf{(7)}$$

This condition of balance results in the Boltzmann transport equation:

$$\frac{\partial f}{\partial t} = -\mathbf{v}.\nabla_{\mathbf{r}} f - \frac{1}{\hbar}(F.\nabla_k f) + \left(\frac{df}{dt}\right)_{\mathbf{scattering}} \qquad \mathbf{(8)}$$

The three main contributions to the rate of the transport distribution function change with time are correctly found in this equation. In the right part of the equation, the first term on the left is related to the electron diffusion moving in and out a specific volume with a velocity **v**. If the distribution function is spatially homogeneous this term becomes zero. On the contrary, when this function varies in space, the electron ratio flowing in and out the volume is not zero anymore and this diffusion becomes a contribution to the change of the distribution function. Now if the distribution function varies with the momentum state **k**, the number of particles accelerated by an external force **F** into a specific region of momentum will differ from the particles that are leaving this same region. The second term is related to this effect. The last term is related to the probability of electron scattering and brings up the difficulty to solve the Boltzmann transport equation. Nevertheless, no physical solution can be found without it. It is then necessary to simplify the collision term through the relaxation time approximation to express the related variation of the distribution function.

II.6.2.2 Relaxation time approximation

In order to solve the Boltzmann transport equation, one has to give an analytical expression to the scattering term. This can be done considering the transitions leading to a change of k-state.

The distribution function can be seen as independent of the position r in this case. If a transition occurs from the state k to another state k′, f(k) will decrease and conversely. The scattering term can then be expressed by:

$$\left(\frac{df}{dt}\right)_{\mathbf{scat.}} = \sum_{k'}(W(\mathbf{k}',\mathbf{k}).f(\mathbf{k}')[1-f(\mathbf{k})] - W(\mathbf{k},\mathbf{k}').f(\mathbf{k})[1-f(\mathbf{k}')]) \qquad \mathbf{(9)}$$

Where $W(\mathbf{k}',\mathbf{k})$ is the transition rate from a state $\mathbf{k}'$ to a state **k**, $f(\mathbf{k}')$ is the probability of electron occupation in the initial state $\mathbf{k}'$ and $(1-f(\mathbf{k}))$ is the probability of the presence of

a vacancy in the state **k**. The usual case where the Fermi level lies below the bottom of the conduction band **($f(\mathbf{k})$ and $f(\mathbf{k}')$ << 1)** is studied. Considering the equilibrium state (1), one can express the following equation:

$$W(\mathbf{k}',\mathbf{k}).f_0(\mathbf{k}') = W(\mathbf{k},\mathbf{k}').f_0(\mathbf{k}) \qquad \textbf{(10)}$$

One can observe here the logical impact of this equality on the transition probabilities. When $\varepsilon_{\mathbf{k}} < \varepsilon_{\mathbf{k}'}$, W(k,k′) < W(k′,k). In other words, the probability for an electron to be scattered from a low energy state to a higher one is smaller than the inverse probability. The scattering can be rewritten as:

$$\left(\frac{df}{dt}\right)_{\mathbf{scat.}} = -\sum_{\mathrm{k}'} W(\mathbf{k}',\mathbf{k})\left[f(\mathbf{k}) - f(\mathbf{k}')\frac{f_0(\mathbf{k})}{f_0(\mathbf{k}')}\right] \qquad \textbf{(11)}$$

In almost every real case, the deviation from the equilibrium is small, i.e. the scattering results from an elastic collision. The initial energy state ε_k is then close from the energy of the final state $\varepsilon_{k'}$. This can be stated as:

$$f(\mathbf{k}) = f_0(\mathbf{k}) + f_1(\mathbf{k}), \text{ with } f_1(\mathbf{k}) \ll f_0(\mathbf{k}) \qquad \textbf{(12)}$$

It results in the approximation $f_0(\mathbf{k}) \approx f_0(\mathbf{k}')$ and allows one to rewrite the scattering term as:

$$\left(\frac{df}{dt}\right)_{scat.} = -f_1(\mathbf{k})\sum_{k'} W(\mathbf{k}',\mathbf{k})\left[1 - \frac{f_1(\mathbf{k})}{f_1(\mathbf{k}')}\right] \qquad \textbf{(13)}$$

Those assumptions constitute the relaxation time approximation, only valid for homogeneous scattering. The relaxation time **τ(k)** is defined as the time between two collisions leading to scattering and allows one to rewrite the scattering term as:

$$\left(\frac{df}{dt}\right)_{\mathbf{scat.}} = -\frac{f_1(\mathbf{k})}{\tau(\mathbf{k})} = \frac{f(\mathbf{k}) - f_0(\mathbf{k})}{\tau(\mathbf{k})} \qquad \textbf{(14)}$$

Where

$$\frac{1}{\tau(\mathbf{k})} = \sum_{\mathbf{k}'} W(\mathbf{k}',\mathbf{k})\left[1 - \frac{f_1(\mathbf{k})}{f_1(\mathbf{k}')}\right] \qquad \textbf{(15)}$$

In this relaxation time approximation, the Boltzmann transport equation is reformulated as;

$$\frac{\partial f}{\partial t} + \frac{1}{\hbar}(\mathbf{F}.\nabla_{\mathbf{k}} f) + \mathbf{v}.\nabla_{\mathbf{k}} f = \frac{f(\mathbf{k}) - f_0(\mathbf{k})}{\tau(\mathbf{k})} \qquad \textbf{(16)}$$

This relaxation time characterizes the speed of recovery of the equilibrium state: for a short relaxation time, many collisions help the system to return to its initial state and conversely for a long relaxation time. Indeed a system recovering from a steady but non equilibrium state (t = 0) to its equilibrium without any external force will satisfy the following equation:

$$\frac{\partial f}{\partial t} = -\frac{f(\mathbf{k}) - f_0(\mathbf{k})}{\tau(\mathbf{k})} \qquad \textbf{(17)}$$

The non-equilibrium system then decays exponentially with the relaxation time to its equilibrium:

$$f - f_0 = (f - f_0)_0 e^{-t/\tau} \qquad \textbf{(18)}$$

In this thesis, the relaxation time is approximated by a constant value, which is implemented in the BoltzTraP code. But in fact, the transition probabilities will differ depending on the type of scattering mechanisms electrons are facing and this relaxation time will take different temperature and energy dependent expressions.

II.6.2.3 Transport coefficients derivation

It is crucial, in order to study thermoelectricity, to be able to calculate the transport properties of a system. At the macroscopic level, the relations between the electrical or the heat current **J** and $\mathbf{J_Q}$**,** the electric field **E** and a temperature gradient $\Delta\mathbf{T}$ in an isotropic solid are:

$$\mathbf{J} = \boldsymbol{\sigma}.\boldsymbol{E} + \boldsymbol{S\sigma}.\Delta\mathbf{T} \qquad \textbf{(19)}$$

$$\mathbf{J_Q} = \boldsymbol{S_\sigma}.\mathbf{T}.\mathbf{E} + \boldsymbol{\kappa}.\Delta\mathbf{T} \qquad \textbf{(20)}$$

Where σ is the electrical conductivity, S the Seebeck coefficient and κ the thermal conductivity.

At the microscopic level of the transport, the electrical current of carriers is defined by:

$$\mathbf{J} = e\sum_{\mathbf{k}} f(\mathbf{k})\mathbf{v}(\mathbf{k}) \qquad \textbf{(21)}$$

$$\mathbf{v}(\mathbf{k}) = \frac{1}{\hbar}\frac{\partial \varepsilon_{\mathbf{k}}}{\partial \mathbf{k}} \qquad \textbf{(22)}$$

There is here a need for an analytical expression of the distribution function, the one which is expressed by the Boltzmann transport theory. In the absence of magnetic field and temperature gradients, the population on the state k – i.e. the distribution function *f*(k) – is given by the linearized Boltzmann transport equation (16). This expression can be rewritten in a

convenient way when considering an electric field **E (F = eE)** and a stationary state ($\partial f/\partial t = 0$) as:

$$\boldsymbol{f}(\mathbf{k}) = \boldsymbol{f_0}(\boldsymbol{\varepsilon_k}) + \boldsymbol{e}\left(-\frac{\partial f_0}{\partial \varepsilon}\right)\boldsymbol{\tau}(\mathbf{k})\mathbf{v}(\mathbf{k}).\mathbf{E} \qquad \textbf{(23)}$$

The electrical current can then be reformulated as:

$$\mathbf{J} = \mathbf{e}\boldsymbol{f_0}(\boldsymbol{\varepsilon_k})\sum_{\mathbf{k}}\mathbf{v}(\mathbf{k}) + \boldsymbol{e^2}\sum_{\mathbf{k}}\left(-\frac{\partial f_0}{\partial \varepsilon}\right)\boldsymbol{\tau}(\mathbf{k})\mathbf{v}(\mathbf{k})\mathbf{v}(\mathbf{k}).\boldsymbol{E} \qquad \textbf{(24)}$$

When there is no gradient of temperature, the macroscopic expression of the electrical current (21) is reduced to its electric field contribution. The electrical conductivity can then be expressed as:

$$\boldsymbol{\sigma}(\mathbf{k}) = \boldsymbol{e^2}\sum_{\mathbf{k}}\left(-\frac{\partial f_0}{\partial \varepsilon}\right)\boldsymbol{\tau}(\mathbf{k})\mathbf{v}(\mathbf{k})\mathbf{v}(\mathbf{k}).\boldsymbol{E} \qquad \textbf{(25)}$$

$$\boldsymbol{\sigma}(\mathbf{k}) = \sum_{\mathbf{k}}\left(-\frac{\partial f_0}{\partial \varepsilon}\right)\boldsymbol{\sigma}(\mathbf{k}) \qquad \textbf{(26)}$$

The transport properties are expressed as tensors since they can be anisotropic. As for the density of states, the tensor of conductivity shows a distribution in energy. It represents the contribution to the conduction of electrons having an specific energy ε:

$$\boldsymbol{\Xi} = \sum_{\mathbf{k}}\boldsymbol{\sigma}(\mathbf{k})\frac{\boldsymbol{\delta}(\epsilon-\epsilon_{\mathbf{k}})}{\boldsymbol{d}\epsilon} \qquad \textbf{(27)}$$

The transport coefficients in a unit cell crystal of volume Ω can then be calculated for a specific chemical potential μ and temperature by integrating this conductivity distribution:

$$\boldsymbol{\sigma}(\boldsymbol{T},\boldsymbol{\mu}) = \frac{\mathbf{1}}{\Omega}\int \boldsymbol{\Xi}(\epsilon)\left[-\frac{\boldsymbol{\partial f_0}(\boldsymbol{T},\epsilon)}{\boldsymbol{\partial}\epsilon}\right]\boldsymbol{d}\epsilon \qquad \textbf{(28)}$$

$$\boldsymbol{S}(\boldsymbol{T},\boldsymbol{\mu}) = \frac{\mathbf{1}}{\Omega\mathbf{e}\mathbf{T}\boldsymbol{\sigma}(\boldsymbol{T},\boldsymbol{\mu})}\int \boldsymbol{\Xi}(\epsilon)(\epsilon-\boldsymbol{\mu})\left[-\frac{\boldsymbol{\partial f_\mu}(\boldsymbol{T},\epsilon)}{\boldsymbol{\partial}\epsilon}\right]\boldsymbol{d}\epsilon \qquad \textbf{(29)}$$

$$\boldsymbol{\kappa}(\mathbf{T},\boldsymbol{\mu}) = \frac{\mathbf{1}}{\Omega\mathbf{T}}\int \boldsymbol{\Xi}(\epsilon)(\epsilon-\boldsymbol{\mu})\left[-\frac{\boldsymbol{\partial f_\mu}(\boldsymbol{T},\epsilon)}{\boldsymbol{\partial}\epsilon}\right]\boldsymbol{d}\epsilon \qquad \textbf{(30)}$$

II.6.2.4 BoltzTraP code

The BoltzTrap code [143] allows one to compute these transport coefficients with little computational effort. This code uses Fourier expansions to solve Boltzmann equation in the relaxation time approximation. The interpolated band structure is used to calculate the required

derivatives to evaluate transport properties, e.g. the group velocities. It is therefore essential that the band energies are correctly computed through Wien2k package before using BoltzTraP.

In this code, the rigid band approximation is made. It means that the bands are independent in doping, the chemical potential is simply shifted. To facilitate the computation of the transport coefficients, the relaxation time can be considered as constant in BoltzTraP, i.e. temperature and energy independent. However, it is also possible to implement energy and temperature dependent relaxation times corresponding to specific electron scattering processes and then to compute their relative transport properties.

In this thesis WIEN2k code is used to explore different functional magnetic materials. Different xc functionals are used to compare structural, electronic, magnetic and optical properties of studied materials. WIEN2k has been used most successfully to obtain accurate results. Besides, the Boltztrap code was performed to well-understand the thermoelectrical properties for the studied materials.

Chapter III:
Study of optical, electrical, and photovoltaic properties of $CH_3NH_3PbI_3$ perovskite

III.1 Introduction

Photovoltaic solar cells have been considered as an appealing renewable energy source and an interesting future substitute for fossil-fuel used in electricity generation systems [144]. The photovoltaic panels based on silicon thin films are already used in the industry for different devices [145]. As a promising candidate for photovoltaic application because of their low manufacturing cost with great properties such as long carrier lifetime, direct bandgap, high absorption coefficient and high efficiency that already exceeded 22% in the past five years [146-148].

Hybrid halide perovskite is a class of perovskite materials having the general chemical formula ABX_3, where A, B and X refer to methyl ammonium, lead and halide, respectively [144-146]. Number of researchers report that substituting different element in A, B and X sites, leads to produce a new material with a tunable band gap, and interesting properties [149-151]. $CH_3NH_3PbI_3$ compound crystalizes in three different crystalline structures, i.e., cubic (Pm3-m), tetragonal (I4/mcm) and orthorhombic (*Pnma*) structure. At 161 K, a structural transition from the orthorhombic to tetragonal structure is observed and remains stable until 330 K, at which, second transition to the cubic structure takes place [152,153]. More discussions are needed to improve their efficiency. Etgar et al, and Kojima report that $CH_3NH_3PbI_3$ films are characterized by a large absorption coefficient, a direct bandgap, and a very high diffusion length relatively large for both electrons and holes. These advantages render $CH_3NH_3PbI_3$ as a great absorber of light [154,155].

The objective of this work, is to study the correlation between the electronic structure of $CH_3NH_3PbI_3$ material and its efficiency in a photovoltaic device, by calculating the open-circuit voltage V_{oc} and the short-circuit current J_{sc} using density functional theory. The theoretical approach used in this work opens the possibility to rapidly estimate the efficiency of a given hybrid halide perovskite such as $CH_3NH_3PbI_3$ without the necessity to realize a photovoltaic device as well as optimize the size of an already existed photovoltaic device.

III.2 Computational details

The calculations were performed using Density Functional Theory (DFT) within the Full-Potential Linearized Augmented Plane Wave (FP-LAPW) as implemented in the WIEN2K package [156]. The Generalized Gradient Approximation proposed by Perdew, Burke, and Ernzerhof (GGA-PBE) is used to describe the exchange-correlation energy [157]. Basis functions, charge density, and potential were expanded inside the muffin-tin spheres in

combination with spherical harmonic functions with a cut-off $l_{max} = 2$, and in Fourier series in the interstitial region. We have used a parameter $R_{MT}xK_{max} = 7$, where K_{max} is the plane wave cut-off and R_{MT} is the smallest of all atomic sphere radii. The self-consistency is obtained by 800 K-points in the irreducible symmetry wedge of the first Brillouin zone. The iteration process is repeated until the calculated total energy of the crystal converges to less than 10^{-5} Ry.

III.3 Results and discussion

III.3.1 Structural properties

As well known, $CH_3NH_3PbI_3$ compound exists in three different structures presented in table III.1. Before studying the electronic and optical properties of this material, the structural stability has been studied by calculating the total energy of the three structures of $CH_3NH_3PbI_3$ compound (Orthorhombic, tetragonal and cubic).

Table III-III-1: Structural properties of $CH_3NH_3PbI_3$ material in its different crystalline structure

Crystalline structure	***Orthorhombic***	***Tetragonal***	***Cubic***
Space group	*Pnma (N° 62)*	*I_4/mcm (N° 140)*	*Pm-3m (N° 221)*
Lattice parameters	a = 8.37526 Å b = 12.58934 Å c = 8.37526 Å α = β = γ = 90°	a = b = 9.13663 Å c = 13.00602 Å α = β = γ = 90°	a =b = c = 5.79973 Å α = β = γ = 90°

As shown in Figure III.1, the most stable structure of $CH_3NH_3PbI_3$ is the tetragonal crystalline structure with a total energy of about -339055.7971 Ry compared to the orthorhombic (E_{Total} = -339048.0747 Ry) and the cubic structure (E_{Total} = -84762.7178 Ry). For the rest of this work, we will focus on the tetragonal structure to calculate the electronic and optical properties of the $CH_3NH_3PbI_3$ material. We used cell parameters and atomic coordinates reported in references [158,159].

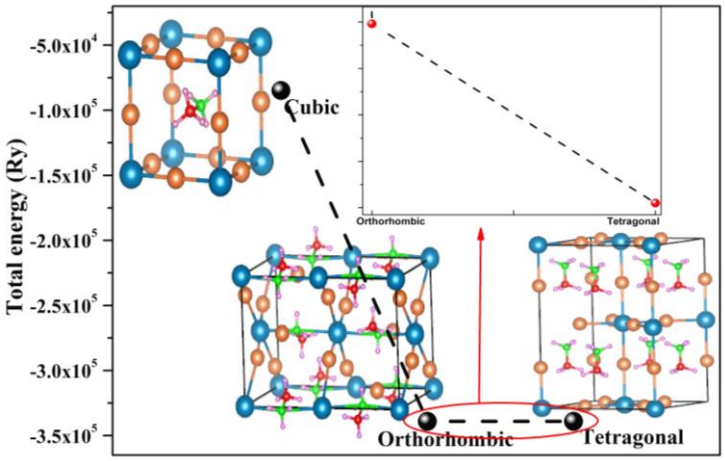

Figure III-1: Calculated total energy of $CH_3NH_3PbI_3$ compound for different crystalline structures.

III.3.2 Electronic structure of $CH_3NH_3PbI_3$

The electronic properties have been investigated for the tetragonal geometry of $CH_3NH_3PbI_3$, using GGA-PBE approximation. The total density of states DOS is presented in Figure. III.2. The vertical line presents the Fermi level, taken as energy reference. It takes place close to the top of valence band for intrinsic $CH_3NH_3PbI_3$, which confirms the p-type of this semiconductor.

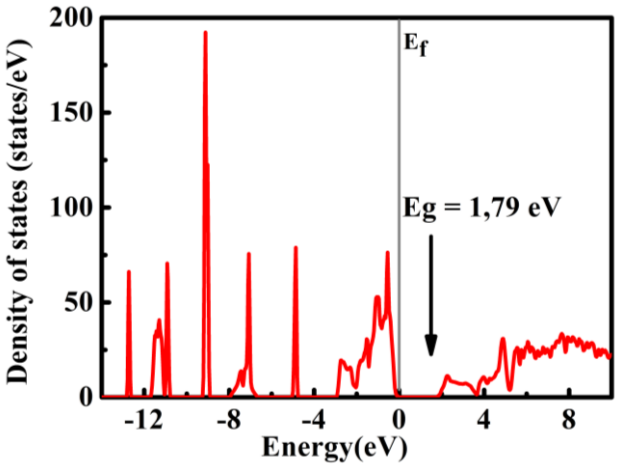

Figure III-2: Total density of states of tetragonal $CH_3NH_3PbI_3$ from FLAPW calculations.

The gap energy is found equal to 1.79 eV, which is reasonably in accordance with the experimental band gap varying from 1.51 eV [160] to 1.63 eV [161]. Other previously published calculations using different methods report a band gap value ranging from 0.57 eV to 2.87 eV for tetragonal $CH_3NH_3PbI_3$. Experimental and theoretical band gap values are gathered in Table III.2.

Table III.2: Theoretical calculations and experimental band gaps of tetragonal $CH_3NH_3PbI_3$ with different approximations		
Theoretical results		***Experimental results***
Band gap (eV)	***Calculation methods***	***Band gap (eV)***
1.43[160]	*DFT*	*1.51*[160]
1.68[174]	*DFT*	*1.55*[174]
0.60[174]	*SOC-DFT*	*1.52*[175]
2.87[174]	*GW*	*1.63*[161]
1.67[174]	*SOC-GW*	*1.61*[176]
1.56 – 1.66[177] *0.57*[177] *1.67*[176,177] *1.57*[178]	*DFT* *SOC-DFT* *SOC-GW* *SOC-GW*	

The DOS calculations allow to understand photovoltaic phenomena taking place in this compound and to determine the atoms and electronic bands contributing to such phenomena. For this aim, the *l*-decomposed DOS of *s* and *p* like-states are computed for organic group CH_3NH_3, I, and Pb atoms, and displayed in Figure. III.3. As well known, the photovoltaic or optical phenomena originates from electronic transitions between bands allowed by the known rule conditions $\Delta l = \pm 1$ where l = 0, 1, 2, 3 is the orbital quantum number.

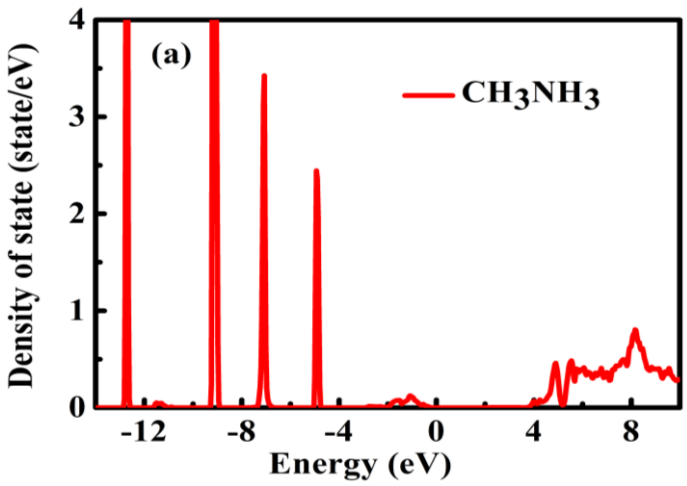

Figure III-3: The density of states of CH_3NH_3 from FLAPW calculations.

In Figure III.3. no transitions can be observed for organic CH_3NH_3 group since the DOS is practically absent near Fermi level E_f. For I atom (Figure III.4), only the s band contribute to

the valence band at negative energies. Then, non-band conduction at positive energies is observed. As seen in Figure. III.5, FLAPW calculations give for Pb atom s and p bands at valence band and at conduction band, respectively, pointing out to the possible contribution to photovoltaic phenomena induced by electronic transitions between both bands.

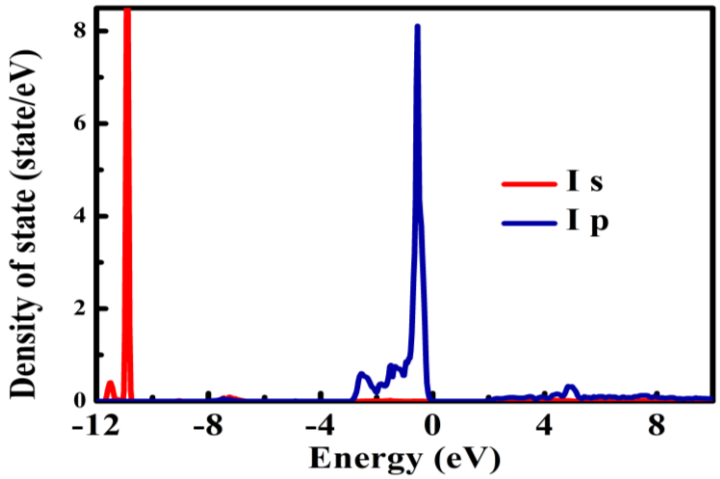

Figure III-4: The density of states of I atoms from FLAPW calculations.

Moreover, non-contribution to the photovoltaic phenomena can originate from electronic transitions between bands of I and Pb atoms since the Δl=0. This condition cancels electronic transitions between s(I) band in the valence band and s(Pb) in the conduction band as shown in Fig. 3c. As conclusion, only Pb atom in this compound is involved in the observed photovoltaic behavior. It is worth noting that our results are in accordance with those obtained from the calculations on $CH_3NH_3PbI_3$ using the same GGA-PBE implanted in Wien2k [162].

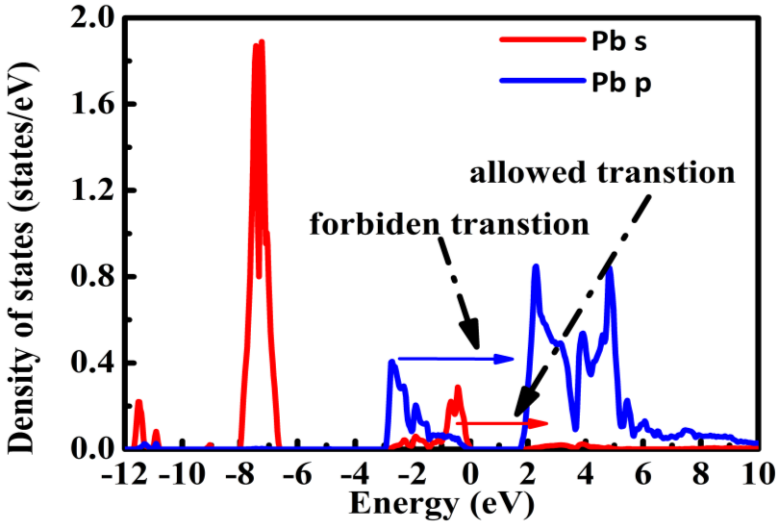

Figure III-5: The density of states of Pb atom from FLAPW calculations.

In this paper, we redid the calculations and found the same results. Then, we use these results as input to compute crucial parameters requested by the industrial applications such as the Short Circuit Current Jsc, the Open Circuit Voltage Voc, the Quantum Efficiency QE, and electrical power of $CH_3NH_3PbI_3$. The estimate of such parameters is based on the dielectric constant calculations.

III.3.3 Optical properties

As well known, the dielectric constant is an important physical quantity, which allows analyzing the optical properties of materials. It permits to better understand their nature, as well as to provide a clear reason for using them in photovoltaic or optoelectronic devices. The imaginary part of optical dielectric constant ε_i (E) and the absorption coefficient $\alpha(E)$ are calculated versus energy E using GGA-PBE approximation for $CH_3NH_3PbI_3$. Computed $\alpha(E)$, ε_i(E) and available experimental data are reported in Figure. III.6.

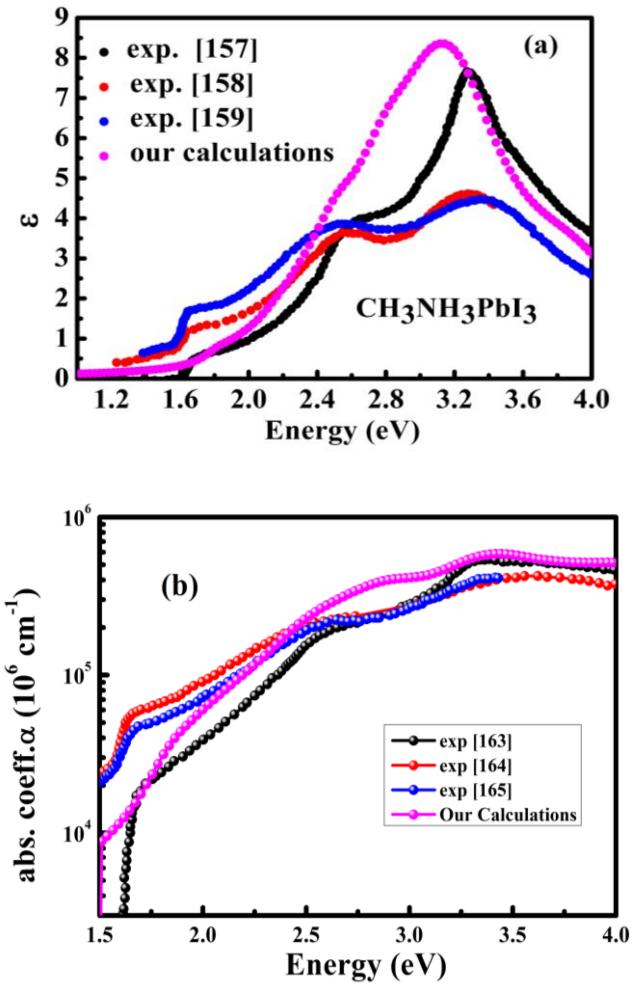

Figure III-6: Calculated Imaginary part of optical dielectric constant (a) and Coefficient of absorption (b). Both physical quantities compared to experimental data.

Firstly, some differences in the experimental curve shapes are observed [163–165]. Considering these differences, we can reasonably conclude that our calculations agree with experimental data even our calculated curves do not fit perfectly. The shape curve dependence on sample is probably justified by the degradation of the surface after the elaboration of the tetragonal $CH_3NH_3PbI_3$.

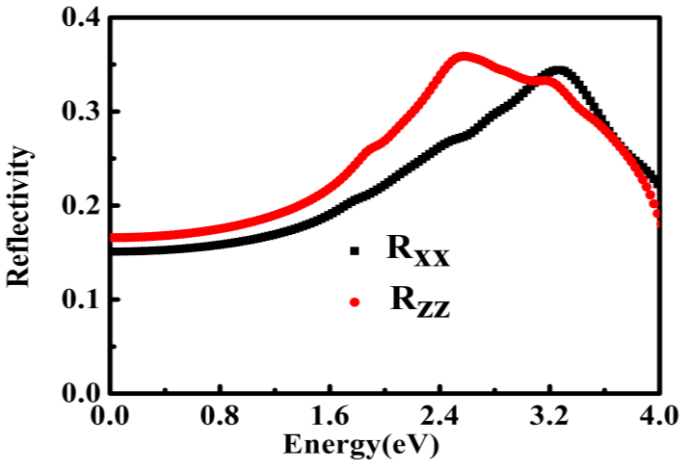

Figure III-7: Reflectivity of $CH_3NH_3PbI_3$ for XX and YY directions.

Also, the reflectivity $R(E)$ of $CH_3NH_3PbI_3$ is calculated and displayed in Figure III.7. In the visible range, it increases to 36% and 34% for the XX and YY directions, respectively. It confirms the good absorbance of the tetragonal $CH_3NH_3PbI_3$ in all directions.

III.3.4 Photovoltaic properties

Both physical quantities $R(E)$ and $\alpha(E)$ have been used to estimate the quantum efficiency Q_E, the open circuit voltage V_{oc}, the short circuit current density J_{sc}, as well as the electrical power. These parameters significantly describe the ability of the materials to be considered as a good candidate in photovoltaic devices. The determination of these parameters makes possible to overcome the technologic difficulties encountered in the consuming time development of such devices.

The open circuit voltage is related to the band gap E_g via the following equation [166,167]:

$$V_{oc} = \frac{E_g}{q} - \frac{nkT}{q}[\ln(J_{SG}) - \ln(J_{00})] \qquad (1)$$

Where E_g is the energy band gap, kT/q is the thermal voltage, n is the ideality factor, J_{sc} is the short-circuit current density, and J_{00} is the reverse saturation current density. According to equation (1), the limit of the open circuit voltage is always equal or below the bandgap energy. The second part of this equation related to the temperature is equal 0 when T = 0 K. Since the E_g is determined from DFT calculations performed at T = 0K, the V_{OC} is obtained through the relationship $V_{oc} = \frac{E_g}{q}$ where q is an electron charge. We obtained 1.79 V being higher than the experimental value which is V_{OC} = 1.2 V. This deviation between the experimental and measurements results is probably due to resistances established during measurements or charge accumulation between material layers of the device. The recombination process of charge carriers can also reduce the experimental V_{OC}.

The quantum efficiency $Q_E(E)$ of the $CH_3NH_3PbI_3$, which is an important parameter for its proportionality to the quantity of electrons/ holes generated by semiconductors is computed as well. This physical parameter is obtained from the absorption α(E) and the reflectivity R(E) reported in Figure III.6.b and Figure III.7, respectively. The $Q_E(E)$ is expressed using the equation (2):

$$\boldsymbol{Q_E = (1 - R(E))(1 - e^{-\alpha(E)t})} \qquad \textbf{(2)}$$

The *t* parameter is the thickness of the sample. This equation is written considering the first and the second reflections as well as the first transmission. In Figure III.8, we report our computed $Q_E(E)$ for a thickness t = 600 nm and available experimental $Q_E(E)$ for comparisons. In visible range, analysis reveals that the calculated quantum efficiency $Q_E(E)$ reaches a maximum of 75%, being in nice agreement with available experimental quantum efficiencies for $CH_3NH_3PbI_3$ compound reported in references [168–170].

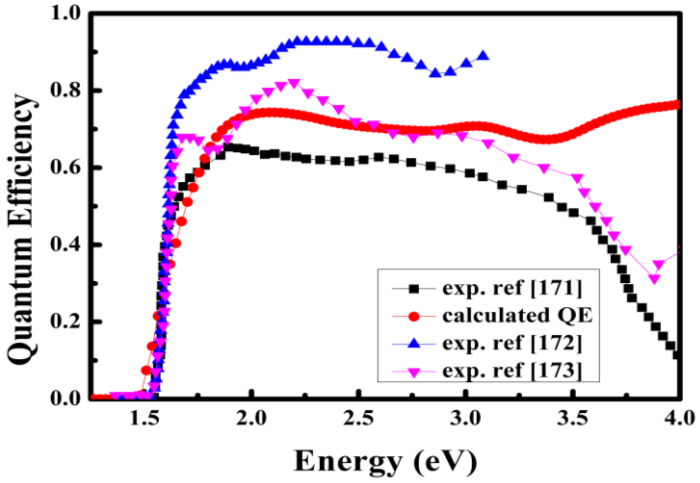

Figure III-8: Calculated quantum efficiency of $CH_3NH_3PbI_3$ compared to the experimental data.

Moreover, in the present work we report the pertinent manner to calculate the short circuit current J_{sc} from ab initio calculation using the FLAPW method with GGA-PBE approximation. From the quantum efficiency $Q_E(E)$ as well as the spectral irradiance $\phi(E)$ displayed in Fig. 7, we calculate the photocurrent versus the photon energy E using the equation (3).

$$\boldsymbol{I_{ph}(E) = \phi(E) Q_E(E)} \qquad \textbf{(3)}$$

Calculations of the $\phi(E)$ are performed using spectral irradiance AM1.5G [34] ranging from 0.5 to 4.0 eV. The sample thickness t is set to 600 nm. As seen in Figure III.9, the $I_{ph}(E)$ increases with the photon energy and reaches a maximum of 19 mA/cm² when photon energy approaches 1.7 eV. Then, it lowers to 0 mA/cm^2 when the energy is higher than 4.0 eV. The $I_{ph}(E)$ is re related to the mobility charge carrier and its maximum is due to the maximum of photons quantity coming from incident light at 1.7 eV.

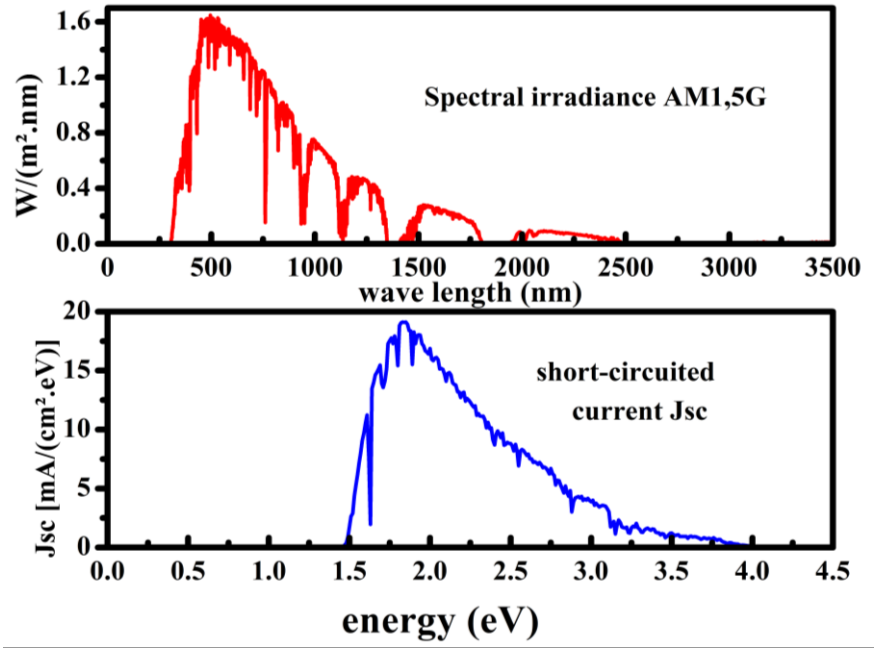

Figure III-9: The $\boldsymbol{\phi(E)}$ spectral irradiance AM1.5G used in our calculation and the photocurrent I_{ph} of $CH_3NH_3PbI_3$ versus photon energy.

It is worthy noticing that we consider J_{sc} as the sum of I_{ph} over wavelength λ or energy E of the visible light. We express J_{sc} via the equation (4):

$$\boldsymbol{J_{sc} = \int_{E1}^{E2} I_{ph} dE = \int_{E1}^{E2} \phi(E) Q_E(E).dE} \qquad \textbf{(4)}$$

E_1 is the bottom of the conduction band and E_2 is defined as the highest energy for the $\phi(E)$ spectral irradiance AM1.5G. The short circuit current J_{sc} is obtained by performing the

integral of equation over the 1.7 eV - 4.0 eV range. Our calculations, for which the thickness is set to t =600 nm, reveals a J_{sc} = 20 mA/cm which is in a good accordance with experimental data (20mA/cm) from reference [173].

Furthermore, we performed calculations of J_{sc} versus the t thickness (J_{sc} (t)) and obtained results are reported in Figure III.10. Analysis of this figure gives evidence of a good agreement of our J_{sc}(t) with available experimental data [172] as well as with previously theoretical results obtained from other calculation methods [173]**.** As main evidence, the saturation of J_{sc} (t) is reached when the thickness is about 400 nm. This result is a major key to optimize the active layer thickness in photovoltaic device, because it fixes the accurate thickness value of the material giving a maximum of charge carrier and presents a minimum of the electrical resistance.

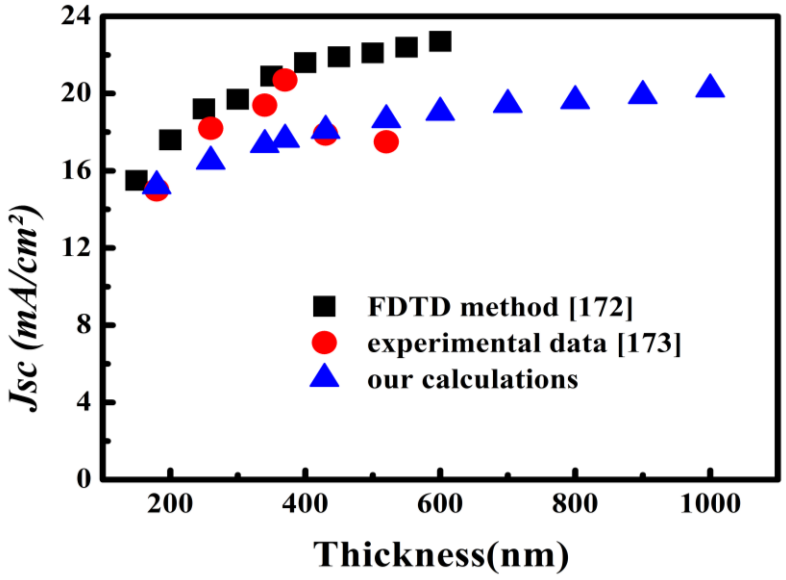

Figure III-10: The calculated and the experimental short circuit current as a function of the thickness of $CH_3NH_3PbI_3$.

The $CH_3NH_3PbI_3$ layer thickness was varied from 100 nm to 600 nm to examine the thickness effect on the short circuit current (Figure III.11). This variation reveals a substantial effect on the short circuit current. As seen the value of J_{sc} increases from around 19.8 mA/cm^2 to 32.5 mA/cm^2. Therefore, we conclude that the thickness of 600 nm relatively gives a good result than other thicknesses.

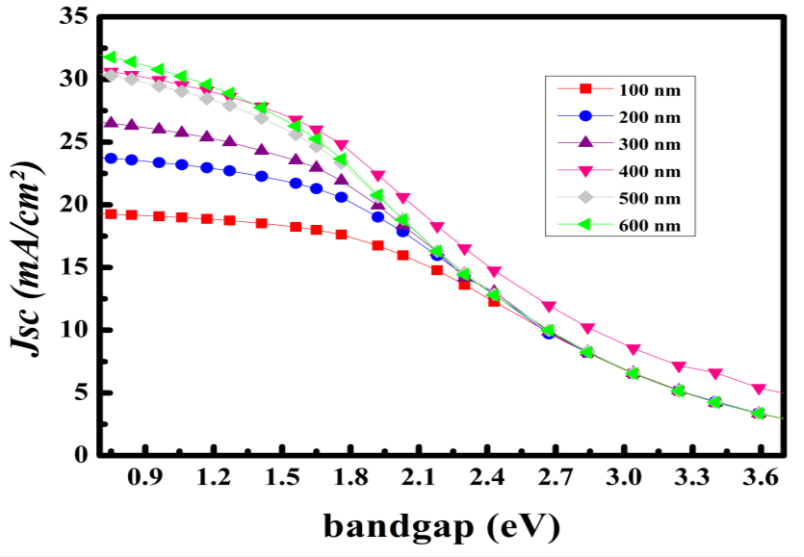

Figure III-11: Short circuit current as a function of bandgap for different thicknesses of $CH_3NH_3PbI_3$.

Since the pertinent parameter for photovoltaic device is the electrical power $P = V_{oc}J_{sc}$, we analyzed the dependence of both P and J_{sc} on the gap. Their variations are displayed in Figure III.12. in which we observe a maximum of the power P taking place at 1.5 eV. This observation specifies that the material with a gap close to 1.5 eV transfer more electrical charge. In other word, materials showing such gap value are potentially able to be used in photovoltaic devices with a good efficiency.

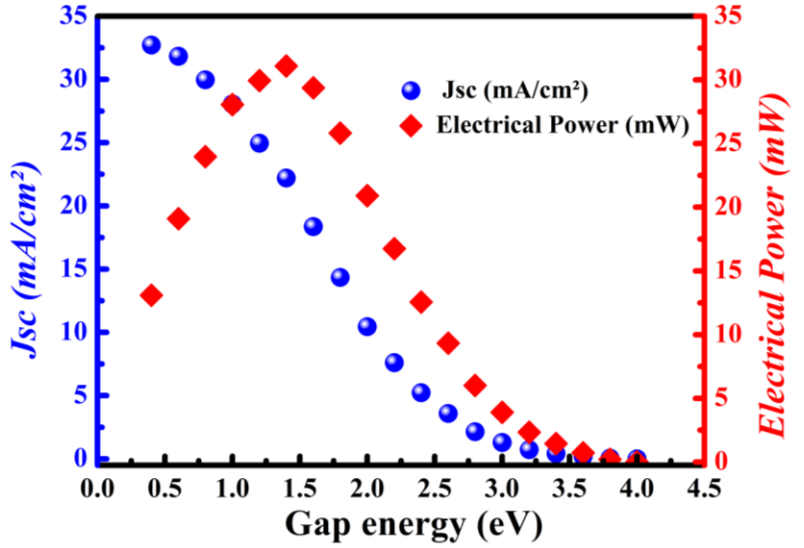

Figure III-12: The short circuit current and the electrical power versus the band gap value of $CH_3NH_3PbI_3$.

Finally, we underline that our proposed method based on ab initio calculation is revealed very useful and fast to evaluate and predict the photovoltaic quality of a given material

expressed via V_{OC}, J_{sc}, Q_E, and P parameters. Moreover, the necessity of the consuming time device realization in order to know the photovoltaic efficiency can be substantially reduced if our present method is employed.

III.4 Conclusion

First-principle DFT based on FLAPW method is used to investigate the optical and photovoltaic properties for a given material. The chosen material is the perovskite $CH_3NH_3PbI_3$ and DOS results are in accordance with previously results obtained from similar method calculations. Then, these results are used as input to calculate optical and photovoltaic properties. The reflectivity and the absorption coefficient are computed and the last one agrees with the experimental data. The pertinent photovoltaic parameters such as quantum efficiency Q_E, short circuit current J_{sc}, the open voltage V_{oc}, and the electrical power P are computed as well and compared to the available measurements. We obtained a good accordance between our calculations and measurements. As consequence, a useful and fast method to evaluate the efficiency of a given photovoltaic material is proposed.

Chapter IV:
Electronic, optical, and magnetocaloric properties of $(C_6H_{10}N_2)_2[Co(H_2O)_4P_2Mo_5O_{23}].6H_2O$

IV.1 Introduction

Over the previous decades, attracted extensive attention has been paid to the crystallization of new multifunctional Polyoxometalates (POMs) materials due to their tunable functionality, remarkable properties, structural diversity, defined size and shape [179–181]. All these properties make them highly potential candidates to a prospective application in the field of magnetic, medicine, catalyze, as well as optoelectronic materials [182–186]. These metal-inorganic family present unique behaviors such as good stability at ambient temperature [187] and can form a motivating structure, by coordinating with transitional metal ions [184,188,189]. Several experimental and theoretical studies of Polyoxometalate have been reported recently [190,191]. The prototypical structure of Polyoxometalate (POMs) cluster materials can be presented by the following general formula: $[M_mO_y]^p$ isopolyanions or $[X_xM_mO_y]^q$ Heteropolyanions, where M is usually Mo^{6+}, W^{6+}, V^{5+}, Nb^{5+}, or Ta^{5+}, or a mixture of these elements. Here, X is the main group of transition-metal heteroatom [192,193]. Ying Ma & al have been shown that the hydrothermal technique is an effective method to prepare well-defined novel structural polyoxometalate compounds containing transition metal complexes [194]. The presence of transitional metals cations in POMs compounds and their ability to accept a large number of electrons with small structural modifications influences the electronic, electric, optical, and the magnetic properties, and increase the possibility of being used for applications in diverse fields [195–199]. The stability of the polyoxometalates clusters is due to the organic ligands and to the strong hydrogen bonds. The conduction bands in the POM clusters have the capacity to promote the electron transfer and trap them. This process allows to retard and minimize the exciton recombination in solar cells [200–203]. In the last few years, Density Functional Theory calculations have been used in the computational chemistry to better understand and rationalize the contribution of the transitional metal in the electronic, optical, and magnetic properties of POMs complexes [204–210].

To our knowledge, POMs clusters are unexplored so far for the photovoltaic applications despite their promising characteristics. For that reason, our work is focused on studying the photovoltaic and the magnetic properties of a new hybrid compound which is based on Strandberg type P_2Mo_5 polyoxoanions and cobalt cations.

Accordingly, this paper focuses on the analysis of the electronic structure. Computational details describing the electronic properties using GGA approximation are presented. The originality of our work is the comparison between the experimental and the theoretical optical properties, such as the reflectivity, and the absorption coefficient for the photovoltaic

application, as well as the study of the magnetocaloric properties. As a continuity of our previous work [208], we Investigate here in detail the theoretical morphological properties and the computational optical properties such as the reflectivity and the absorption coefficient for the photovoltaic application as well as the magnetocaloric effect of $(C_6H_{10}N_2)_2[Co(H_2O)_4P_2Mo_5O_{23}].6H_2O$.

IV.2 Computational details

In this study, we used density functional theory, within the full-potential linearized augmented plane waves (PF-LAPW) method, as implanted in the Wien2K package [156]. The exchange-correlation energy is described by the generalized gradient approximation (GGA) proposed by Perdew, Burke, and Ernzerhof [157]. The Kohn-Sham equation and energy functional were evaluated consistently. The space was divided into the interstitial and the non-overlapping muffin-tin spheres centered on the atomic sites. The basis function inside each atomic sphere consisted of linear expansion of the radial solution of a spherically potential multiplied by spherical harmonics. In the interstitial region, the wave function was taken as an expansion of plane waves and no shape approximation for the potential was introduced in this region which is consistent with the full potential method. The core electrons were described by atomic wave functions which can be solved relativistically using the current spherical part. The FP-LAPW calculations were performed using the crystal structure parameters deduced from our X-ray diffraction refinement. Spin-polarized potential is considered for our calculations. The atomic muffin-tin (MT) spheres, supposed not to overlap with each other, are taken as 1.80, 2.10, 1.64, 1.04,1.12 and 0.55 a.u. for Co, Mo, P, N, C and H atoms respectively. The material crystalizes in the triclinic structure type ($a \neq b \neq c$) within space-group P, which is stable under ambient conditions as seen in Figure IV.1. The gap energy, which defines the separation of the valence and core state, was chosen equal to -6.0 R_y. The largest reciprocal vector G in the charge Fourier expansion, G_{max}, was equal to 12 and the cut-off energy corresponding to the product of the muffin-tin radius and the maximum reciprocal space vector, $R_{MT}.K_{max}$, was equal to 7. Inside the atomics spheres, the potential and charge density are expanded in crystal harmonics up to $l_{max} = 6$. Calculations are performed with 38 in equivalent k-points in the irreducible Brillouin zone. Such a value is large enough to ensure the magnetic moment. The convergence criterion was chosen to be the total energy and set at 10^{-4} eV.

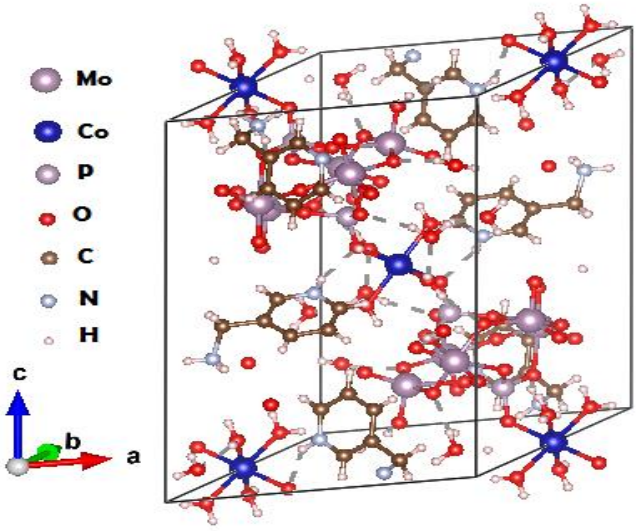

Figure IV-1: Crystal structures of $(C_6H_{10}N_2)_2[Co(H_2O)_4P_2Mo_5O_{23}].6H_2O$

IV.3 Experimental details

The material was synthesized according to the protocol described in our previous work [208]. The light absorption and UV–Vis diffuse reflectance spectra were obtained using the Perkin–Elmer spectrophotometer type instrument.

For magnetocaloric effect study, magnetization isotherms were measured for $(C_6H_{10}N_2)_2[Co(H_2O)_4P_2Mo_5O_{23}].6H_2O$ system up to a maximum magnetic field of 5 T over a temperature range of 190 to 300 K at every 2 K interval using a high sensitive superconducting quantum interference device (SQUID) magnetometer (Quantum Design).

IV.4 Results and discussion

IV.4.1 Structural properties

Our obtained XRD pattern is presented and revealed that it is in excellent agreement with $(C_6H_{10}N_2)_2[Co(H_2O)_4P_2Mo_5O_{23}].6H_2O$ simulated pattern. All refined crystallographic structure is gathered in our previous work [208]. The purity phase of the sample is illustrated in Figure.IV.2. The XRD peaks show that this material crystallizes in the triclinic phase (space group $P\bar{1}$), with the lattice constants *a* = 11.1205 Å, b = 11.7576 Å, and *c* = 16.7869 Å.

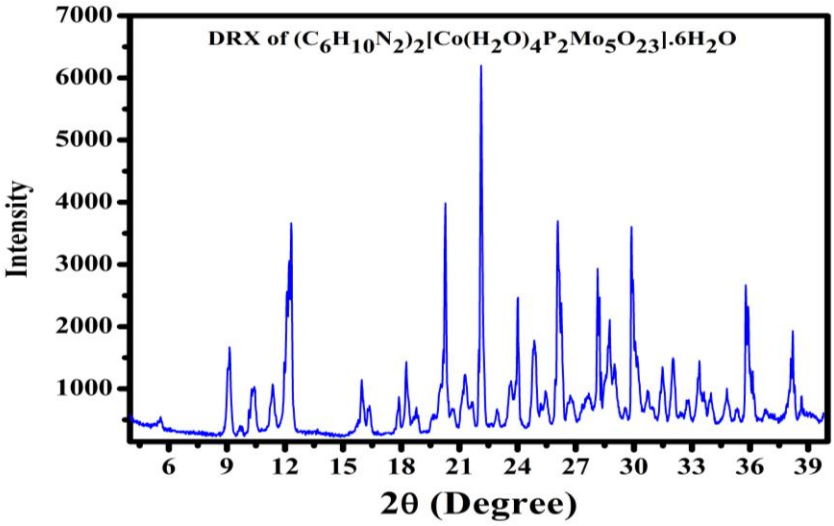

Figure IV-2: XRD pattern of $(C_6H_{10}N_2)_2[Co(H_2O)_4P_2Mo_5O_{23}].6H_2O$.

The theoretical morphological scheme of the Crystal is established via the WinXMorph software, taking into account only the point group and the crystal cell parameters [209], using the Bravais-Friedel and Donnay-Harker (BFDH) law. According to BFDH law, the growth rate of the plane is inversely proportional to the interplanar distance d_{hkl}. This morphological scheme is shown in Figure. IV.3. Table IV.1 list the crystalline forms {hkl} equivalent faces and their corresponding d_{hkl} for the synthesized compound.

Table IV-1: The crystalline forms {hkl} equivalent faces and their corresponding dhkl for the synthesized compound.

Hkl	001	010	100	01-1	-101	-110	-111
d_{hkl}	0.773	1.248	1.326	1.371	1.415	1.450	1.620

From the Table 1, it can be seen that d_{hkl} of {001} face is the largest subsequently {010} face, {100}, {01-1}, {-101}, {-110} and {-111}. According to BFDH rule the {001} facet is thus designated as having more morphological importance than the other faces.

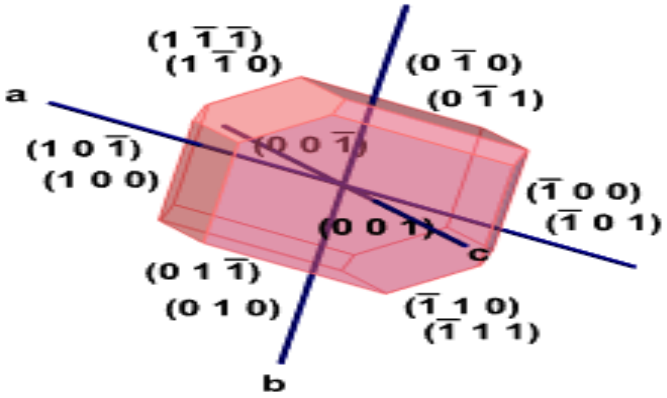

Figure IV-3: The morphological scheme of $(C_6H_{10}N_2)_2[Co(H_2O)_4P_2Mo_5O_{23}].6H_2O$ crystal.

IV.4.2 Electronic properties

The density of states (DOS) computed from the FP-LAPW method implanted in Wien2k code [156] is displayed in Figure. IV.4. In our previous work [208], we calculated the density of states with 16 in equivalent k-point, but in this work, we increased to 38 in equivalent k-point, in order to study k-point effect on our calculations. The Fermi level is taken as an energy reference.

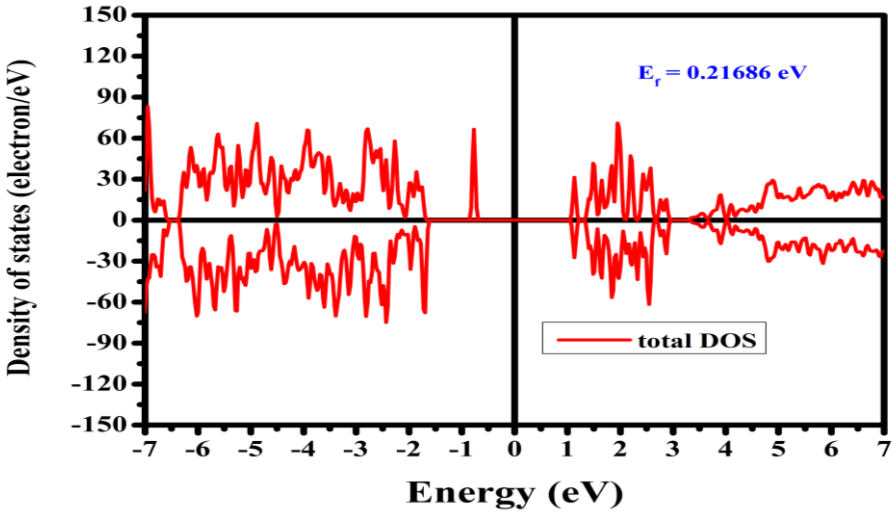

Figure IV-4: Total DOS of $(C_6H_{10}N_2)_2[Co(H_2O)_4P_2Mo_5O_{23}].6H_2O$ using FP-LAPW calculations

The negative energies correspond to the occupied state whereas the positive energies correspond to the unoccupied states. At negative energies, the total DOS (Figure. IV.4) points out to a broad band on [-7 eV; -1.68 eV] range and a peak located at -0.69 eV. The band originates from hybridization between Co-d, C-p, Mo-d, O-p states. The small contribution of P-p states is also observed in this band. The peak observed at -0.69 eV is a contribution from the d states of Co atoms.

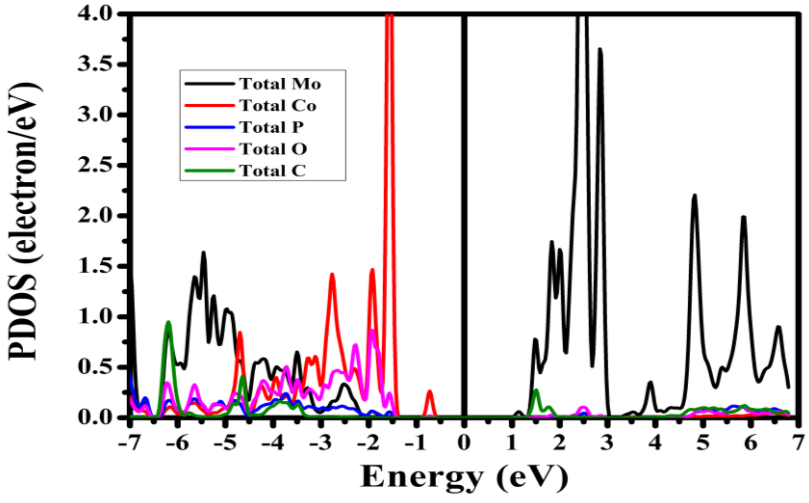

Figure IV-5: Partial DOS of $(C_6H_{10}N_2)_2[Co(H_2O)_4P_2Mo_5O_{23}].6H_2O$ using FP-LAPW calculations.

As seen in Figure. IV.5, the unoccupied band ranging from 1.71 eV to 7 eV, consists of hybridization between Mo-d and C-p. with a major contribution of Mo-d orbital is observed as well (Figure. IV.6). The bandgap of the spin up is about 1.8 eV whereas the spin down gap is found about 2.65 eV. The experimental bandgap obtained from the optical measurements is around 1.81 eV [208]. The total density of states up and total density down are revealed asymmetrical with respect to the energy axis. This observation underlines that our compound is in a magnetic state. This magnetism is induced by the presence of the Co atoms in the lattice as reported in our previous work [208].

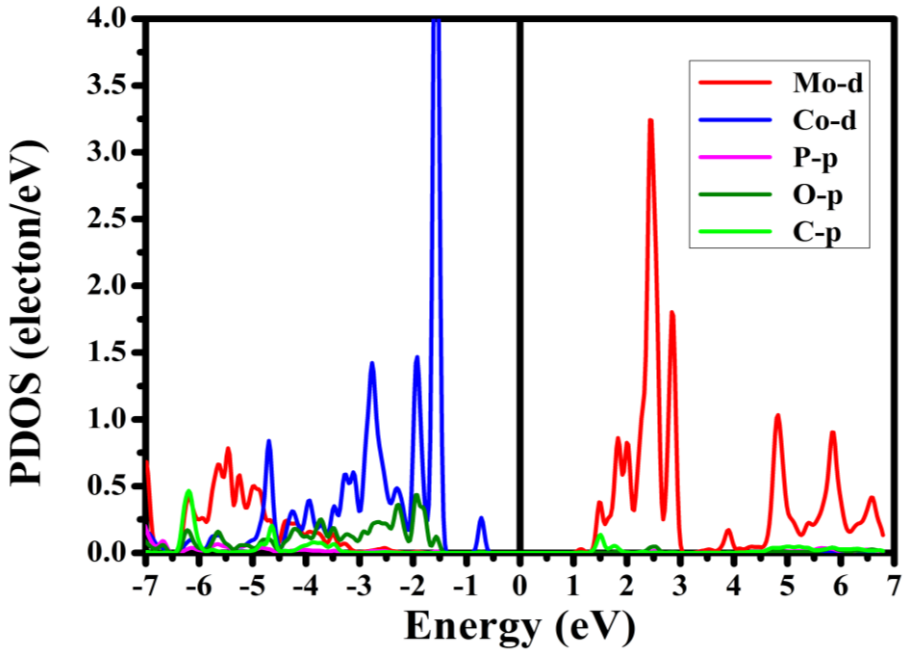

Figure IV-6: Partial DOS of $(C_6H_{10}N_2)_2[Co(H_2O)_4P_2Mo_5O_{23}].6H_2O$ using FP-LAPW calculation.

IV.4.3 Optical properties

The optical properties are extracted from dielectric function ε(ω) that generally describes the interaction between photons and electrons. The linear optical properties in solids can be described by the complex dielectric function [210,211]:

$$\varepsilon = \varepsilon_1(\omega) + i\varepsilon_2(\omega) \qquad (1)$$

Where $\boldsymbol{\varepsilon_1}$ (ω) represents the real part of the dielectric function indicating the dispersion of the incident photons by the material and $\boldsymbol{\varepsilon_2}$ (ω) is the imaginary part of the dielectric function which corresponds to the absorbed energy of the material.

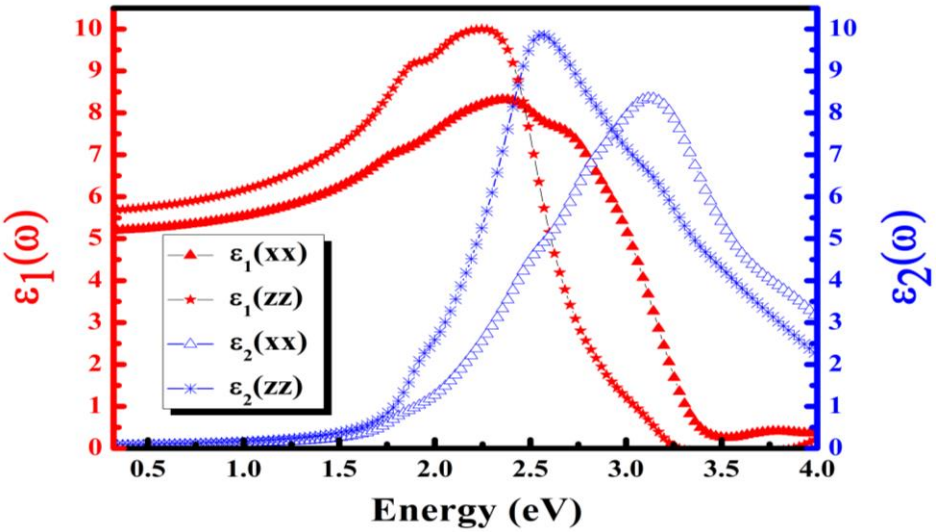

Figure IV-7: Dielectric function of $(C_6H_{10}N_2)_2[Co(H_2O)_4P_2Mo_5O_{23}].6H_2O$ the imaginary part and the real part versus energy.

Figure IV.7. illustrated the calculated result for real $\boldsymbol{\varepsilon_1}$ (ω) and imaginary parts $\boldsymbol{\varepsilon_2}$ (ω) of the dielectric function of our compound, exhibited in the range 0-4 eV. It is clear from the graph that the imaginary part indicates the minimum absorption before 1.5 eV energy, and it increases gradually to reach a maximum of 3.12 eV and 2.56 eV for XX and ZZ direction respectively. Similarly, it decreases smoothly with any further increase of the energy values. This confirms that the compound has a good absorption in the visible range. The calculated static dielectric constant $\boldsymbol{\varepsilon_1}$ (0) $_{xx}$ and $\boldsymbol{\varepsilon_1}$ (0) $_{zz}$ are 5.5eV and 5.7 eV respectively. Therefore, the material's response is depending on the direction which means that the material has considerably an anisotropic behavior due to the difference between the XX and ZZ directions.

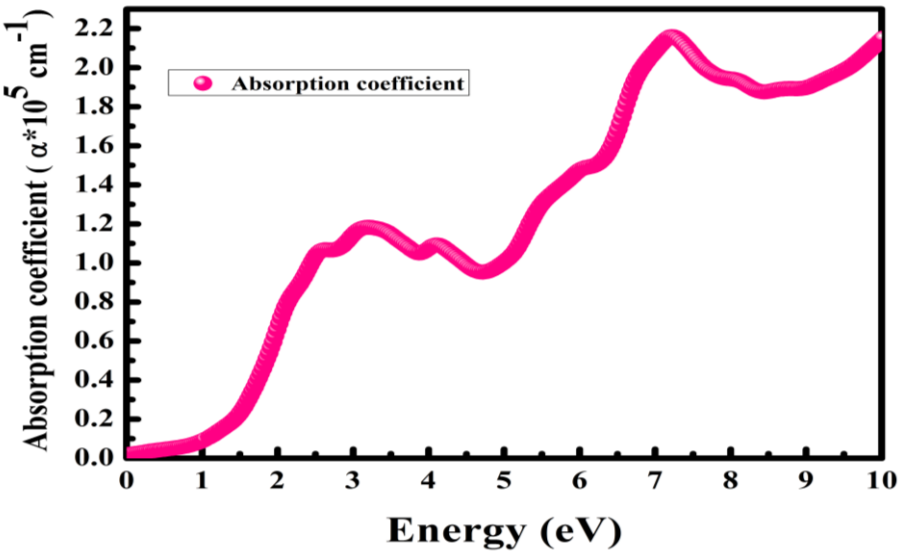

Figure IV-8: Dielectric function of $(C_6H_{10}N_2)_2[Co(H_2O)_4P_2Mo_5O_{23}].6H_2O$ the imaginary part and the real part versus energy.

The calculated absorption coefficient as a function of photon energy for the hybrid complex $(C_6H_{10}N_2)_2[Co(H_2O)_4P_2Mo_5O_{23}].6H_2O$ with GGA method is plotted in Figure IV.8. It shows that this material has a large absorption power in the visible range, it increases with increasing energy to reach a maximum of $1.2*10^5$ cm $^{-1}$ at 3.2 eV, and decreases smoothly, above 4.7 eV, the mean peak is more important, it is situated at 7.2 eV and reaches a maximum of $2.2*10^5 cm^{-1}$.

Experimentally, the absorption coefficient is obtained from the measured absorbance, using the simple following equations [210,213]:

$$A = \exp(-\alpha d) \quad (2)$$

$$\alpha = \frac{1}{d}\ln\left[\frac{(1-R)^2}{T}\right] \quad (3)$$

$$\alpha = 2.303\frac{A}{d} \quad (4)$$

d is the sample thickness, R and T are the reflectance and the transmission, A is the absorbance, and α is the absorption coefficient (cm^{-1}).

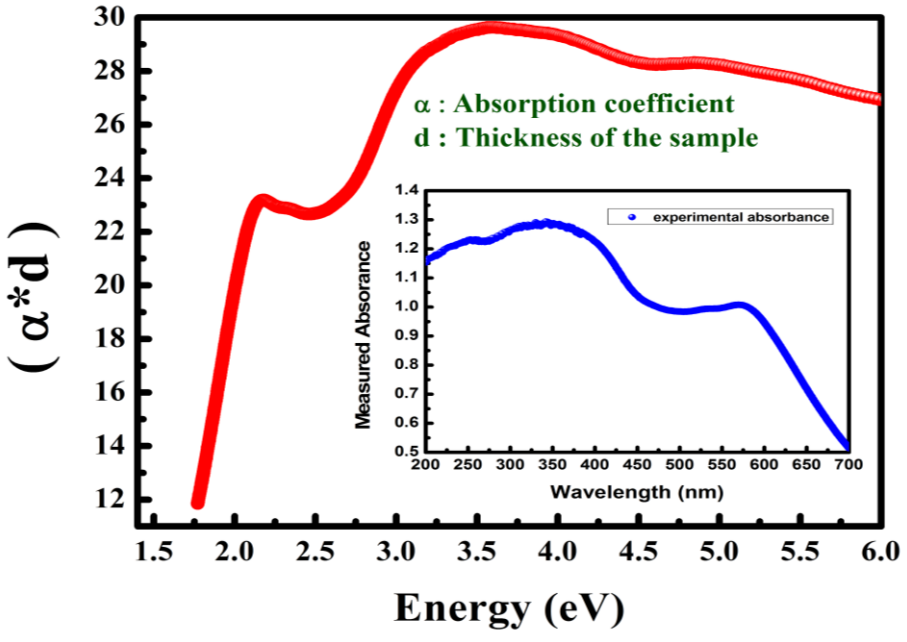

Figure IV-9: The experimental absorption coefficient obtained from measured absorbance of $(C_6H_{10}N_2)_2[Co(H_2O)_4P_2Mo_5O_{23}].6H_2O$.

In our work the experimental absorption coefficient is calculated from the measured absorbance by using equation (4), without taking sample thickness in the calculation as plotted in Figure IV.9. This figure shows a large absorption of light in the visible range, which starts

from the energy 1.75 eV to reach a maximum at the energy of 3.37 eV. According to Figure IV.9. $(C_6H_{10}N_2)_2[Co(H_2O)_4P_2Mo_5O_{23}].6H_2O$ demonstrates a good quality of absorbance in the visible range, which is motivating for solar cells applications.

The theoretical and experimental band gaps E_g of $(C_6H_{10}N_2)_2[Co(H_2O)_4P_2Mo_5O_{23}].6H_2O$ could be determined using the following model law: $[\alpha * h\nu]^n$, where α is absorption coefficient, $h\nu$ is the energy of incident photons, and n may be equal to ½ for indirect transition or 2 for a direct transition [214]. For our complex, the bandgap obtained from the theoretical absorption coefficient is 1.8 eV as seen in Figure IV.10, which is in good agreement with the experimental bandgap reported in our previous work [208], and the bandgap indicated by the total density of states.

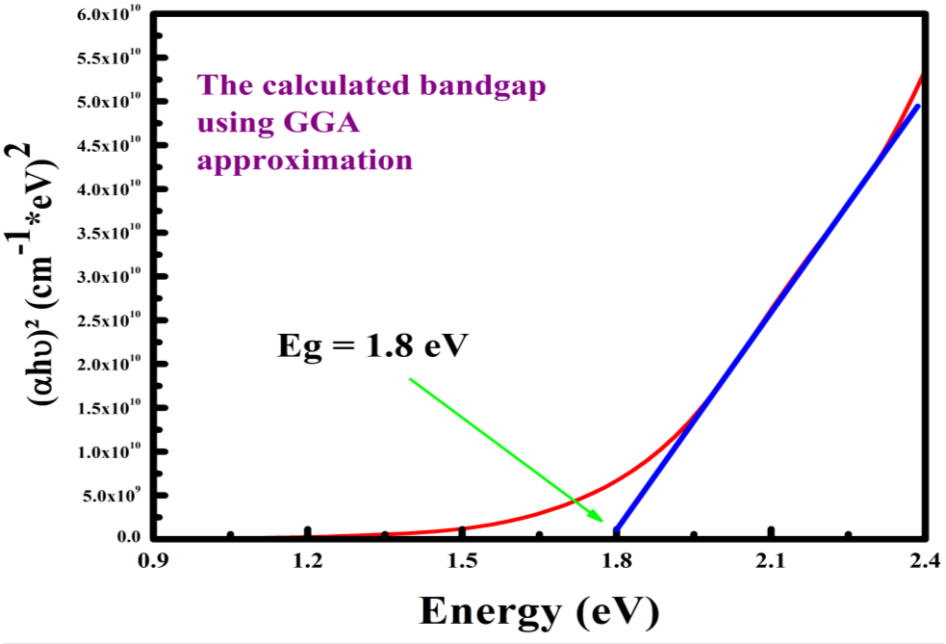

Figure IV-10: The experimental and the theoretical band gap using tauc equation of $(C_6H_{10}N_2)_2[Co(H_2O)_4P_2Mo_5O_{23}].6H_2O$.

As it is reported in Figure IV.11, we normalized the absorption coefficient to compare the experimental and theoretical investigations for the organic-inorganic hybrid complex $(C_6H_{10}N_2)_2[Co(H_2O)_4P_2Mo_5O_{23}].6H_2O$. The results show that the quality of the shapes of the experimental and theoretical curves is in good accordance, with the good response to the incident light, this confirms the high absorption power in the visible and UV energy range, and proves the potential of this material for PV and optoelectronic applications.

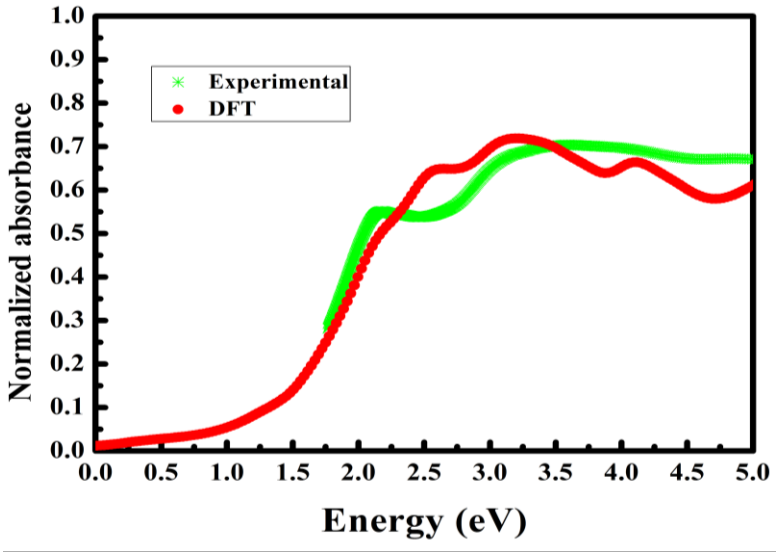

Figure IV-11: The experimental and the theoretical normalized absorption coefficient of $(C_6H_{10}N_2)_2[Co(H_2O)_4P_2Mo_5O_{23}].6H_2O$.

The calculated reflectivity using GGA approximation as a function of photon energy for $(C_6H_{10}N_2)_2[Co(H_2O)_4P_2Mo_5O_{23}].6H_2O$ is plotted in Figure IV.12. This figure shows that this compound reflectivity not exceeding about 21%, it starts at 6.5%, and increases as well to 19,7% for 4.39 eV. As well, it decreases to 8.7%. this result is good with the experimental results reported in our previous work [208]**.** Consequently, these results demonstrate that the material studied has a weak reflectivity, which makes it a promising candidate for photovoltaic use.

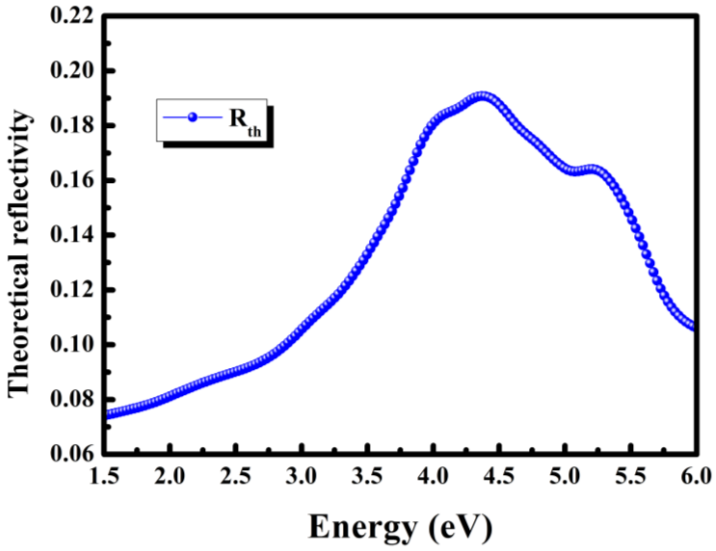

Figure IV-12: The calculated reflectivity of $(C_6H_{10}N_2)_2[Co(H_2O)_4P_2Mo_5O_{23}].6H_2O$.

The energy loss function of $(C_6H_{10}N_2)_2[Co\ (H_2O)_4P_2Mo_5O_{23}].6H_2O$ versus energy is presented in Figure IV.13. As seen, the evolution of the loss energy spectrum appears more

important in the UV range compared to the visible range. In fact, the spectra show an anisotropic nature between L_{xx} and L_{zz}. Moreover, the energy loss increases smoothly to reach the first maximum in the UV range about 65% and 62% for XX and ZZ directions respectively. Around 6.45 eV and 5.68 eV, the curve reaches the second maximum of about 36% for XX and ZZ directions.

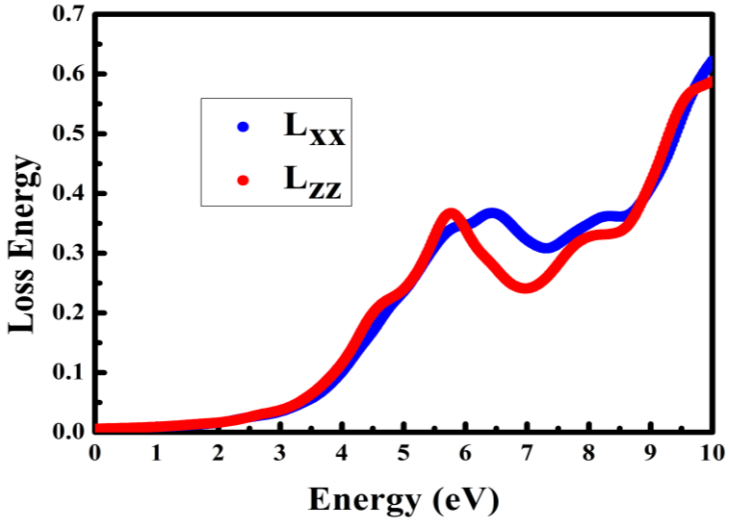

Figure IV-13: Energy loss spectrum of $(C_6H_{10}N_2)_2[Co(H_2O)_4P_2Mo_5O_{23}].6H_2O$ Complex.

From the optical properties observed in the visible region, the $(C_6H_{10}N_2)_2[Co(H_2O)_4P_2Mo_5O_{23}].6H_2O$ can be considered as promising candidate for visible optical devices namely in photovoltaic application. In addition, the fluorescent emission results reveal that the complex belongs to the blue luminescent compounds.

IV.4.4 Second-order ferromagnetism and magnetocaloric effect

The isothermal magnetization around T_C is measured for the analysis of the critical properties, as gives in Figure IV.14. In addition, The M^2 vs. H/M curve should appear as straight lines in the high-field range in the Arrott plot. The intercept of M^2 as a function of H/M on the H/M axis is negative/positive below/above TC. The line of M^2 vs. H/M at TC should cross the origin. According to the criterion proposed by Banerjee [215], the order of the magnetic transition can be determined from the slope of the straight line: the positive slope corresponding to the second-order transition whiles the negative slope to the first-order one.

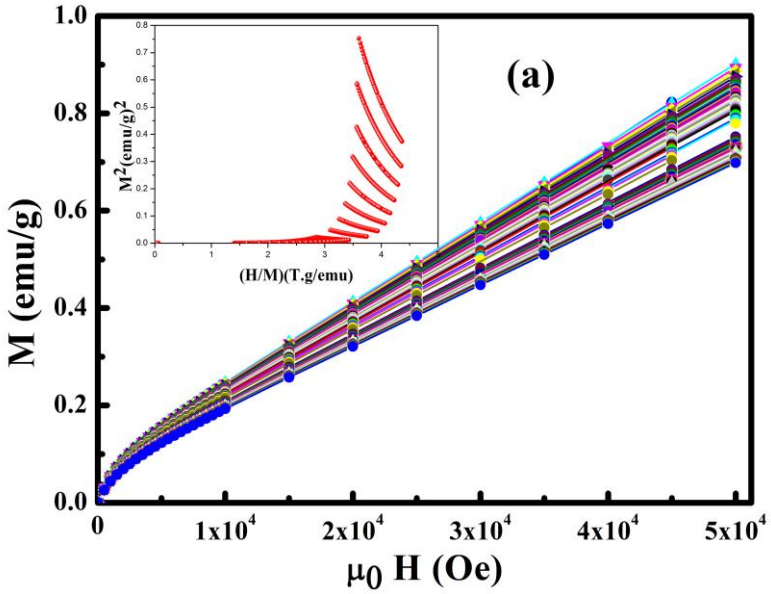

Figure IV-14: Magnetization isotherms measured at different temperatures between 190 and 300 K with 5 K interval.

Figure IV.15, shows the Arrott plot of M^2 vs. H/M for studied complex around T_C. The positive slope of the M^2 vs. H/M relation indicates that the PM-FM phase transition is a second-order one. all curves in the Arrott plot are nonlinear and show an upward curvature even in the high-field region, which indicates that $\beta = 0.5$ and $\gamma = 1$ are satisfied according to the Arrott-Noakes equation of state $(H/M)^{1/\gamma} = (T-T_C)/T_C + (M/M_1)^{1/\beta}$ [216]. Such results improved that mean-field theory with $\beta = 0.5$ and $\gamma = 1$ is valid for studied the magnetic properties of the materials.

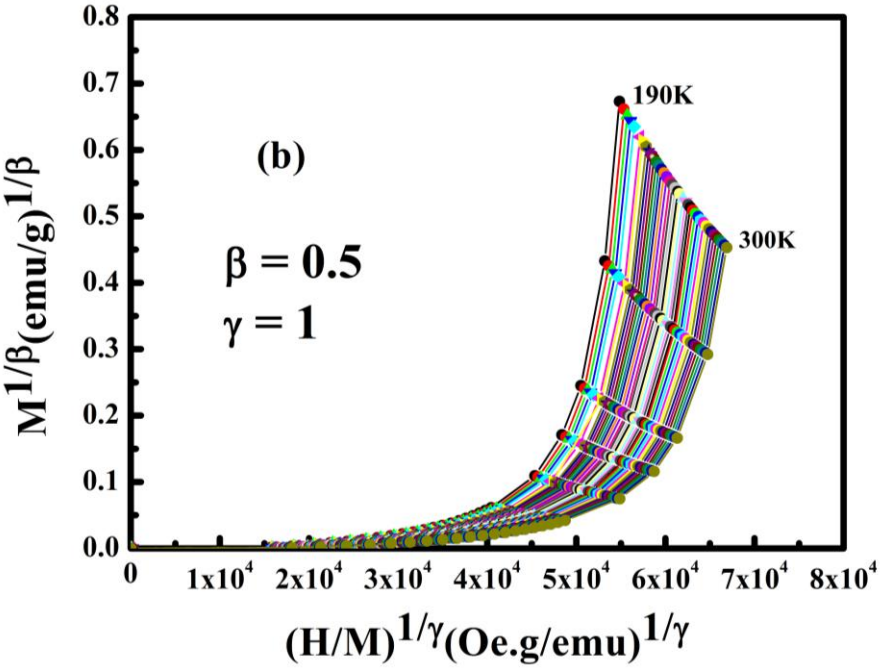

Figure IV-15: (b)The M^2 vs H/M plots for representative temperatures around the T_C.

Finally, to elucidate the influences of the magnetic transition and long-range ferromagnetism on the magnetocaloric effect (MCE) in **(**$C_6H_{10}N_2)_2[Co(H_2O)_4P_2Mo_5O_{23}].6H_2O$, the magnetic entropy change $\Delta S_M(T)$ is calculated from a family of isothermal *M-H* curves using the Maxwell relation $\Delta S_M(T) = \mu_0 \int_0^{Hmax} \left(\frac{dM}{dT}\right) dH$. Where *M* is the magnetization, *H* is the magnetic field, and *T* is the temperature.

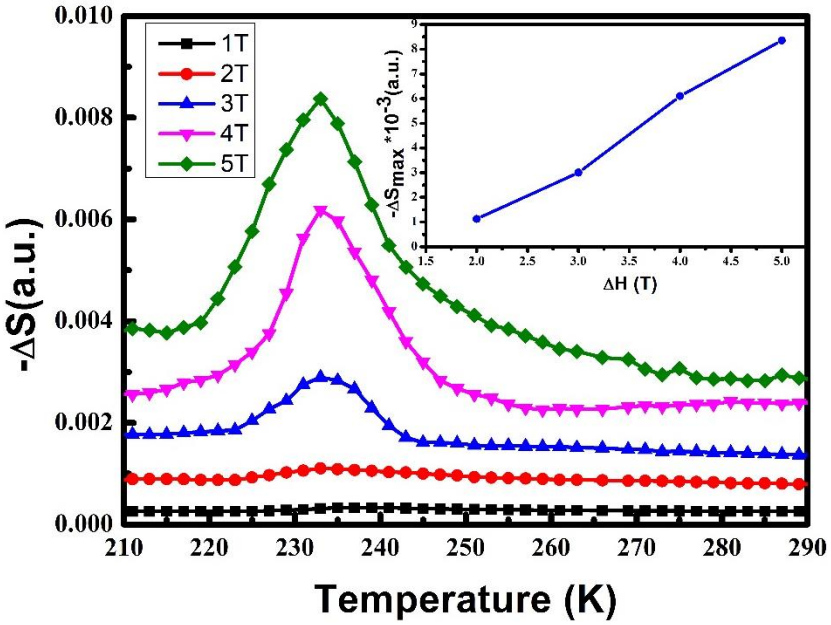

Figure IV-16: Magnetic entropy changes as a function of temperature extracted from *M-H-T* curves via the Maxwell relation. Inset magnetic entropy vs applied field.

Figure IV.16, shows the magnetic entropy change $\Delta S_M(T)$ as a function of temperature for different magnetic field changes up to 5 T. From Fig.13, $\Delta S_M(T)$ reaches a value of 8.2 $*10^{-3}$ a.u. at 232 K for *H*=5 T, indicating low candidate to magnetocaloric effect (MCE) by the studied material.

Figure IV.16, inset shows that the maximum of entropy almost varies linearly with the applied magnetic field.

The weak magneto-caloric effect obtained for our synthesized compound substantiates that this material can be considered as a 1D homometallic coordination polymer, which makes it a candidate to construct metal-inorganic frameworks with long-range ferromagnetic superexchange between Co(II) centers.

V.5 Conclusion

The ab initio density functional theory (DFT) calculations are performed in order to investigate the electronic and optical properties of the organic-inorganic hybrid material

$(C_6H_{10}N_2)_2[Co(H_2O)_4P_2Mo_5O_{23}].6H_2O$ synthesized, the lattice parameter values of the nanocrystals compound were obtained using X-ray diffraction (XRD). A density of states analysis showed that the highest contribution arises from 3d orbital of Co atom near the fermi level. Moreover, we determine the optical constants such as the absorption coefficient, the reflectivity, the energy loss function, and the real and imaginary part of the optical dielectric function. The magnetic properties present a low magnetocaloric effect. At last, we experimentally observed that the optical results are in good agreement with our theoretical results, and a wide application for this compound because of its multifunctional properties.

Chapter V: Electronic, and optical properties of organic-inorganic (Cu^{II} /Re^{VII})-heterobimetallic L-Arginine complex

V.1 Introduction

The metal-inorganic hybrid frameworks are considered as an emerging area of transition metal that provides diverse properties, for several applications [208,217–220]. However, the characteristics of these systems depend on the nature of both the transition metals and the organic components and have led to advances in numerous fields such as laser technologies, optical storage technologies, optical communication, magnetic field, and photovoltaics [221–226]. Meanwhile, the complexes of amino acids and peptides molecules derivatives are significant for their unique electrical, and optical properties [227, 228]. These materials are formed by Van der Waals interaction and hydrogen bonded networks and are considered as a Non-Linear optical material (NLO) compounds, such as L-Arginine phosphate monohydrate (LAP) which exhibits a nonlinear optical property [229]. Besides, the electronic charge distribution delocalization leads to an increase in the optical nonlinearity by increasing the mobility of electrons. All of the above properties have encouraged the development of amino acid crystals such as NLO materials [229–231]. Over the years, many transition metal complexes based on L-Arginine were developed [232–235]. The self-assembled networks between L-arginine and the self-assembly transition metal complexes have attracted much attention, owing to their design, physical and biological characteristics [236, 237]. These compounds are known not only for their chirality but also for their flexibility which tolerates a wide range of different properties [238]. A series of compounds of $[Cu(L\text{-}Arg)_2]_m(X).nH_2O$ with different counter-anions were studied by Yamauchi et al. [239, 240]. The results demonstrated that the Cu(II)-Arginine complexes architecture changed by changing the counter-anions nature [241]. In a previous work, we described the synthesis, design and characterization of the Cu^{II}/Re^{VII}- heterobimetallic complex of $[Cu(L\text{-}Arg)_2(ReO_4)_2$ as a rare example of heterobimetallic L-arginine complexes [242]. The major objective of this work is to investigate the electronic, dielectric, and optical properties of this heterobimetallic- L-Arginine compound, formulated as $Cu(L\text{-}Arg)_2(ReO_4)_2$. For this investigation, the full potential linearized augmented plane wave (FP-LAPW) method [156], within the generalized gradient approximation (GGA), as implanted in the Wien2k package [243] is used . No studies have been reported on theoretical calculations for the Cu-Arginine family. Most studies about Cu-arginine complexes have focused on synthesis and experimental characterization. This work provides a substantial opportunity to advance our knowledge of understanding the electronic, dielectric and optical properties, using the full potential linearized augmented plane wave (FP-LAPW) method. In addition, it allows to shed light on the correlation between the experimental

results and calculations. From the Kubelka-Munk function, the experimental band gap was estimated and compared with the calculated one. Similarly, the scattering coefficient is estimated from the calculated absorption coefficient using the Kubelka-Munk (K-M) function.

V.2 Computational details

In this study, we used the density functional theory within the full-potential linearized augmented plane wave (FP-LAPW) method as implanted in the Wien2k package[156]. The exchange-correlation energy is described by the generalized gradient approximation (GGA) proposed by Perdew, Burke, and Ernzerhof [244, 157]. The Kohn-Sham equation and energy functional were evaluated consistently. The space was divided into interstitial and non-overlapping "muffin tin" spheres centered on the atomic sites. The basis function inside each atomic sphere consisted of linear expansion of the radial solution of a spherical potential multiplied by spherical harmonics. In the interstitial region, the wave function was taken as an expansion of plane waves, and no shape approximation for the potential was introduced in this region which is consistent with the full potential method. The core electrons were described by atomic wave functions solved relativistically using the current spherical part. The FP-LAPW calculations were performed using the crystal structure parameters deduced from X-ray diffraction refinement [242]. The synthesized complex crystallizes in a chiral monoclinic structure as seen in Figure.V.1. Spin-polarized potential is considered for our calculations. The atomic muffin-tin (MT) spheres, was chosen not to overlap with each other, with values 1.71, 1.93, 1.21, 1.04, 1.09, and 0.56 a.u for Re, Cu, O, N, C, and H atoms respectively. The gap energy, which defines the separation of the valence and core state, was chosen equal to -8.0 Ry. The largest reciprocal vector G in the charge Fourier expansion, G_{max}, is chosen equal to 12 and the cut-off energy corresponding to the product of the muffin-tin radius and the maximum reciprocal space vector, $R_{MT}.K_{max}$, was set to 7. Inside the atomics spheres, the potential and charge density are expanded in crystal harmonics up to $l_{max} = 6$. Thus, the calculations are carried out with 50 equivalent k-points in the irreducible Brillouin zone. A convergence criterion was applied to the total energy, and set at 10^{-4} eV to ensure the calculated properties and the magnetic moment.

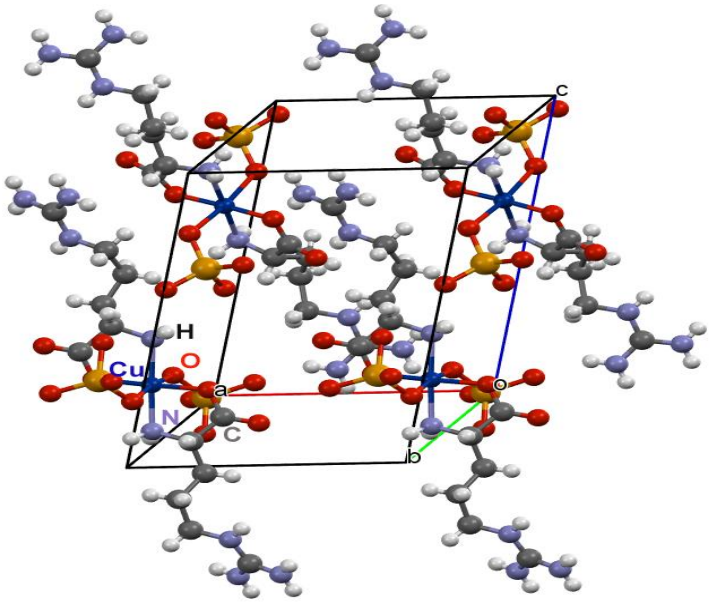

Figure V-1: $[Cu(L\text{-}Arg)_2(ReO_4)_2]$ monoclinic crystal structure.

V.3 Experimental details

The material was synthesized using the protocol described in our previous work [242]. The UV–Vis reflectance electronic spectrum was obtained on a Perkin–Elmer spectrophotometer type instrument Lambda-45, in the range of 400-850 nm, with a scan speed of 960 nm. min^{-1}, and an aperture of 4 nm coupled to an integration sphere type RSA-PE-20.

V.4 Results and discussion

V.4.1 Electronic properties

The density of states describes the distribution probability of the electron in the energy spectrum. The total and partial densities of states (DOS) of $Cu(L\text{-}Arg)_2(ReO_4)_2$ calculations are investigated using GGA approximation and reported in Figure V.2. From Figure V.2-a, it is obvious that the total DOS can be divided into three regions: the first region located from the lower valence band (LVB) to the upper valence band (UVB) between -8.5 eV to -0.7 eV. It is due to the mixture of Re, O, and C atoms in the lower valence band, and a huge contribution of Cu atoms mixed with N and O atoms, in the upper valence band from -5.2 eV to -0.7 eV as seen in Figure V.2-b. The second region, located in the conduction band, starts from 2.6 eV to 3.28 eV. This area result comes from the hybridization of d orbital of Re transition metal and p orbital of O atom, as seen in Figure V.2-c. The last region starting from 3.75 eV in the conduction band is related to the mixture of C and Re atoms with a slight contribution of O-p

states as plotted in Figure V.2-b. The non-symmetry between the major and the minor spins in the total DOS (Figure V.2-a) gives an indication of the magnetic behavior of the studied compound. From the partial DOS displayed in Figure V.2-b, the DOS of Cu atoms dominates on the negative energies range. The non-symmetry between the major and the minor spins for this DOS points out that the Cu atoms carry a magnetic moment which validates the compound magnetic behavior. The calculated moment of Cu is close to $0.51\mu_b$, whereas for the other atoms, the moment is equal to 0 μ_b. The calculated band gap of major and minor spin using GGA-PBE approximation is 3.7 eV, and 3.3 eV respectively. The Fermi level E_f taken as energy reference is found to be equal to 0.147 eV. The experimental band gap obtained from the Kubelka-Munk equation is around 3.62 eV which is in good concordance with our estimated band gap from the total density of states (Figure V.2-a). To better understand the origin of the optical properties, the partial densities of states are plotted in Figure V.2-c and analyzed. The optical phenomena originate from electronic transitions between bonds based on the known rule conditions $\Delta l = \pm 1$ where l = 0, 1, 2, 3 is the orbital quantum number. As seen in Figure V.2-c, d-Re and s-Re bands do not contribute at negative energies and take place at positive energies, which confirm that the Re valence band involving d^5s^2 is empty and oxidation number is +7. For O atoms, the p bands contribute only to the valence band at negative energies. That points out that this band is full and its oxidation number of O is -2. As a conclusion, the origin of the optical properties comes mostly from d bands of Re atoms.

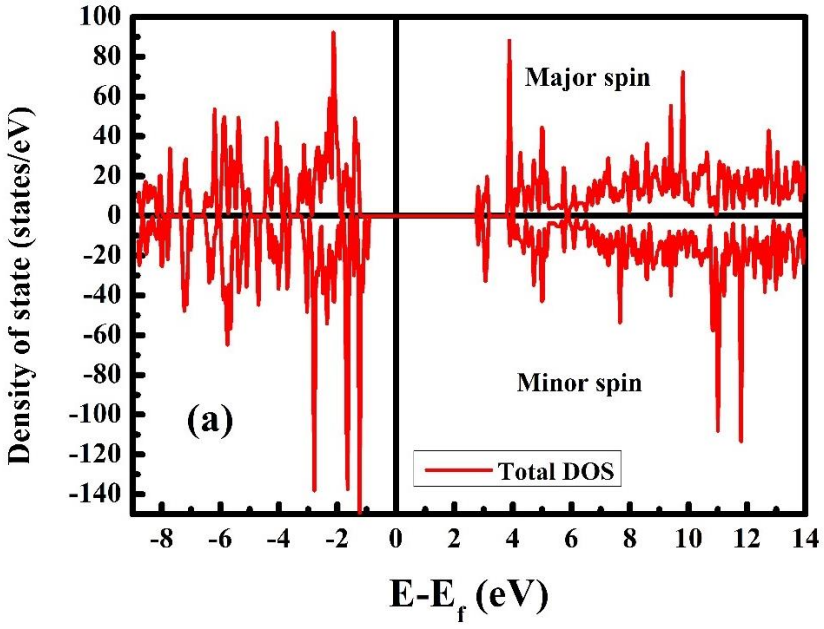

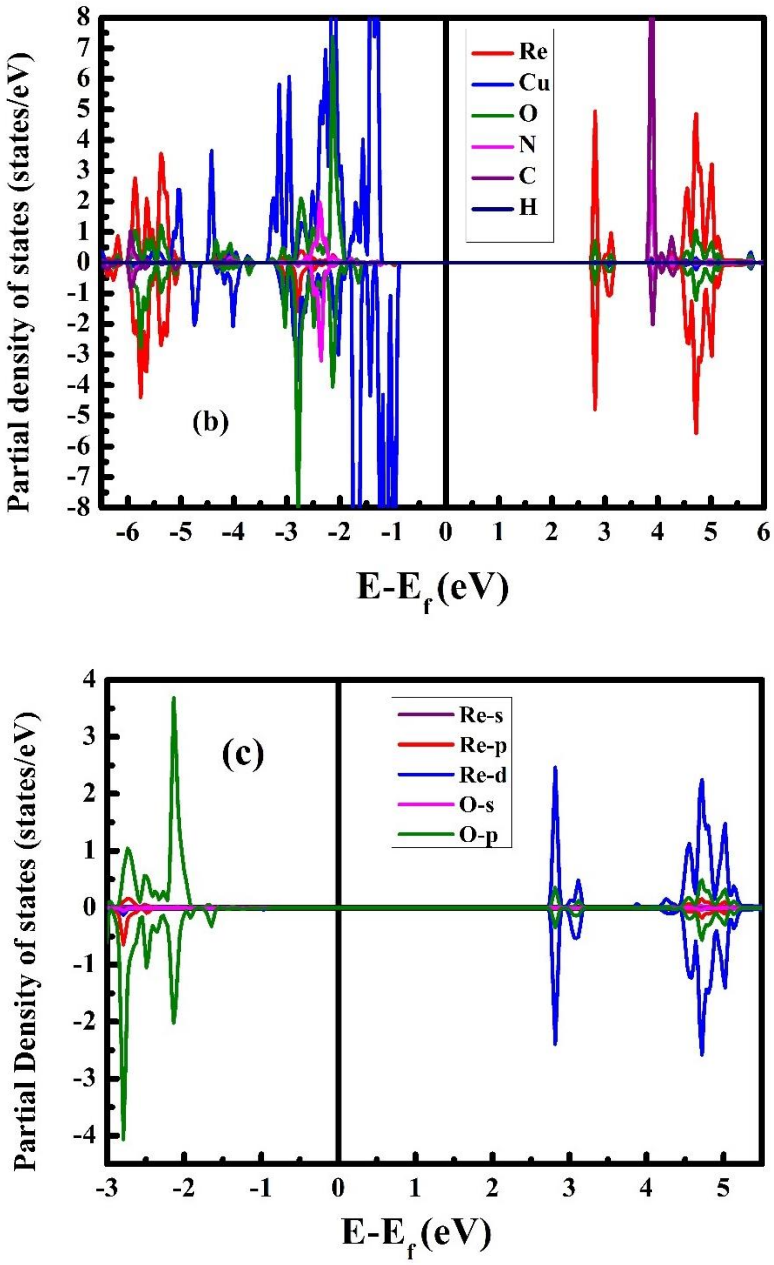

Figure V-2: Total (a) and Partial DOS (b,c) of $Cu(L\text{-}Arg)_2(ReO_4)_2$ using GGA-PBE Approximation.

The band structure is an important result used to further understand the electronic properties of materials. It allows exploring the evolution of the absorption spectrum, the charge density distribution, the electrons/holes mobility, and other characteristics. The calculated energy band dispersion in k-space of the $Cu(L\text{-}arg)_2(ReO_4)_2$ complex using GGA approximation is plotted in Figure V.3(a,b). From the band structure, the band gap which refers to the energy difference between the top valence band and the bottom of the conduction band. The high antisymmetric directions of the Brillouin zone are clearly described in Figure V.3(a,b). The minimum of the conduction band is located at Γ point, and the maximum valence band is

located at Z and M point respectively, for both major and minor spin. Here the minimum of the conduction band and the maximum valence band do not have the same k coordinates in Brillouin zone. This result underlines that the energy gap is induced by an indirect type transition for $Cu(L\text{-}arg)_2(ReO_4)_2$ complex.

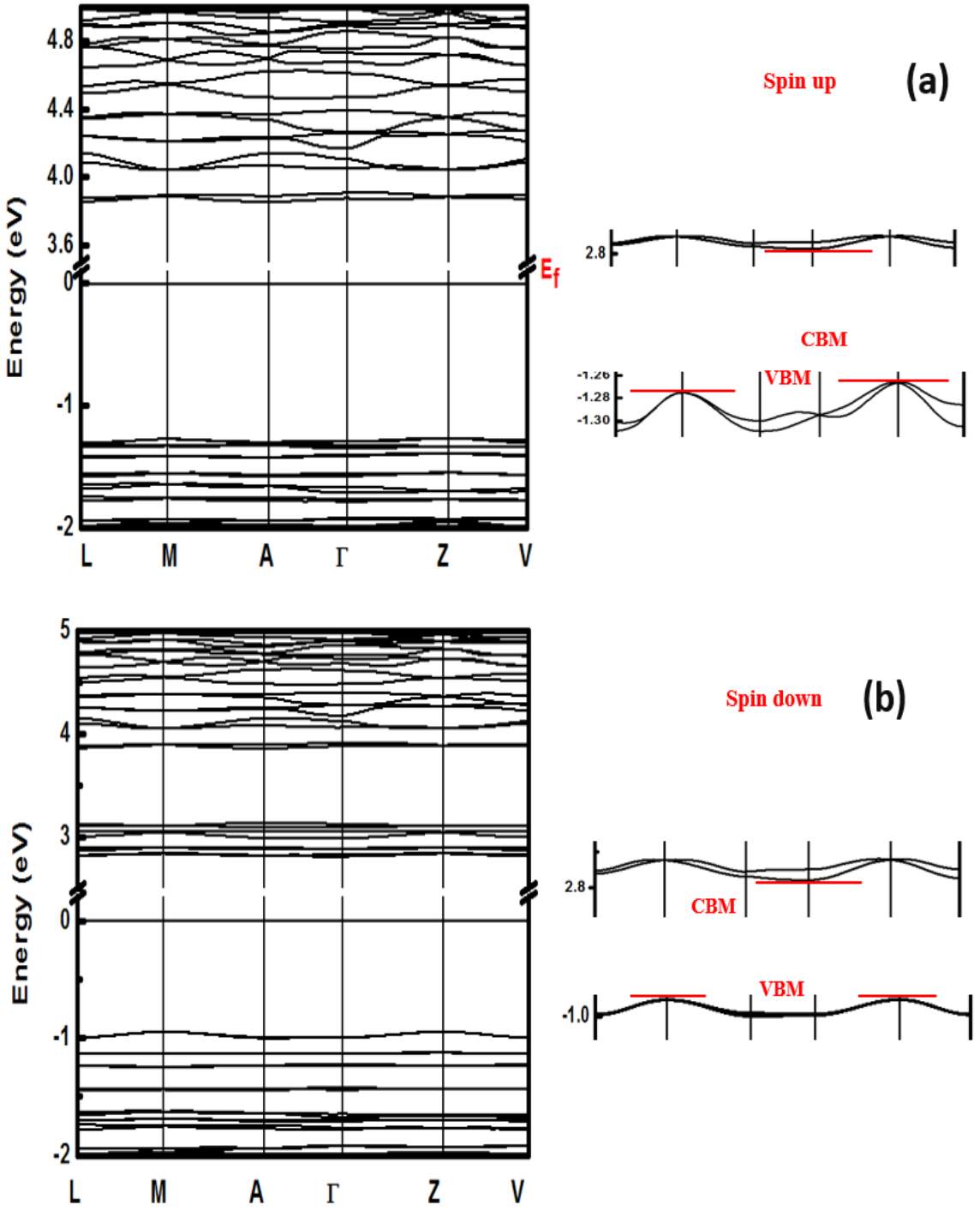

Figure V-3: The calculated band structures of $Cu(L\text{-}arg)_2(ReO_4)_2$ for spin up (a) and spin down (b) using GGA-PBE approximation.

V.4.1 Optical properties

The dielectric function and the absorption coefficient are calculated using GGA-PBE approximation, The real $\boldsymbol{\varepsilon_1}$ **(ω)** and imaginary part $\boldsymbol{\varepsilon_2}$ **(ω)** of dielectric function describe the dispersion of the incident photons and the absorption capacity of the phonon by the compound, respectively [245]. The complex dielectric function is expressed by the following equation [246]**:**

$$\varepsilon(\omega) = \varepsilon_1(\omega) + i\varepsilon_2(\omega) \qquad \textbf{(1)}$$

Figure V.4, illustrates the spectral behavior of the real part of the dielectric function from 0 to -14 eV spectral range. The static real part **ε** (0) begins from 2.5 at zero energy and increases to a maximum value of 4.41 and 4.05 for xx and zz directions respectively. Then, it decreases further until to cross a zero line at 12.7 eV. For directions xx and zz, we observe a change in the curve's shapes. That reveals that the material's response changes depend on chosen direction. The difference between xx and zz curves shape can be explained by the material's optical anisotropy. At an energy of 12.7 eV, the real part is negative, meaning that in this region no wave is propagated through the material.

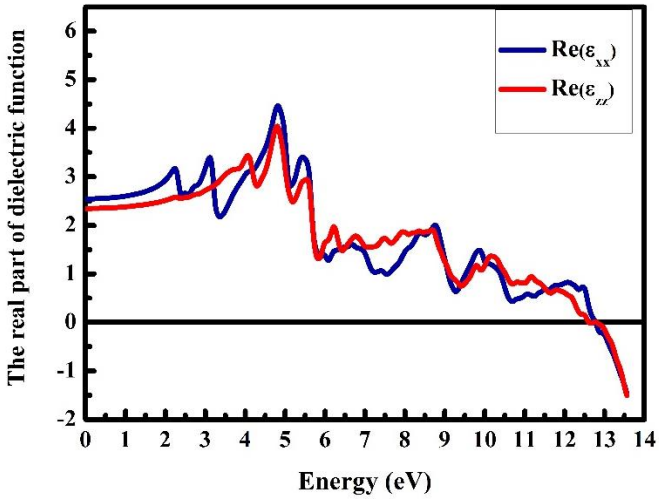

Figure V-4: Real part of dielectric function for $Cu(L\text{-}arg)_2(ReO_4)_2$ versus photon energy.

The optical absorption coefficient calculated using GGA-PBE approximation can be deduced from $\varepsilon_1(\omega)$, and $\varepsilon_2(\omega)$ using the following equation [247]:

$$\varepsilon(\omega) = \sqrt{2}(\omega)\left[\sqrt{\varepsilon_1(\omega)^2 + \varepsilon_2(\omega)^2} - \varepsilon_1(\omega)\right]^{1/2} \qquad \textbf{(2)}$$

The Figure V.5 shows, on the 0-14 eV spectral range, the calculated absorption coefficient versus phonon energy using GGA-PBE approximation. The absorption threshold values for $Cu(L\text{-}arg)_2(ReO_4)_2$ occur at around 2 eV and 3.2 eV for xx and zz direction, respectively. The calculated absorption coefficient starts to rise from the threshold energy. In the range of [2-4 eV], the absorption coefficient reaches a maximum at 3.23 eV for xx direction, whereas for the zz direction, the absorption starts from 3.2 eV and reaches a maximum at 4.2 eV. After 5 eV, the absorption coefficient increases efficiently due to a good absorption taking place in the U-V range. From the previous results, it is interesting to note that $Cu(L\text{-}arg)_2(ReO_4)_2$ could be promising for optoelectronic applications requiring a wide bandgap.

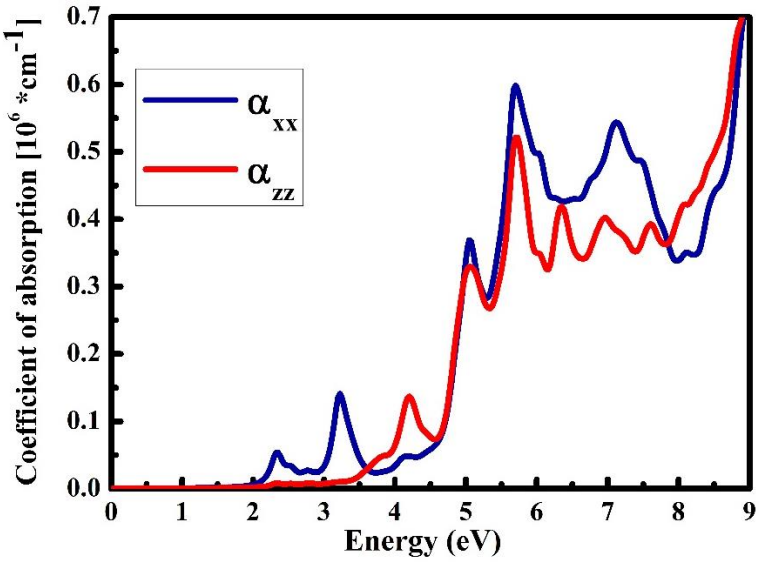

Figure V-5: The calculated absorption coefficient of $Cu(L\text{-}arg)_2(ReO_4)_2$ versus photon energy.

The experimental reflectance spectrum of (Cu^{II}/Re^{VII})-heterobimetallic L-Arginine complex is presented in Figure V.6. It is observed that the spectrum decreases linearly and reaches a minimum of 15% at 2.02 eV. Then, the curve increases gradually as a function of energy reaching a maximum of 55% in the vicinity of 3.09 eV. Furthermore, the Figure V.7. illustrates the calculated reflectivity of $Cu(L\text{-}arg)_2(ReO_4)_2$. The calculations carried out between 0 and 9 eV, confirm an optical anisotropy of the studied compound. When the energy is equal to zero, the reflectivity is around 4% and 5% for xx and zz direction, respectively. The first peak for $Cu(L\text{-}arg)_2(ReO_4)_2$ are situated at 2.1 eV for xx direction, while for the zz direction, it appears at 4.0 eV. The maximum of the reflectivity is observed at 5 eV and around 5.8 eV for xx and zz directions, respectively.

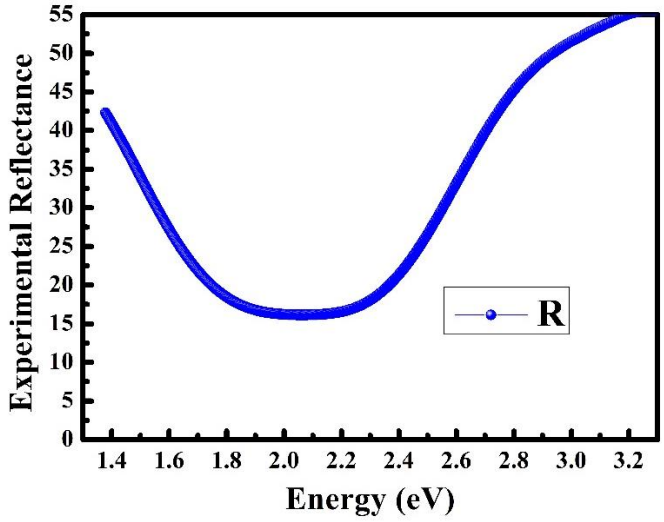

Figure V-6: The experimental reflectance spectrum of (Cu^{II}/Re^{VII})-heterobimetallic L-Arginine complex versus photon energy.

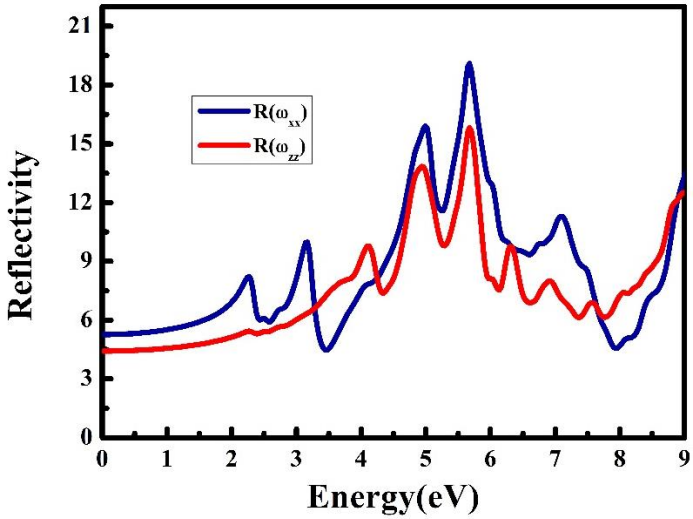

Figure V-7: Variation of reflectivity spectra as a function of energy (eV) of (Cu^{II}/Re^{VII})-heterobimetallic L-Arginine complex.

The Kubelka-Munk function K/S presented in Figure V.8 is estimated from the measured reflectance according to the following equation [248,249]:

$$F(R) = \frac{(1-R)^2}{2R} = \frac{K}{S} \qquad \textbf{(3)}$$

The R, K, and S are the reflectance, the absorption coefficient, and the scattering coefficient, respectively.

Figure V.8. shows the interaction between the incoming light and $Cu(L\text{-}arg)_2(ReO_4)_2$ material in the visible range as described by the Kubelka-Munk function. The F(R) function is

proportional to the absorption coefficient. This function starts increasing when the energy is 1.5 eV to reach a maximum at 2.05 eV, due to the photon absorption, and decreases smoothly with the energy increase.

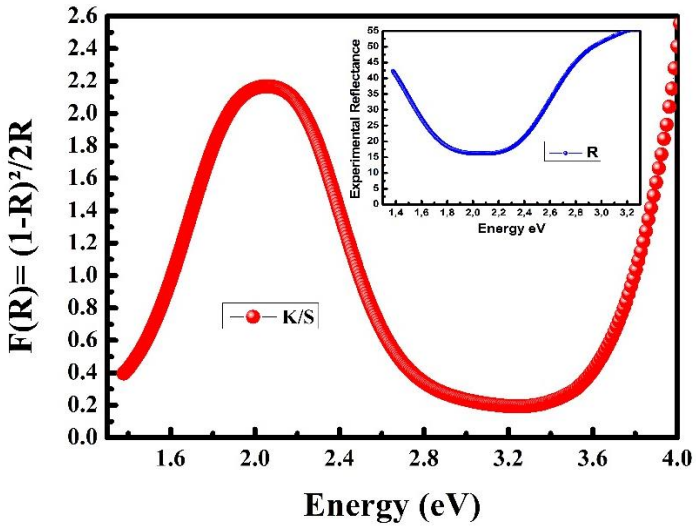

Figure V-8: The Kubelka-Munk function F(R) = K/S versus energy.

The Kubelka-Munk method based on reflectance spectra is used to estimate the experimental bandgap via the relationship (4). This method was proposed by Mott, Davis, and Tauc [248, 250–252]:

$$F\left(R_{\alpha}\right)h\nu = A(h\nu - Eg)^{n} \qquad \textbf{(4)}$$

Where $h\nu$ is the energy of incident photon, Eg is the optical gap energy situated between the localized states near the mobility edges according to the density of states model proposed by Mott and Davis [253, 254]. The constant A is known as band tailing parameter which is independent of photon energy. The exponent n is the power factor of transition mode. It can be equal to ½ or 2 depending on the transition type (indirect or direct transition).

The theoretical optical band gap is calculated from the absorption coefficient via Tauc plot equation [255]:

$$\left(\alpha h\nu\right)^{1/n} = A(h\nu - E_{g}) \qquad \textbf{(5)}$$

Where n=1/2 for a direct transition, and n=2 for an indirect transition.

For the $Cu(L\text{-}arg)_2(ReO_4)_2$, the experimental band gap calculated from the Kubelka-Munk equation is 3.62 eV, which is in a good agreement with the theoretical band gap around 3.60 eV as seen in Figure V.9 (a,b).

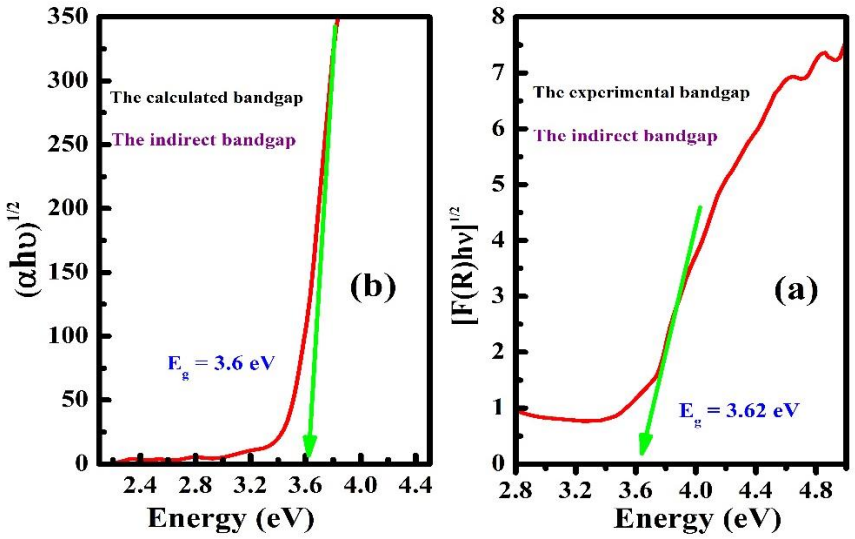

Figure V-9: The experimental (a) and the theoretical (b) band gap calculated using Tauc equation for the indirect transition versus energy.

In this work, we found that the experimental band gap (a) is very close to the calculated band gap (b) using GGA-PBE approximation. For this reason, we used the semi-empirical Kubelka-Munk function to calculate the scattering coefficient, from the experimental F(R) plotted in Figure V.10, and the theoretical absorption coefficient obtained using GGA-PBE approximation. From the calculated scattering coefficient for both directions xx and zz shown in Figure V.10, the scattering coefficient rises after 2.20 eV, and 2.7 eV for xx and zz directions, respectively. We can observe that for the xx direction, the maximum scattering coefficient is $7.23x10^5$ cm^{-1} which is reached at 3.23 eV while for the zz direction the maximum is around $0.75x10^5$ cm^{-1}, which takes place at 3.58 eV. It can be concluded that the light interaction with the studied compound is more important in the xx direction than the zz direction.

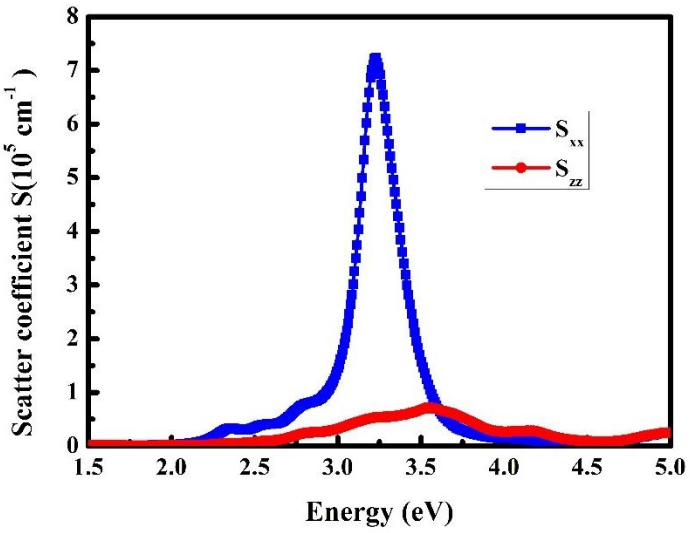

Figure V-10: The scattering coefficient S versus energy.

V.5 Conclusion

In this paper, the electronic, optical, and dielectric properties of $Cu(L\text{-}arg)_2(ReO_4)_2$, are investigated using the density functional theory (DFT), through the generalized gradient approximation (GGA-PBE). The density of states shows that the studied compound exhibits a magnetic behavior, due to the presence of Cu atoms. The band structure for major and minor spin confirms the indirect transition for the $Cu(L\text{-}arg)_2(ReO_4)_2$ complex. The experimental band gap estimated from the measured reflectance using the Tauc equation is in accordance with band gap calculated theoretically. Furthermore, based on the Kubelka-Munk semi-empirical approach, the transport scattering coefficient S is estimated for xx and zz directions respectively. The obtained results show the potential of this material to be a promising candidate for optoelectronic devices.

Chapter VI:
The structural, electronic, optical, magnetic, and thermoelectric properties of $NaMnAsO_4$ cluster.

VI.1 Introduction

Exploiting clean and safe sources of energy became a major technological challenge in the 21'st century [256–259]. Elaborating new materials with high efficiency, low cost, and improved durability, will impact on making promising energy technologies [260–263]. For that reason, new materials such as Transition Metal Oxide (TMO) compounds have received much attention from the scientific community. They can be tailored for a variety of applications [264–266]. Their introduction in the field of electronics dates to the 1996's. Tokito & al have reported the important role factor for hole injection at the metal-oxide interface when it is used as thin films for organic light-emitting diodes (OLED) [267]. TMO materials have been extensively used for various technical applications such as energy storage/ conversion systems, electrochemical capacitors, Li-ion batteries, metal oxides batteries, fuel cells which are coming more attractive than ever [268–272].

Furthermost of the phosphates and arsenates materials family is adopted by many oxides that have $AMXO_4$ ($A^IM^{II}X^VO_4$) type chemical formula, where A^I refers to alkali metal cation, NH_4^+, Tl^+, Ag^+, M^{II} refers to Fe, Cu, Zn, Mn, and X^V refers to As, P. The success of transition metal oxide materials can be explained by the presence of 3d TM ions, which create local ferromagnetic structures.

Among various metal oxides, the $NaMnAsO_4$ compound presents a new material that possesses an outstanding property that can be used for many optoelectronic devicesas is known for TM oxide materials. $NaMnAsO_4$ can crystallize in the monoclinic and orthorhombic structures. Recent results are an experimental explanatory synthesis of quasi-low-dimensional $NaMnAsO_4$, to study the structure, and magnetic properties [273,274]. Ulutagay-Kartin et al. have been reported that the monoclinic structure of $NaMnAsO_4$ (α-form) is obtained from a high-temperature synthesis in a molten salt medium, this structure has an antiferromagnetic transition at Neel temperature T_N= 50K, then a ferromagnetic transition emerged at low temperature, which shows a hard ferromagnetic hysteresis loop behavior. As well, the thermal magnetization measurement at the field of H= 500 Oe applied perpendicular to the (a) axis demonstrate a divergence behavior when the temperature approaches zero, confirming thus the emergence of a ferromagnetic phase transition along z direction.

A new form of $NaMnAsO_4$ has been reported by Matthias and Theo. In which they explored the structure properties obtained under hydrothermal conditions [274], the new form of $NaMnAsO_4$ crystallizes in orthorhombic structure (β-form), which is less dense (D = 3.95

$g.cm^{-3}$) as compared to the monoclinic structure (D = 4.03 $g.cm^{-3}$). With respect to the synthesis, structure and magnetic properties, the monoclinic structure is isostructural with $LiMnPO_4$, and $LiMnAsO_4$, then for the orthorhombic phase (β-$NaMnAsO_4$), a quantitative similarity in the structure has been found with isotypic sodium copper(II) arsenate $NaCuAsO_4$, whereas, the magnetic properties are reported for the first time.

In order to further improve the performance of these materials, a comprehensive understanding of the DFT calculations becomes necessary. Besides, no theoretical model has been processed for this compound and evaluated its electronic, optical, magnetic, and thermoelectrical properties. For this reason, the Density Functional Theory (DFT) calculations have been used widely to prove the stability of the structures and calculate the electronic, magnetic, thermoelectric, and optical properties [275,276]. The band structure, the density of states, and the charge density have been used to analyze the material's electronic structure. The dielectric constant, absorption coefficient, reflectivity and refraction index have been computed for the optical properties. Besides, BoltzTraP simulation is performed to calculate the transport properties of $NaMnAsO_4$ for both structures. This led to predict the material efficiency for the desired application, the results of the Seebeck coefficient, thermal conductivity, electrical conductivity and figure of merit have been discussed in detail. Then To overcome the bandgap underestimation lack of $NaMnAsO_4$ in standard DFT calculation. The correction of this lack is performed using the GGA+U approach. The reasonable potential value used for Mn atoms is U= 3.9 eV.

This work aims to provide a theoretical study of the electronic, optical, and thermoelectric properties based on the density functional theory using the GGA and GGA+U approach within the Wien2k package.

The plan of this work has been divided into four sections. In section 2, the structure electronic calculations are detailed. Section 3 concerns the obtained results for both structures of the $NaMnAsO_4$ compound, and Section 4 presents a conclusion of this work.

VI.2 Structure electronic calculations

In this work, we used density functional theory (DFT), within the full-potential linearized augmented plane waves (PF-LAPW) method, as implemented in the Wien2K package [156]. The exchange-correlation energy is described by the generalized gradient approximation (GGA) proposed by Perdew, Burke, and Ernzerhof [157]. The electronic, magnetic, and optical results of this compound were obtained from the GGA approach. Unfortunately, GGA cannot

successfully describe the d states of the transition metal atoms (Mn) present in the material. For that reason, the correction of this lack is necessary. The exchange-correlation terms were added to GGA using the GGA+U approach. The GGA+U yield quite satisfying results by exploiting the Coulomb repulsion (U). for Mn atoms, the reasonable value of the potential is U= 3.9 eV. The Kohn-Sham equation and energy function were evaluated consistently. The space was divided into the interstitial and the non-overlapping muffin-tin spheres centered on the atomic sites. The basis function inside each atomic sphere consisted of linear expansion of the radial solution of a spherically potential multiplied by spherical harmonics. In the interstitial region, the wave function was taken as an expansion of plane waves, and no shape approximation for the potential was introduced in this region which is consistent with the full potential method. The core electrons were described by atomic wave functions which can be solved relativistically using the current spherical part. The FP-LAPW calculations were performed using the crystal structure parameters deduced from our X-ray diffraction refinement. The spin-polarized potential is included in our calculations. The atomic muffin-tin (RMT) spheres, supposed not to overlap with each other, are taken as 1.98, 1.7, 2.11, and 1.4 a.u. for Mn, As, Na, and O atoms, respectively.

The material crystallizes in two structures which are: the monoclinic lattice (α-$NaMnAsO_4$) within space group $P2_1/c$, and the orthorhombic structure (β-$NaMnAsO_4$) within space group P_{nma} with (a≠ b≠ c) as seen in Figure VI.1. The gap energy, which defines the separation of the valence and core state, was chosen equal to -7.0 R_y. The largest reciprocal vector G in the charge Fourier expansion, G_{max} is equal to 12 and the cut-off energy corresponding to the product of the muffin-tin radius and the maximum reciprocal space vector, $R_{MT}.K_{max}$, was equal to 7. Inside the atomics spheres, the potential and charge density are expanded in crystal harmonics up to l_{max} = 6. Calculations are performed with 200 k-points. This value is large enough to ensure the magnetic moment. The convergence criterion for the energy was set at 10^{-4} eV. Furthermore, to calculate the thermo-electrical properties of this material for both structures, we used the theory of transport distribution function as implemented in BoltzTraP code, The calculated energy band structure was used in combination with the Boltzmann transport equation developed by Georg Madsen and David Singh [276]. This theory elucidates the thermoelectric characteristics such as electrical conductivity, thermal conductivity, Seebeck coefficient, and figure of merit through the following equations:

$$\sigma_{\alpha\beta}(\varepsilon) = \frac{1}{N}\sum \sigma_{\alpha\beta}(i,k)\frac{\delta(\varepsilon-\varepsilon_{i,k})}{\delta(\varepsilon)} \qquad \textbf{(1)}$$

$$\sigma_{\alpha\beta}(i,k) = e^2 \tau_{i,k} \upsilon_\alpha(i,\vec{k}) \upsilon_\beta(i,\vec{k}) \qquad (2)$$

Where $\tau = 10^{-14}$s is the relaxation time, it is kept constant in the BoltzTraP code. Moreover, Seebeck coefficient S, and electrical conductivity σ are in terms of temperature T and mobility μ.

$$\sigma_{\alpha\beta}(\alpha,\mu) = \frac{1}{\Omega}\int \sigma_{\alpha\beta}(\varepsilon)\left[-\frac{\partial f_0(T,\varepsilon,\mu)}{\partial\varepsilon}\right]d\varepsilon \qquad (3)$$

$$S_{\alpha\beta}(T,\mu) = \frac{1}{eT\Omega\sigma_{\alpha\beta}(T,\mu)}\int \sigma_{\alpha\beta}(\varepsilon)(\varepsilon-\mu)\left[-\frac{\partial f_0(T,\varepsilon,\mu)}{\partial\varepsilon}\right]d\varepsilon \qquad (4)$$

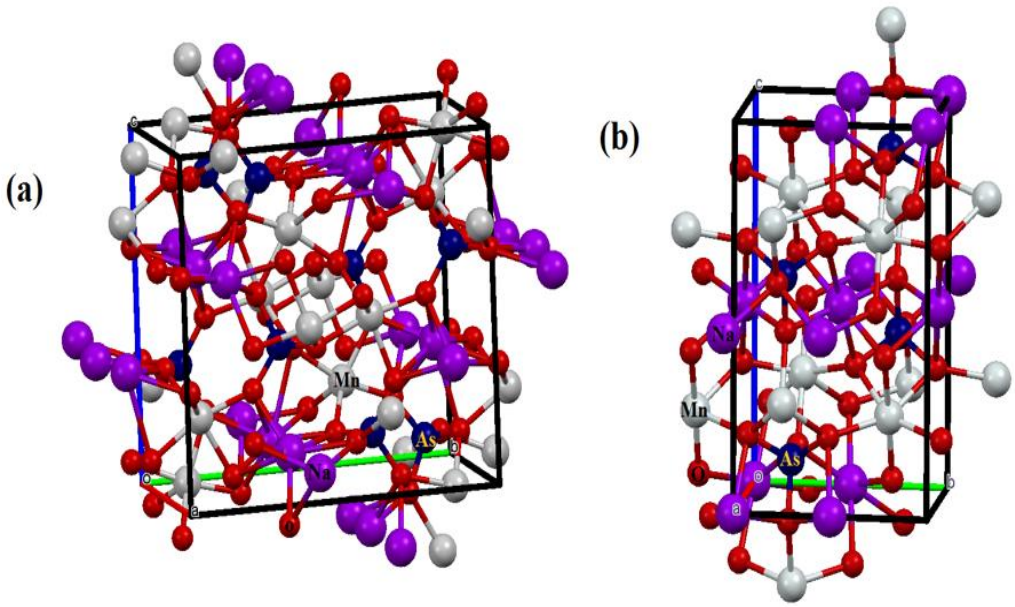

Figure VI-1: Crystal structures of (a) monoclinic and (b) orthorhombic $NaMnAsO_4$ material.

VI.3 Results and discussion

VI.3.1 Structural properties

The first part of this work consists of determining the optimized relaxed lattice parameters of both structures, monoclinic and orthorhombic of $NaMnAsO_4$ (with $a \neq b \neq c$). The optimization is attained by repeated sequential relaxing of the volume and the shape of the primitive unit cell. The first step equilibrium volume was determined by varying the unit cell volume using a third-order fitting polynomial with data of total energy value vs unit cell volume. Then optimizing the ratio c/a, b/a, and the volume to find the lattice parameters equilibrium as seen in Fig. VI-2.

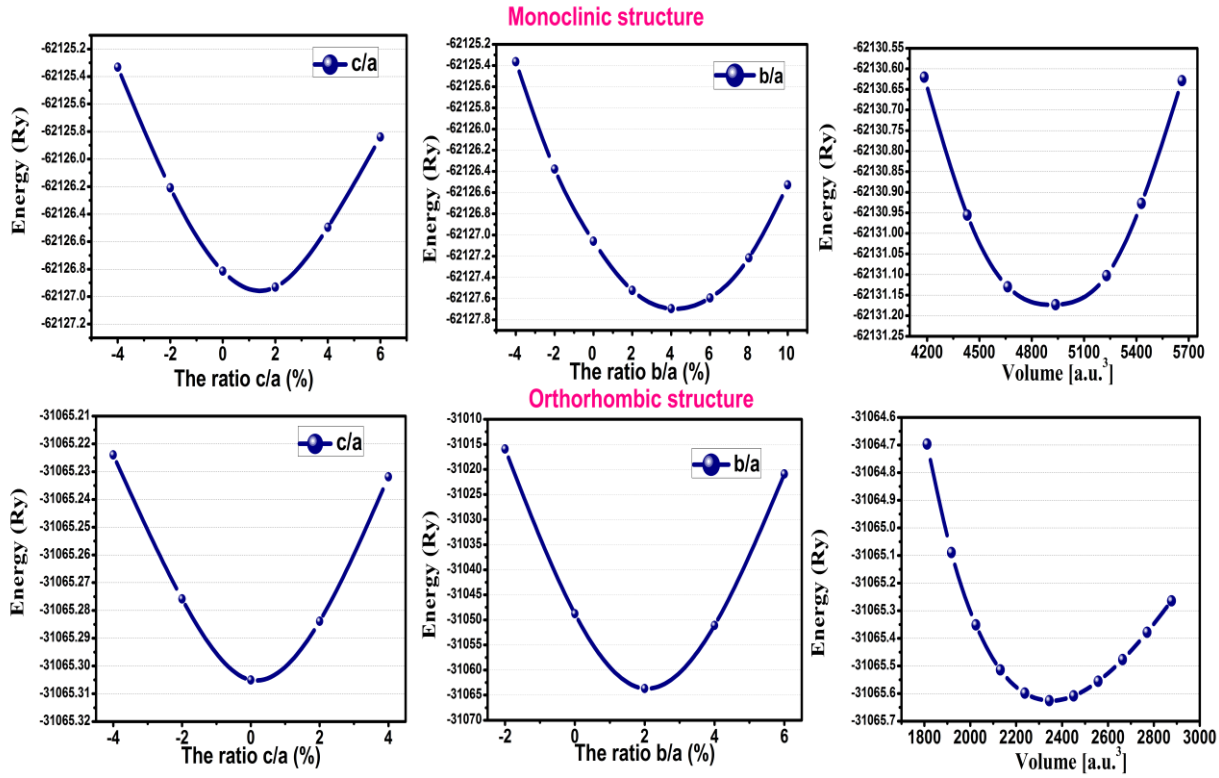

Figure VI-2: Total energy versus c/a, b/a and unit cell of NaMnAsO4 for both structures (α-form and β-form).

The thermodynamic stability is essential to realize if the material synthesis reaction is exothermic, to be used in device-based applications. The reaction type can be evaluated with the help of the enthalpy of formation (ΔH_f) calculation, through the following equation [277]:

$$\Delta H_f = E_{Total}(NaMnAsO_4) - E_{Na} - E_{Mn} - E_{As} - 4E_o \qquad (5)$$

Where $E_{Total}(NaMnAsO_4)$ represents the ground state energy of $NaMnAsO_4$, E_{Na}, E_{Mn}, E_{As}, and E_O are the individual energies of Na, Mn, As, and the Oxygen atoms, respectively. Table 1. (a) gathered the obtained results.

The thermodynamic stability of $NaMnAsO_4$ for both monoclinic and orthorhombic structures is proved with the negative value of ΔH_f (see Table VI-1). However, the monoclinic phase is comparatively more stable than the orthorhombic phase.

The calculated elemental analyses for the two phases have been obtained based on the molecular mass information of the studied compound and of their atoms, the values have been found to be: As (34.55%); Na (10.60%); Mn (25.33%) and O (29.51%). The calculated bond lengths between different atoms are presented in Table VI-2.

Table VI-1: The optimized parameters for both structures of $NaMnAsO_4$ cluster.

$NaMnAsO_4$ Compound		Lattice parameters(Å)			Total Energy (Ry)		ΔH_f (Ry)
		a	B	c	GGA	GGA+U	
Monoclinic phase (This work)		5.49	11.40	9.97	**-62131.861**	**-62128.964**	**-1.82**
Orthorhombic phase (This work)		10.38	6.09	4.93	-31065.625	-31066.154	-1.19
(Exp. /Other work)	**Monoclinic phase [274]**	6.09	11.40	10.50	- -		- -
	Orthorhombic phase [273]	10.85	6.38	5.15			

The calculated elemental analyses for the two phases are: As (34.55%); Na (10.60%); Mn (25.33%) and O (29.51%). The calculated bond lengths between different atoms are presented in Table VI-2.

Table VI-2: Bond length for each $NaMnAsO_4$ structures.

$NaMnAsO_4$ material	Bond length (Å)					
	Na-Mn	Na-As	Mn-As	O-Na	O-Mn	O-As
Monoclinic Phase	3.07	3.94	3.18	2.58	2.14	1.68
Orthorhombic Phase	3.92	3.06	3.05	2.42	2.28	1.73

VI.3.2 Total and partial densities of states (DOS and PDOS)

The electronic properties are important, to understand the nature of the connections made between the different elements (the atoms' contributions in the valence band (VB) and conduction band (CB)) on the electronic properties of the studied material, as well as assess the spectral distribution of absorption, mobility, and other features.

The density of state (DOS) and the band structure of the metal transition oxide $NaMnAsO_4$ were deduced from the spin-polarized calculation with the PBE-GGA and GGA+U approximations. The total DOS and P-DOS are reported in Figure VI.3, Figure VI.4., and Figure VI.5. for both the monoclinic and orthorhombic structures, respectively. The Fermi level is taken as a reference. The spin up and spin down are illustrated in the plotted total and partial DOS, as the positive and negative energies, respectively. It seems that the energy distribution appears to be almost the same for both structures. The total density of states display a

dissymmetry between major (↑) and minor (↓) spins electron, which confirms the magnetic behavior of $NaMnAsO_4$ for both structures. The total DOS looks even similar for both approximations (GGA and GGA+U). The bandgap energies changes for the monoclinic and the orthorhombic structures, it decreases from 1.35 eV to 1.26 eV and shows an interesting enhancement from 0.83 eV to an optimal value of 1.59 eV by applying U potential for monoclinic and orthorhombic structures, respectively.

According to Figure VI.3(a,b) and Figure VI.4. the valence band of the monoclinic structure of $NaMnAsO_4$ can be divided into two regions: The upper part of the valence band [-6.01, -2.45 eV], is mainly formed by states attributed to the Mn-3d and O-2p states, giving rise to p-d coupling with a small contribution of the As-3d and Na-2p states. The lower part of the valence band is located between -2.17 eV and -0.13 eV, is formed mainly by spin up states attributed to Mn-3d and O-2 p states with a small appearance of states of Na-2p and As-3d.

The last region is the conduction band. The first range [0.91 eV, 4.42 eV], dominated mainly by spin down of the Mn-3d state, with a small hybridization with the O-p, As-3d, and Na-2p states. The second range between 4.48 eV and 12.80 eV, is entirely composed of 2p, 2p, and 3d states of Oxygen, Sodium, and As, respectively.

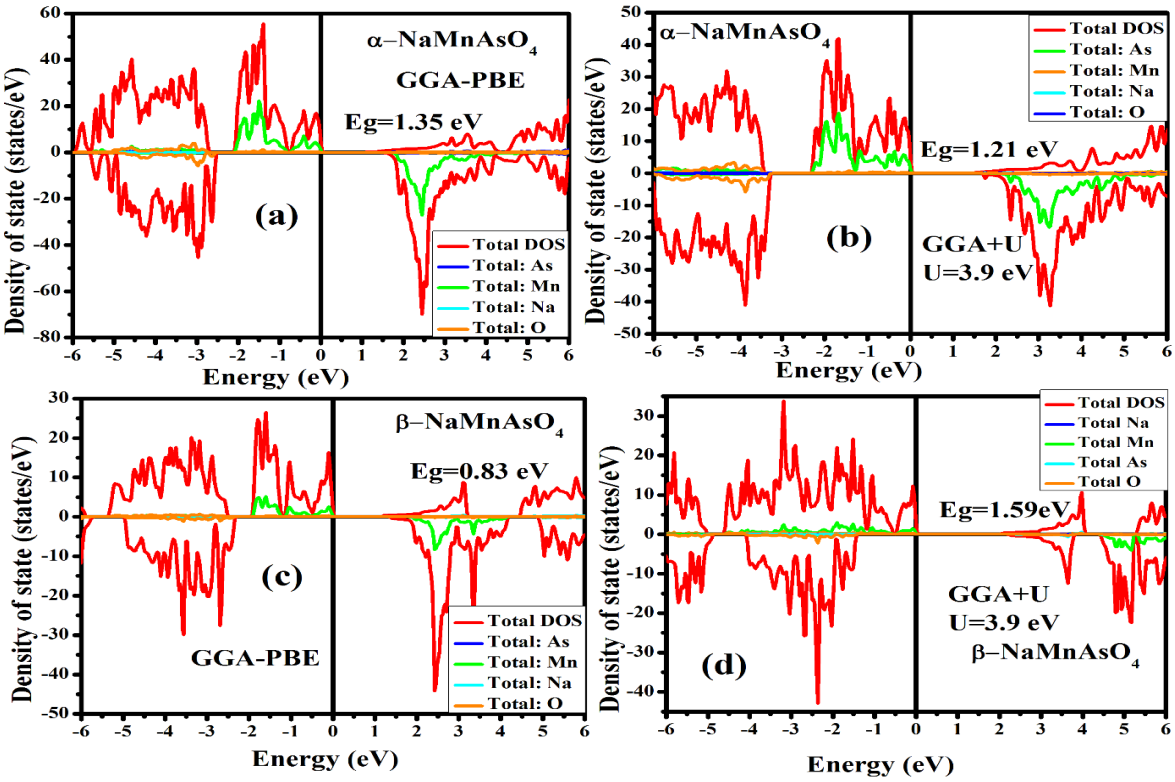

Figure VI-3: The total Density of states of $NaMnAsO_4$ monoclinic (a,b) and orthorhombic (c,d) structures.

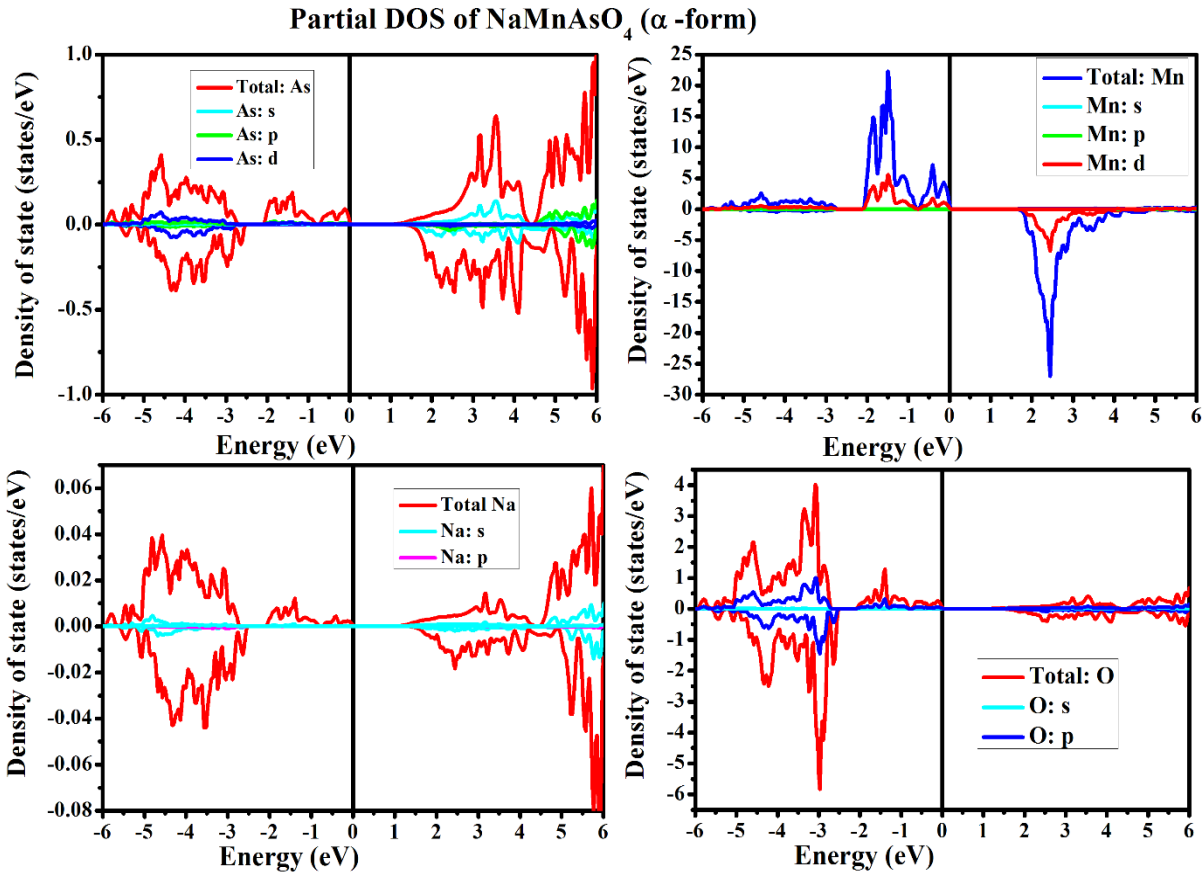

Figure VI-4: Partial DOS of the monoclinic structure of $NaMnAsO_4$ cluster.

The density of states (DOS) and the partial density of states (PDOS) of the Orthorhombic $NaMnAsO_4$ compound are shown in Figure VI.3(c,d) and Figure VI.5. It reveals that the first valence region is located between -5.47 eV and -2.28 eV, is composed entirely of 2p states of Oxygen, the second region [-1.96 eV, -0.02 eV] was formed by a spin up of the state Mn-3d. The conduction band in the first region [0.96 eV to 4.20 eV], is mainly dominated by the spin down of the "d" states of Mn and a small amount of O "p" states. The last region [4.40 eV to 13.04 eV] is formed by a small contribution of O-p, Na-2p, As-3d, and Mn-3d states.

We note that there is no symmetry between the spin-up and down configuration of the state density of both structures of the $NaMnAsO_4$ compound. This indicates that the magnetic behavior of the monoclinic and orthorhombic of the $NaMnAsO_4$ compound, is due mostly to the contribution of the Mn element.

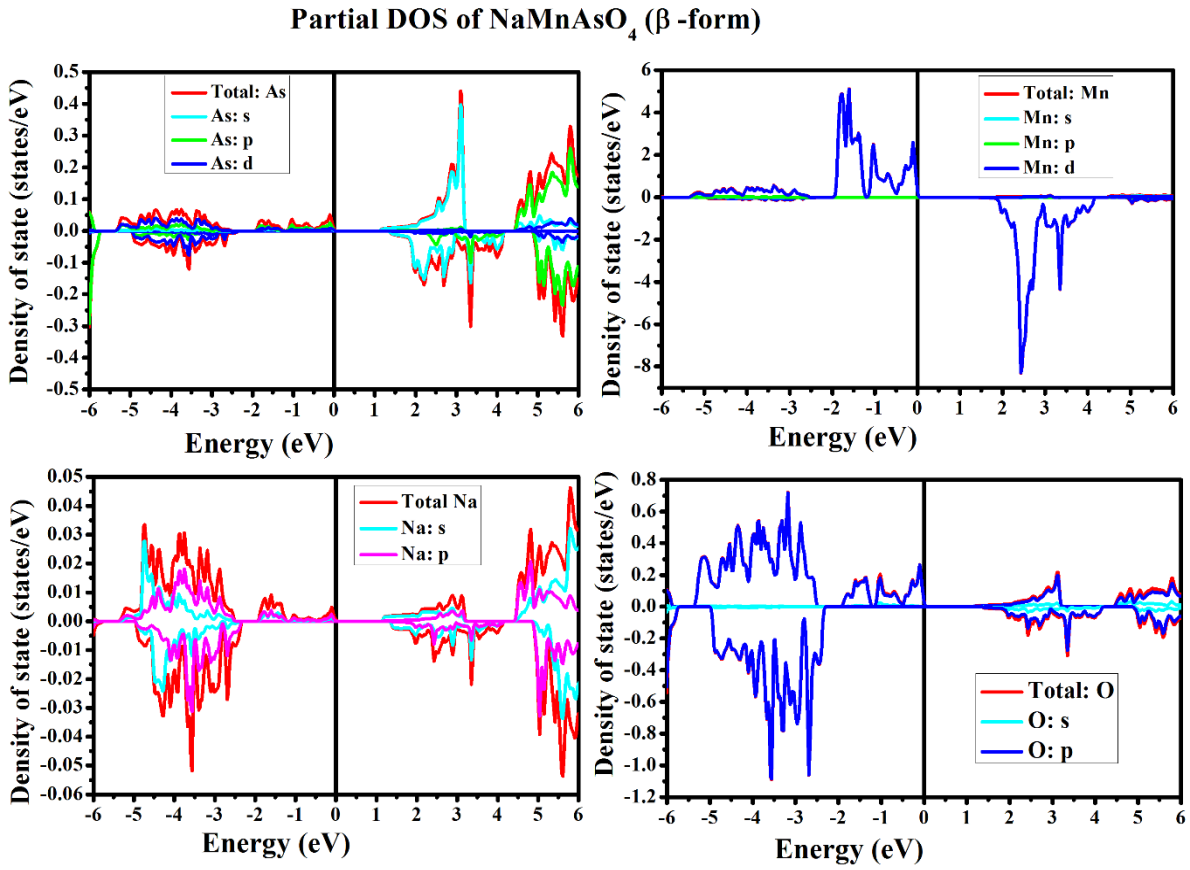

Figure VI-5: The partial DOS of the orthorhombic structure of $NaMnAsO_4$ cluster.

The magnetic behavior of $NaMnAsO_4$ is confirmed by the total and partial density of states. The moments are calculated using PBE-GGA and GGA+U approximations, as seen in the Table VI.3. The calculations of the total and partial magnetic moments of both monoclinic and orthorhombic structures of $NaMnAsO_4$ compound are performed, for the Na, Mn, As, and O atoms in the muffin-tin spheres and in the interstitial sites. The results of these calculations are shown in Table VI.3. As seen the monoclinic structure is more magnetic than the orthorhombic structure, resulting in a total magnetic moment of 40 μ_b (Bohr magnetons) using GGA-PBE and GGA+U approaches. The partial DOS shows that the magnetic behavior comes from the d orbital of the Mn atom. The calculated effective magnetic moment of high-spin d^5 state of Mn^{2+} ions are 3.80 μ_b and 4.25 μ_b with GGA-PBE and GGA+U approaches, respectively, then the experimental effective magnetic moment at the high temperature is 5.44 μ_b as reported in the reference [274], for the monoclinic phase. The difference is probably due to the material's spin ordering, besides the temperature effect, taking into account that DFT is formulated for zero Kelvin. Whereas no experimental calculation has been processed to evaluate the magnetic properties of the orthorhombic structure. The difference of the total moment between the two structures is explained by the intensity of the d-Mn atom, as seen in

Figure VI.3 and Figure VI.4 the intensity of d-Mn orbital of the monoclinic structure is more important as compared to the orthorhombic structure. Besides the distance between the magnetic atoms in the bulk.

Table VI-3: Magnetic moments calculated for the Na, Mn, As and O atoms in the Monoclinic and Orthorhombic phase using GGA and GGA+U approximations.

	Monoclinic (μ_b)		Orthorhombic (μ_b)	
Site	**GGA-PBE approximation**	**GGA+U approximation**	**GGA-PBE approximation**	**GGA+U approximation**
M^T	40.00267	40.01823	19.99274	19.99864
M^{Na}	0.0048	0.00262	0.00094	0.00063
M^{Mn}	**3.80164**	**4.25255**	**4.28513**	**4.40708**
M^{As}	0.01976	0.01270	0.02167	0.01638
M^O	0.3514	0.06479	0.5858	0.03790

VI.3.3 Band structures

The spin-polarized band structure calculations of the $NaMnAsO_4$ compound (monoclinic and orthorhombic structures) were carried out according to the directions of high symmetry along with R- Γ- X- M- Γ points in the first Brillouin zone, using the lattice parameter calculated in the previous section. The spin-polarized band structures are illustrated in Figure VI.6(a-d). for the $NaMnAsO_4$ compound in the monoclinic and orthorhombic structures using GGA and GGA+U approximations, to the complete understanding of the studied material for optoelectronic applications. As seen in the Figure this material exhibits a semiconductor character for both spin-up and spin-down.

From Figure. VI.6 (c,d), we note that the orthorhombic structure of the $NaMnAsO_4$ compound has a direct bandgap in the direction Γ → Γ of the Brillouin zone (majority spin) with both approximations (GGA-PBE and GGA+U), in which the maximum of the valence band and the minimum of the conduction band are located at the Γ point. On the other hand, the monoclinic structure of $NaMnAsO_4$ Fig. VI.6(a,b), has an indirect bandgap in the direction of M → Γ (majority spin) of the Brillouin zone. The maximum of the valence band and the minimum of the conduction band are located at the M and Γ point using GGA-PBE and GGA+U approaches, respectively. The direct bandgap is also observed in the direction of Γ → Γ for a

spin-down for both monoclinic and orthorhombic structures. Besides, Table VI.4 contains the different energy bandgaps of the studied material as calculated by the GGA-PBE and GGA+U approximations. The direct bandgap in the visible region at the orthorhombic structure of $NaMnAsO_4$ make this structure more suitable for optoelectronic devices.

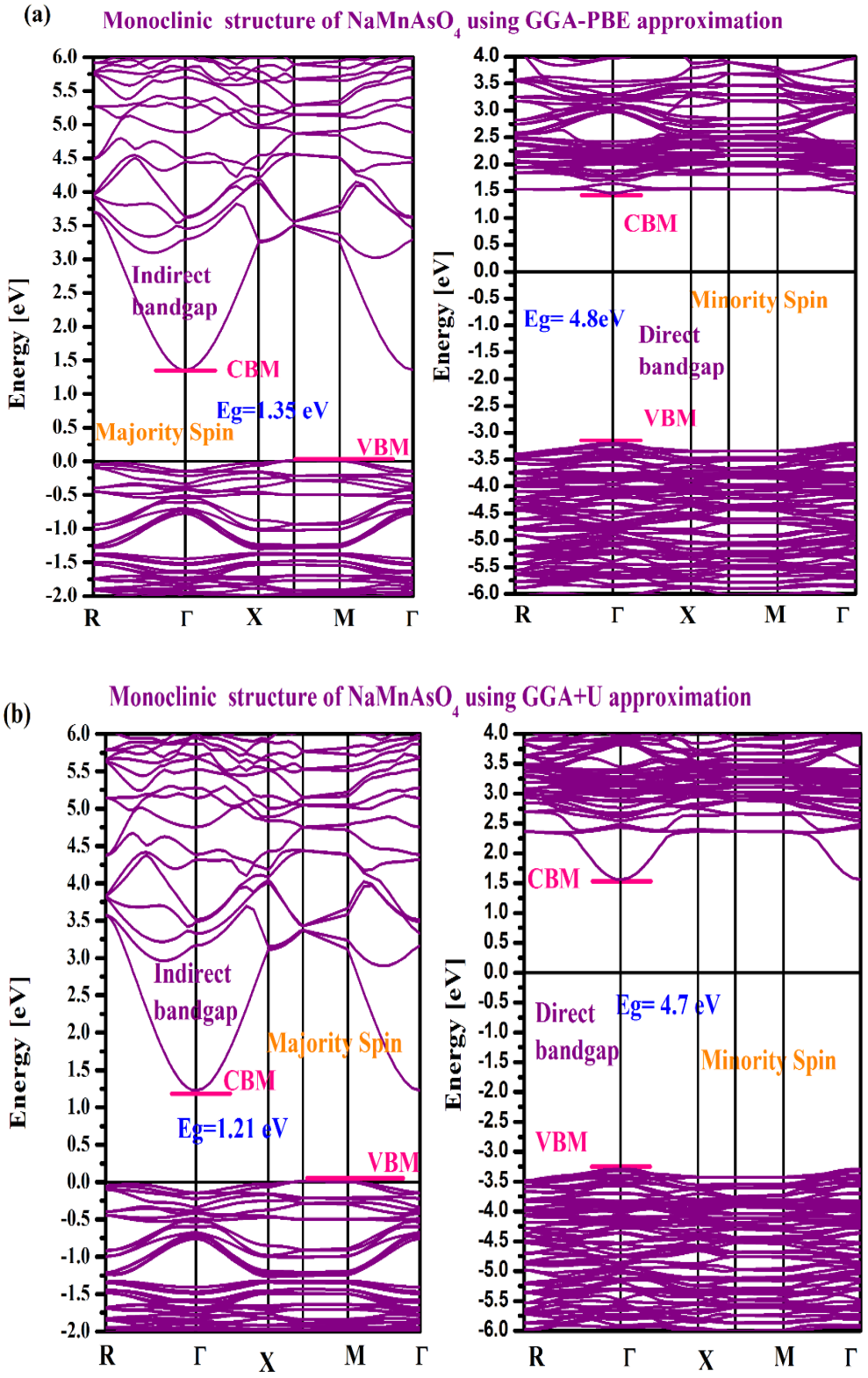

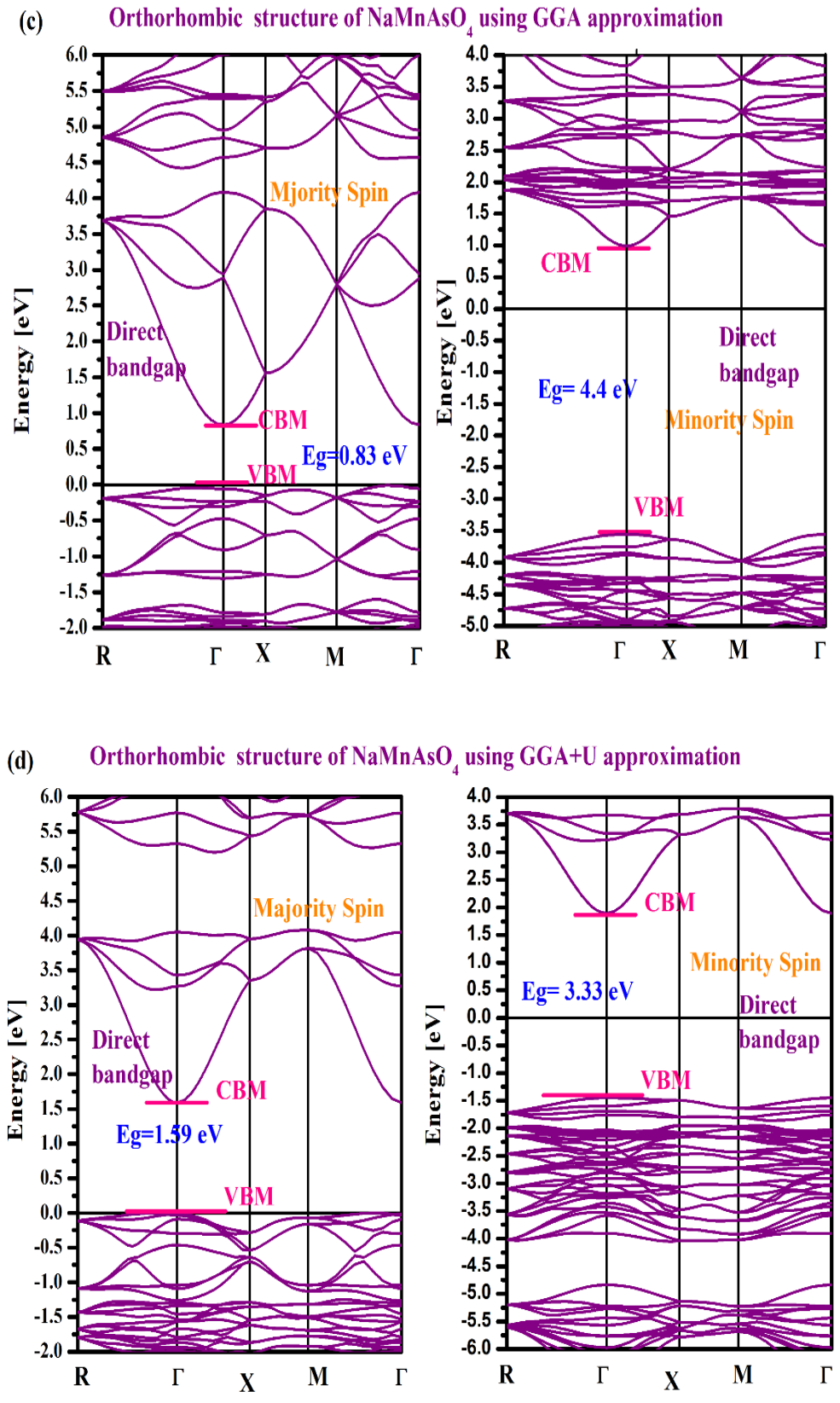

Figure VI-6: The band structure (up + down) for (a,b) monoclinic and (c,d) orthorhombic structures of $NaMnAsO_4$ using GGA and GGA+U approaches.

Table VI-4: Calculated band gaps of the $NaMnAsO_4$ with GGA method.

NaMnAsO4 Compound		E_g (eV)	
		Spin-up	**Spin-down**
GGA-PBE approximation	**Monoclinic phase**	1.35 (M- Γ)	4.8 (Γ− Γ)
	Orthorhombic phase	0.83 (Γ− Γ)	4.4 (Γ− Γ)
GGA+U approximation	**Monoclinic phase**	1.21 (M- Γ)	4.7 (Γ− Γ)
	Orthorhombic phase	1.59 (Γ− Γ)	3.33 (Γ− Γ)

VI.3.4 Electronic charge density

The charge density presents another mean that can be used to analyze the nature of the bonds in the monoclinic and orthorhombic $NasMnAsO_4$ compound. The calculations were performed and illustrated along with the (110) plan as seen in Figure VI.7.

From the charge distribution, we can observe that for the orthorhombic and monoclinic structures of $NaMnAsO_4$ material: Na-Mn, Na-As, and Mn-As bonds contact revealed to be covalently linked, due to the distribution of the charge density between Na and Mn, Na and As, and Mn and As. That appears homogeneous with almost the same affinities of electron charge density. While the contours around the Na-O, and Mn-O contact are shaded to indicate the existence of an ionic bond. Indeed, the contours of As, Na, and Mn atoms process that the circles around the nuclei atoms are focused in valence electrons as compared to Oxygen atoms whose core electrons accumulate near the nucleus. In addition, the electronegativity charge can be an important parameter that could be responsible for the charge transfer from Na, As, Mn, and O atoms. The oxygen is the most electronegative O (= 3,44) than Na (=0,93), Mn (=1,55), and As (=2,18) by the Pauling scale. Due to this difference in the electronegativity, the charge between them gives rise to an ionic bond.

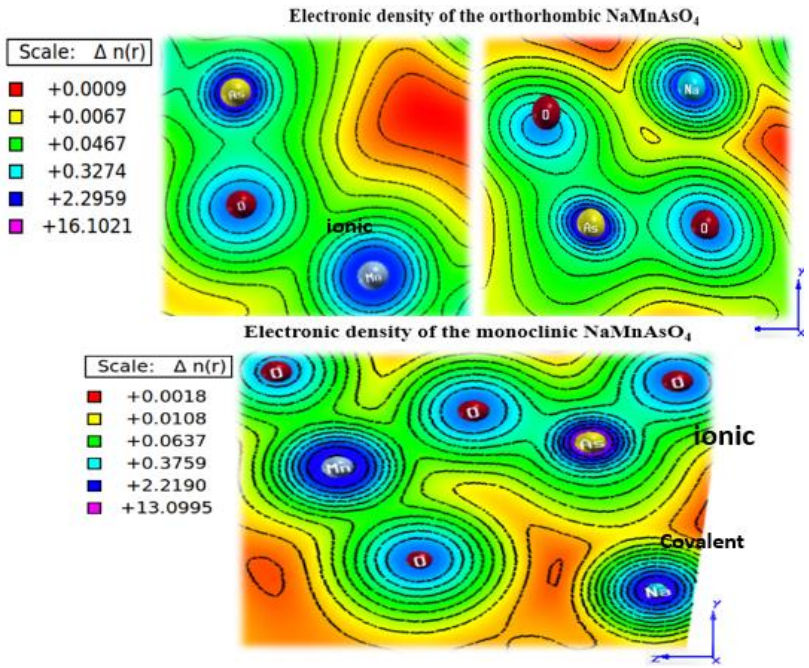

Figure VI-7: Charge density of the monoclinic and orthorhombic structure $NaMnAsO_4$ in plan (110).

VI.3.5 Optical properties

The optical properties of the materials can be described by the complex dielectric function, which presents the linear response of a system due to an external electromagnetic field, it is written as [211,226, 246, 278]**:**

$$\varepsilon(\omega) = \varepsilon_1(\omega) + i\varepsilon_2(\omega) \qquad \textbf{(6)}$$

$\boldsymbol{\varepsilon_1}$ (ω) and $\boldsymbol{\varepsilon_2}$ (ω) are the real and imaginary parts of the dielectric function respectively. The $\boldsymbol{\varepsilon_2}$ (ω) reflects the absorption of the material and is directly related to the electronic band structure of the material, while the real part $\boldsymbol{\varepsilon_1}$ (ω) is related to the polarization of the medium. It derives from the imaginary part using the Kramers-Kronig relations [279] :

$$\varepsilon_1(\omega) = 1 + \frac{2}{\pi}\int_0^{\infty} \frac{\varepsilon_2(\omega')\omega' d\omega'}{\omega'^2 - \omega^2} \qquad \textbf{(7)}$$

$$\mathrm{Im}\,\varepsilon(\omega) = \varepsilon_2(\omega) = \frac{4\pi^2 e^2}{m^2\omega^2}\sum_{i,j} \left| < i \left| M \right| j > \right|^2 * (f_i(1-f_i))\delta(E_f - E_i - \hbar\omega) d^3k \qquad \textbf{(8)}$$

M is the dipole matrix, e and m are the charge and mass of the electron, respectively; ω is the frequency of the incident photon. , f_i is the Fermi distribution function for the i^{th} state;

$|i>$ is the wave function corresponding to the eigenvalue E_i , the energy of the electron in the i^{th} state, *i* and *j* are initial and final states respectively.

The knowledge of these two quantities leads to the calculation of the absorption coefficient **α**, *k* the extinction coefficient, refractive index n, and reflectivity R given by the following relationships [280,281]:

$$\alpha(\omega) = \frac{2\pi\omega}{C}\frac{\sqrt{-\mathrm{Re}(\omega)+|\varepsilon|}}{2} \quad \textbf{(9)}$$

$$n(\omega) = \left[\frac{\sqrt{\varepsilon_1^2+\varepsilon_2^2}+\varepsilon_1}{2}\right]^{1/2} \quad \textbf{(10)}$$

$$R(\omega) = \frac{(n-1)^2+k^2}{(n+1)^2+k^2} \quad \textbf{(11)}$$

The interaction between incident photons and a semiconductor globally results in an essential characteristic of the material. The absorption coefficient is calculated by the GGA-PBE and GGA+U (U=3.9 eV) methods, and are illustrated in the range of the wavelength [200-800] nm in Figure VI.8. We can see that the spectra show an anisotropic nature between the ordinary components ($abs^{//}$) and extraordinary components($abs^{\perp}$), this optical anisotropy is an immediate consequence of the structural anisotropy of the $NaMnAsO_4$ compound (unsymmetrical material). We generally note that the spectrum of the absorption coefficient according to direction zz is more intense than those according to direction xx for both the monoclinic and the orthorhombic structures of the $NaMnAsO_4$.

It is obvious from the plot of the absorption coefficient that good absorption is associated with the GGA approach calculations except for the orthorhombic structure in the range of [275-350] nm. The fact of applying U potential on Mn atoms for the monoclinic $NaMnAsO_4$ induced a small decrease of the bandgap energy, as well as decreased the material's absorption to the incident light in the visible range. But for the orthorhombic structure, a small enhancement of the bandgap has been observed, as well as, a good absorption in the short wavelengths.

From the obtained result, it is clear that the spectra of the absorption coefficient appear high and increase gradually in the short wavelengths. In this case, the majority of incident photons (and transmitted into the material) are absorbed. Near 400 nm, it is worth noting the spectrum of the orthorhombic structure of $NaMnAsO_4$ is very intense compared to the

monoclinic structure, and still possesses this behavior, as well as, the spectra decrease gradually with the wavelength. The maximum absorption is shown in the Ultraviolet region which confirms the studied material potential as a candidate for the application in optoelectronic devices.

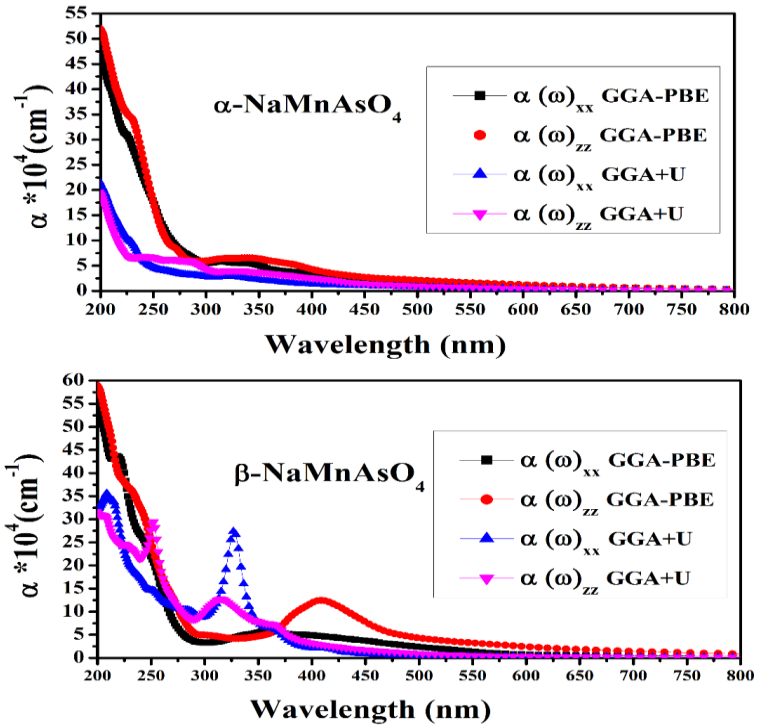

Figure VI-8: The calculated absorption coefficient of the $NaMnAsO_4$ compound using GGA-PBE and GGA+U approximations.

The imaginary part of the dielectric function $\varepsilon_2(\omega)$ is shown in Figure VI.9(b,d) for both the monoclinic and the orthorhombic structures with GGA-PBE and GGA+U approaches, a wide range of absorption region is observed with two main peaks, the first peak is observed for the monoclinic and orthorhombic phase at 3.56 eV and 3.2 eV for the monoclinic with GGA and GGA+U, respectively. For the orthorhombic structure, the peaks are observed at 2.85 eV and 4 eV with GGA and GGA+U, respectively. Besides the peak intensity is important by applying U (U=3.9eV) on Mn atoms for the orthorhombic structure, which enhanced the material absorption. The origin of these peaks is the inter-band transitions which can be related to the density of states. The peaks are due to the transition of electrons from 3d-Mn states, the spectra is observed to reach a maximum at 5.67 eV and 7.49 eV for the monoclinic structure, and at 6.10 eV, and 8.6 eV for the orthorhombic structure, with GGA and GGA+U approximations, respectively.

The analysis of the real (dispersive) part spectra of the dielectric function is shown in Figure VI.9(a,c), it is observed that the static dielectric constant ε_1 (0) is very important at zero frequency. In fact, the average value of the zero-frequency dielectric constant ε_1 (0) is 2.98 and 3 for both the monoclinic and the orthorhombic structures of $NaMnAsO_4$ with GGA approach, and 3 for both structures with GGA+U approximation. From this static dielectric value, the curves begin to increase and reach the maximum value of 4.77, 4 around 4.50 eV, and 6.72 eV for the monoclinic, the maximum value for the orthorhombic is reached at 4.8 and 4.1 at 4.9 eV.

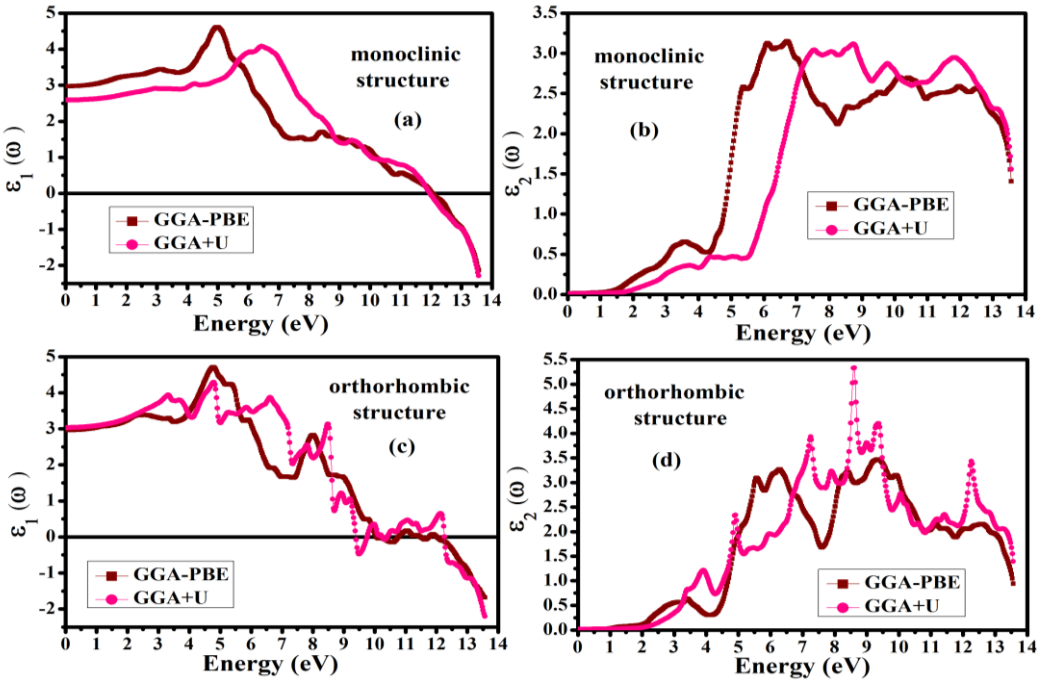

Figure VI-9: The real and imaginary part of the dielectric function of the monoclinic (a,b), and the orthorhombic (c,d) structures of $NaMnAsO_4$ compound.

Figure VI.10. shows the variations of the refractive index which describes the $NaMnAsO_4$ compound transparency and the reflectivity for the monoclinic and orthorhombic structures in the energy range of 0-14 eV. According to this figure, we note that the average value of n (0) is equal to 1.71 and 1.72 with the GGA+PBE approach, then 1.6 and 1.76 with GGA+U, for the monoclinic and the orthorhombic structures, respectively. The values of zero-energy of refractive index are in good agreement for both structures through the relationship $n_0^2 = \varepsilon_1(0)$ as shown in Table 4. The maximum refractive index corresponds to 2.10 at 4.9 eV and 2.22 at 4.7 eV for the monoclinic and the orthorhombic structures with the GGA+PBE approach, respectively. Besides, with GGA+U calculations, the maximum refractive index is found to be

located at 6.2 eV and 7.1 eV for the monoclinic and the orthorhombic structures, respectively, after these peak's values, the refractive index decreases in the higher energies. Therefore, according to the curves of reflectivity vs energy, the enhanced reflectivity in the compound for both structures is observed for the higher energies around 13 eV, the gradual increase and decrease of the reflectivity is shown in the higher energies and in the IR range for both structures, respectively. Then the reflectivity in the UV range is slight. The maximum reflectivity value for monoclinic and orthorhombic structures is around 0.58 and 0.62 or 58% and 62 % at 13.55 eV, with GGA-PBE approach, respectively. By means of the GGA+U, the maximum reflectivity is 58% and 67% for the monoclinic and the orthorhombic $NaMnAsO_4$ compound, respectively. Besides, n (ω) is similar to $\varepsilon_1(\omega)$ due to the relationship between them $n(\omega) = \sqrt{\varepsilon_1(\omega)}$. In the fact, Table. IV.5 presents the values of the static dielectric constant as well as the refractive index for both structures of $NaMnAsO_4$.

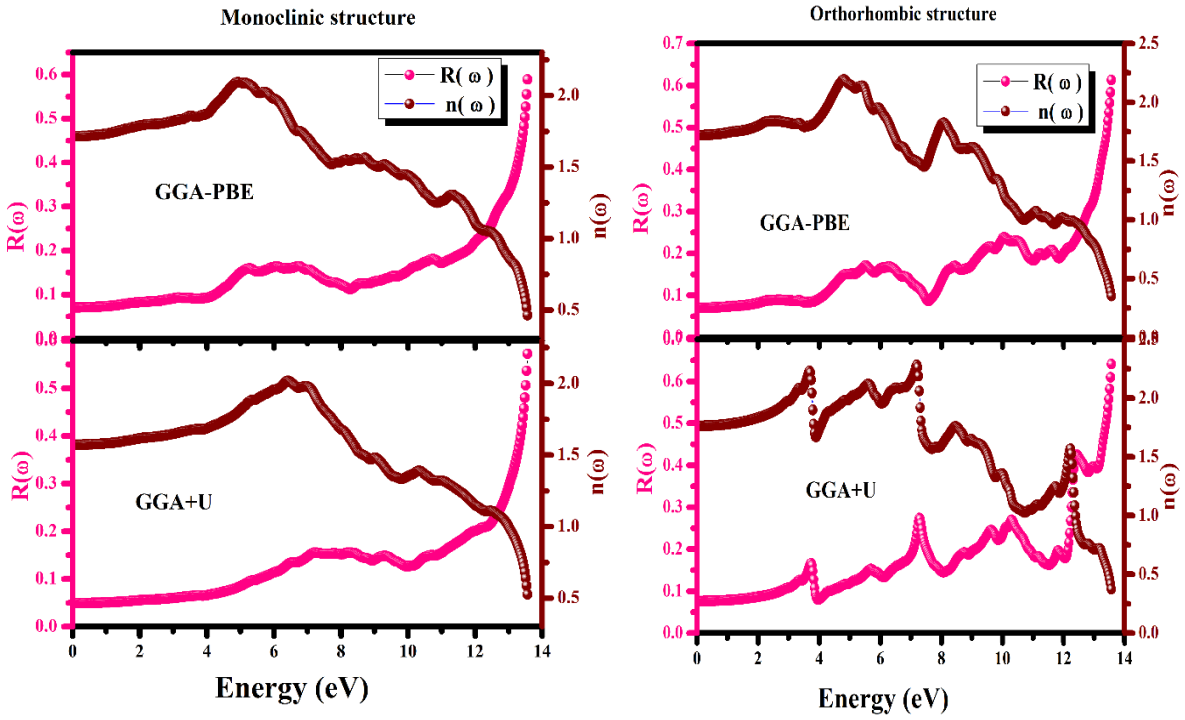

Figure VI-10: The reflectivity and refractive index of the $NaMnAsO_4$ compound.

Table VI-5: Static refractive index and static dielectric constant of $NaMnAsO_4$.

$NaMnAsO_4$ structure	GGA-PBE approach		GGA+U approach	
	$\varepsilon_1(\omega)$	n(ω)	$\varepsilon_1(\omega)$	n(ω)
Monoclinic phase	2.95	1.71	2.5	1.62

Orthorhombic phase	2.97	1.72	3	1.73

The color properties of the simples in the visible region are studied via the Commission International on Illumination CIE 1931 (*x*, *y*) chromatic diagram based on the computational reflectance data [282,283]. The CIE 1931 color spaces are the first defined quantitative relationships between wavelength distributions in the electromagnetic visible spectrum and physiologically perceived colors in human color vision. Furthermore, the correlated color temperature (CCT) is evaluated using McCamy's relation [284]:

$$CCT = -449p^3 + 3525p^2 - 6823.3p + 5520.33 \qquad \textbf{(12)}$$

Where $p = \frac{x - x_e}{y - y_e}$, (x, y) is the sample color coordinates and (x_e = 0.3320, y_e = 0.1858) indicates the coordinates of epicenter. The CIE chromaticity coordinates for the optimized samples and the obtained CCT data for the orthorhombic and monoclinic phases using GGA and GGA+U calculation are summarized in table 5 and table 6, respectively.

Table VI-6: CIE chromaticity coordinate of monoclinic and orthorhombic phase using GGA and GGA+U calculation

	Orthorhombic	**Monoclinic**
GGA-PBE approach	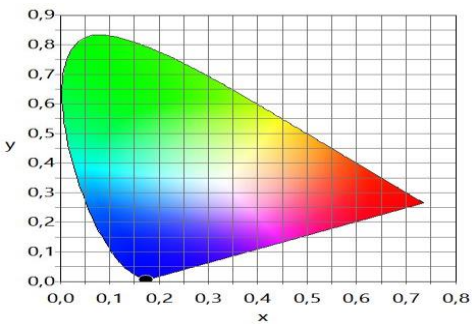	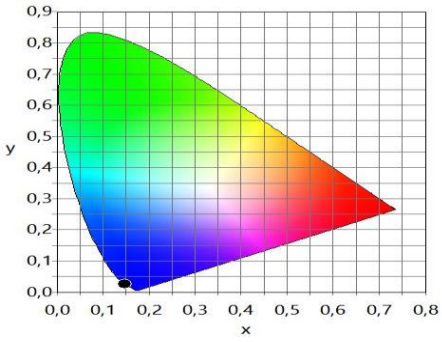
GGA + U approach	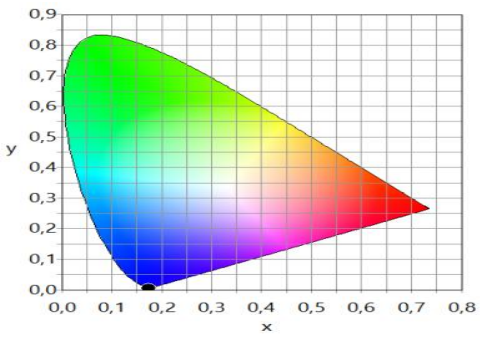	

VI.3.6 Thermoelectric Properties

The thermoelectricity corresponds to a group of phenomena in which a temperature difference is created by a potential such as an electric potential. Various materials semiconductors are generally used in these applications. The transport properties were performed near the Fermi level for both monoclinic and orthorhombic phases of $NaMnAsO_4$. The Seebeck coefficient (S), electrical conductivity, thermoelectric conductivity are calculated for a wide range of temperatures (T) between 0 K and 800 K using the semi-classical theory of Boltzmann implemented in the BoltzTrap code [276].

The Seebeck coefficient or thermoelectric power presents the possibility to quantify the relationship between the electric potential and the thermal potential. It has been established by experience that the values for common materials are of the order of μV / K. Figure VI.11. illustrates the evolution of the Seebeck coefficient (S) as a function of temperature for the monoclinic and the orthorhombic structures of $NaMnAsO_4$. Meanwhile, the Seebeck coefficient is directly related to the band structure. It is obvious that S increases gradually as the temperatures increases in the range of [100- 450]K. This evolution reveals that the Seebeck coefficient (S) appears high for the orthorhombic structure with the GGA and GGA+U approaches as compared to the monoclinic structure, at 300K, the value of S coefficient stood at 1.43 μV/K and 1.62 μV/K for monoclinic phase with the GGA and GGA+U, respectively. Besides for the orthorhombic, the value of S achieves 2 μV/K and 1.59 μV/K with the GGA and GGA+U, respectively. Indeed, the positive sign of the Seebeck coefficient suggests that the conduction of the material is made by holes. On the other hand, a similar variation of the Seebeck coefficient in the negative region reveals that the conduction is made by carriers of negative charges (electrons). therefore, the behavior of both structures is mainly enhanced by the load transfer effected by holes (p-type conduction).

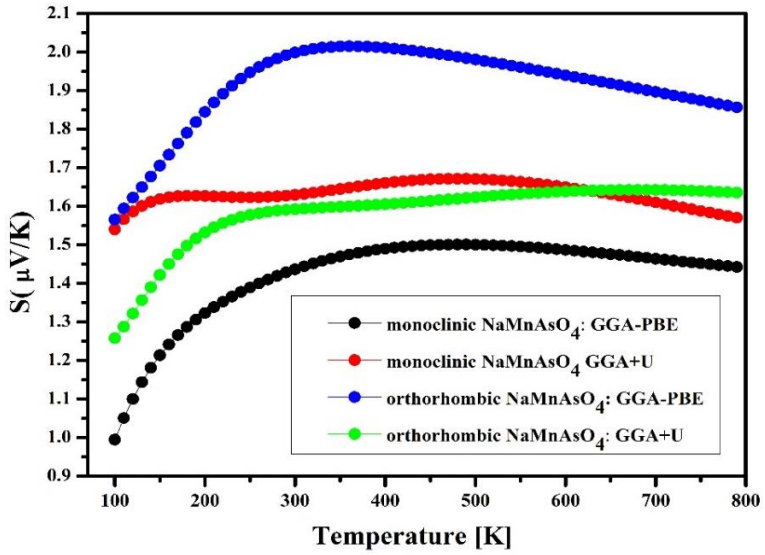

Figure VI-11: Seebeck coefficient (S) versus temperature of the $NaMnAsO_4$.

The plotted electrical conductivity as a function of temperature is shown in Figure VI.12. It is clear that the electrical conductivity σ increases gradually with temperature, except above 200K, it decreases for the monoclinic structure and don't exceed $2*10^{18}$ $(\Omega.m.s)^{-1}$. In fact, the growth of the electrical conductivity is due particularly to the increase in load carriers in the orthorhombic phase of $NaMnAsO_4$.

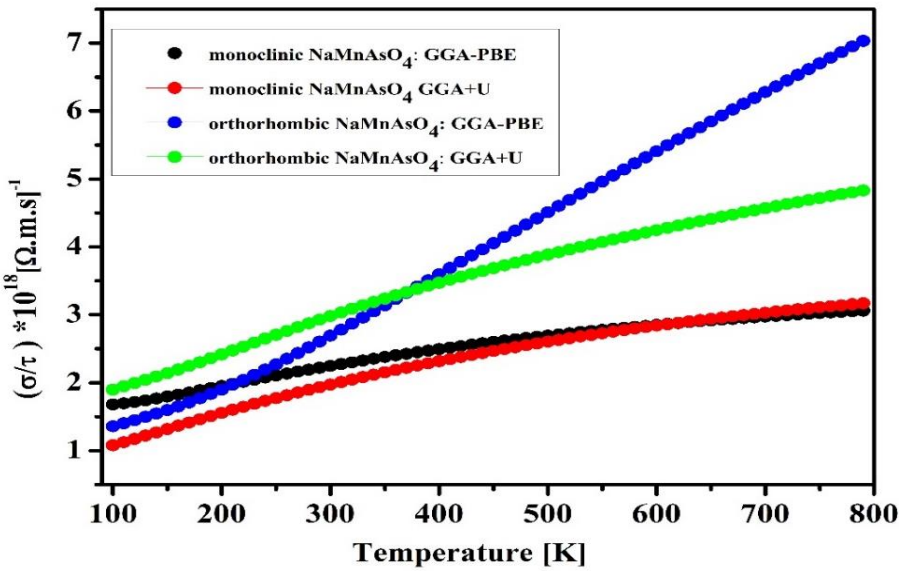

Figure VI-12: Electrical conductivity versus temperature of the $NaMnAsO_4$ material.

The curves of thermal conductivity as a function of temperature are presented in Figure VI.13. The evolution increases gradually with temperature, except that plotted of thermal conductivity for the orthorhombic structure appears to be important as compared to the variation

of the monoclinic structure, reaching a maximum in 800 K, probably caused a by the improvement of phonon diffusion in the material.

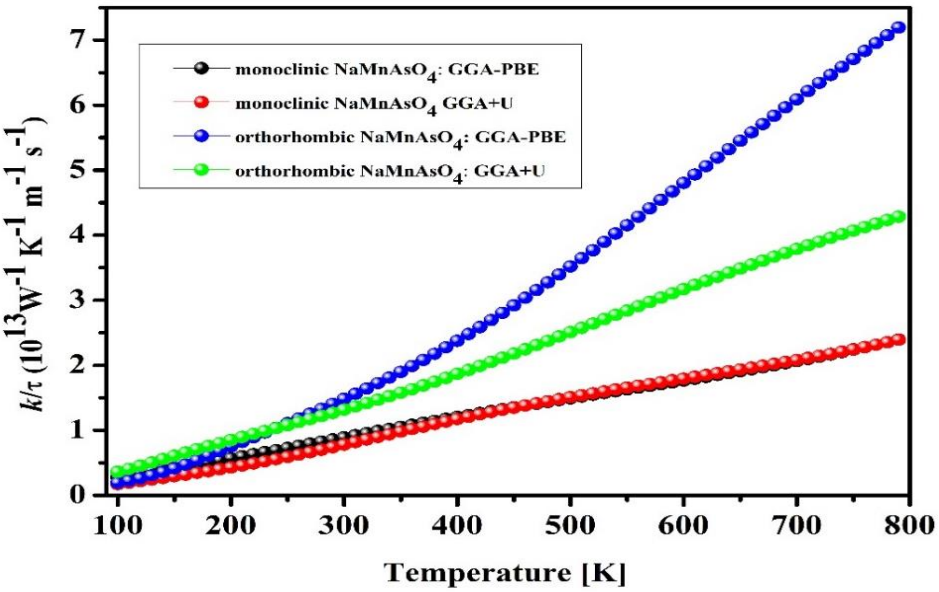

Figure VI-13: Evolution of the thermal conductivity as a function of temperature.

The figure of merit presents a dimensionless quantity, determined to measure the overall thermoelectric performance of materials. It is given by the following relation [285,286]:

$$ZT = \frac{\sigma S^2 T}{k} \qquad \textbf{(13)}$$

T is the absolute temperature, S is the Seebeck coefficient, σ is the electrical conductivity and K is the thermal conductivity.

As a tradition a good thermoelectrical material must have a high figure of merit value. The variation of the figure of merit as a function of temperature is presented in Figure VI.14. According to our obtained results, the curve of the figure of merit ZT for orthorhombic and monoclinic structures of $NaMnAsO_4$ research at room temperature 2.2 and 1.5 with the GGA approach, respectively. Then for the GGA+U, the value of ZT increases to 2 for the monoclinic phase and decreases to 1.72 for the orthorhombic phase. Above 500K, the evaluation of ZT appears high for both structures. Besides, a high value of ZT is obtained due to the high Seebeck coefficient, and the low thermal conductivity. All these properties suggest that the $NaMnAsO_4$ would be a suitable candidate for thermoelectric applications. Hence the need for an experimental synthesis and characterization to further assess the potential of this material.

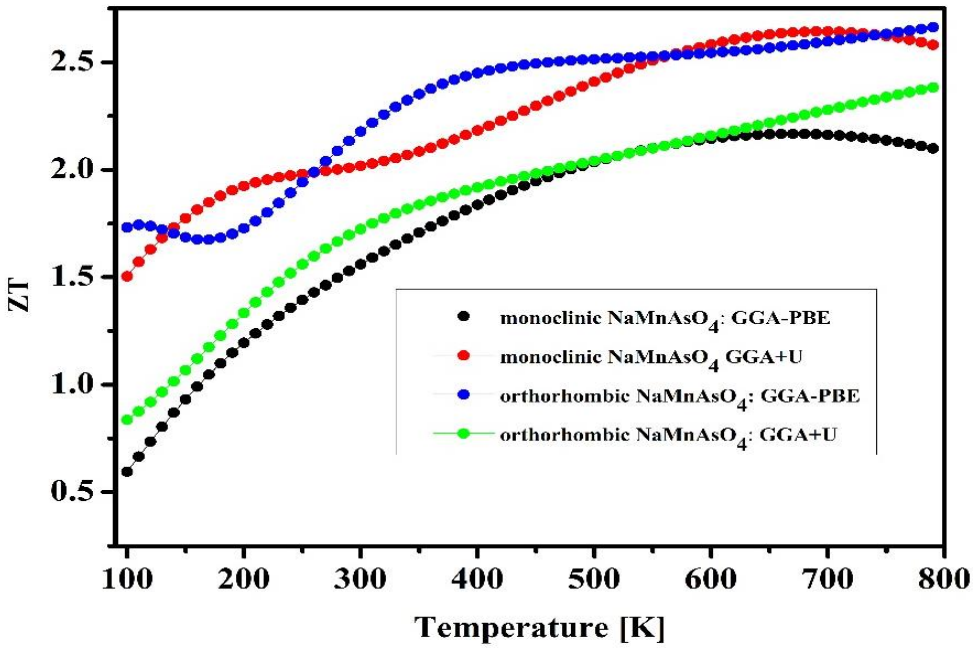

Figure VI-14: The evolution of the merit (ZT) as a function of temperature.

Conclusion

In conclusion, Density Functional Theory (DFT) and the semi-classical Boltzmann theory were performed to study the properties of the $NaMnAsO_4$ cluster. To improve the bandgap energy, we have employed the GGA+U approach with U=3.9 eV for both, the monoclinic and the orthorhombic structures. The electronic, optical, magnetic, and thermoelectric properties were investigated to well-understand the material's behavior. Both structures (monoclinic and orthorhombic) of the $NaMnAsO_4$ showed good optical properties in the ultraviolet region, which confirms its suitability for optoelectronic applications. The total and partial density of states shows the origin of the magnetic properties. The total moment in the bulk changes when the structure of the material changes. Moreover, the semi-classical Boltzmann theory results show that both structures of $NaMnAsO_4$ could be excellent thermoelectric material. Due to its multifunctional properties, the present study gives a good initiative to researchers in order to pave the way to further deep experimental insight into $NaMnAsO_4$ for optoelectronic-thermoelectric application.

General Conclusions

In this thesis, density functional theory was used in conjunction with Boltzmann transport theory to examine the electronic, optical, electrical properties of the organic-inorganic hybrid materials, and the thermoelectric properties of the transition metal oxide materials.

By DFT calculations, we tried to adjust an new theoretical method to calculate the crucial parameters requested by industrial community such as short circuit current, open circuit voltage, quantum efficiency, and electrical power of a given photovoltaic material. This method opens the ability to master the correlation between synthesis and efficiency of all photovoltaic materials without realizing the photovoltaic device. All computed curves and values have been compared to experimental data of the well-known material $CH_3NH_3PbI_3$.

The crystals of $(C_6H_{10}N_2)_2[Co(H_2O)_4P_2Mo_5O_{23}].6H_2O$ with triclinic structure were characterized by X-ray powder diffraction (XRD). The profiles of the density of states (DOS), the optical spectra including the real and imaginary part of the dielectric function, and the measured magnetocaloric properties were presented and analyzed in detail. The results found are in agreement with experimental measurements. As pertinent results, the compound presents a high absorption coefficient in the visible range. A systematic analysis of the experimental and theoretical results shows a good bandgap, a high optical property, and a low magnetocaloric effect which reveals promising original material in optoelectronic, and photovoltaic applications.

The novel *trans*-$[Cu(L\text{-}Arg)_2(ReO_4)_2]$ (CuLARe) complex has been studied using the density functional theory (DFT), within the generalized gradient approximation (GGA-PBE).

The experimental band gap estimated from the Kubelka-Munk function is found to be in good agreement with the calculated band gap found by DFT. The density of states, band structure, density of charge, absorption coefficient, and reflectivity are presented and analyzed in detail. The partial densities of states show that ReO_4^- ligand in the material plays a crucial role in different properties of the *trans*-[$Cu(L\text{-}Arg)_2(ReO_4)_2$] material. Moreover, the experimental reflectance is employed to estimate the scattering coefficient using a semi-empirical equation Kubelka-Munk (K-M).

The electronic, optical, magnetic, and thermoelectrical properties of both, the monoclinic (α-form) and the orthorhombic (β-form) phases of sodium manganese (II) arsenate $NaMnAsO_4$ cluster are investigated comprehensively by the first-principle calculations based on the density Functional Theory. The full-potential linearized augmented plane waves method within the GGA and GGA+U approaches have been performed by the Wien2k software. Thermodynamic stability is confirmed by means of formation energy (ΔH_f). The indirect bandgaps are observed for the monoclinic phase, then the direct bandgaps are reported at Γ-symmetry point for the orthorhombic phase. The density of state, besides the band structure calculation, revealed that the studied material can be identified as a ferromagnetic semiconductor at low temperature with an optical bandgap energy of 1.35 eV and 0.83 eV for monoclinic and orthorhombic phases with GGA approach, as well as 1.27 eV and 1.59 eV with GGA+U approach, respectively. The refractive index range is 1.5 - 2.4 along with a wide absorption band in the UV region, which makes this material outstanding for optoelectronic devices. The thermoelectric properties for both structures have also been investigated using the BoltzTraP package. The obtained electrical conductivity, as well as the figure of merit, are found to be important for thermoelectrical devices. This suggests that $NaMnAsO_4$ could pave the way to further experimental research on optoelectronic-thermoelectric applications.

If there is one lesson, I have learned in this thesis work, it is that the work is never over. Our desire to learn as researchers is insatiable, and as such, there is much more I would like to investigate within these families of materials. For example, studying more the magnetic properties of the transition metal oxide $NaMnAsO_4$ material with different approximations, and provide an experimental study. For such a well-known material, it is perplexing to consider such discoveries on playing on the material's architecture such us investigate thin film materials. As the miniaturizations of electronic devices continue, the components are shifting towards thin films. For this reason, the investigation of thin film of the

organic-inorganic hybrid and the transition metal oxide materials may yield unique properties and interactions

Bibliography

[1] Commision of the European Communities. Green paper: A European strategy for sustainable, competitive and secure energy, 2006.

[2] Teske, S., Pregger, T., Simon, S., Naegler, T., Graus, W., & Lins, C. (2011). Energy [R] evolution 2010—a sustainable world energy outlook. *Energy Efficiency*, *4*(3), 409-433.

[3] Criqui, P., & Kouvaritakis, N. (2000). World energy projections to 2030. *International journal of global energy issues*, *14*(1-4), 116-136.

[4] Intergovernmental Panel on Climate Change. Climate change 2007: The physical science basis. Technical report, United Nations, 2007.

[5] Webster, M. D., Babiker, M., Mayer, M., Reilly, J. M., Harnisch, J., Hyman, R., ... & Wang, C. (2002). Uncertainty in emissions projections for climate models. *Atmospheric environment*, *36*(22), 3659-3670.

[6] Hoegh-Guldberg, O., Mumby, P. J., Hooten, A. J., Steneck, R. S., Greenfield, P., Gomez, E., ... & Hatziolos, M. E. (2007). Coral reefs under rapid climate change and ocean acidification. *science*, *318*(5857), 1737-1742.

[7] M.A. Green, K. Emery, Y. Hisikawa, and W. Warta. Solar cell efficiency tables (version 30).Progress in Photovoltaics: Research and Applications,15:425–430, 2007.],

[8] M.A. Green.Solar cells: operating principles, technology, and system applications. University of New South Wales, Kensington, N.S.W., 1992.

[9] Wenham, S. R., & Green, M. A. (1996). Silicon solar cells. *Progress in Photovoltaics: Research and Applications*, *4*(1), 3-33.

[10] McEvoy, A., Castaner, L., & Markvart, T. (2012). *Solar cells: materials, manufacture and operation*. Academic Press.

[11] Smil, Vaclav. *Energy at the crossroads: global perspectives and uncertainties*. MIT press, 2005.

[12] Emery, Keith, and D. Myers. "Reference solar spectral irradiance: air mass 1.5." *Center, RERD, Ed* (2009).

[13] Shehabi, Arman, et al. "United states data center energy usage report." (2016).

[14] Solar Power Europe (SPE), "Global Market Outlook For Solar Power 2015-2019,"2015.

[15] Becquerel, M. E. "Mémoire sur les effets électriques produits sous l'influence des rayons solaires." *Comptes rendus hebdomadaires des séances de l'Académie des Sciences* 9 (1839): 561-567.

[16] W. G. Adams and R. E. Day, "The Action of Light on Selenium," Proc. Royal Soc. (London), vol. A25, pp. 113–117, 1877.

[17] C. E. Fritts, "On a New Form of Selenium Photocell," American Journal of Science, vol. 26, pp. 465–472, 1883.

[18] M. A. Green, "Photovoltaics: Coming on age," PVSC 1990, vol. 1, pp. 1–8, 1990.

[19] L. O. Grondahl, "The Copper-Cuprous-Oxide Rectifier and Photoelectric Cell," Rev. Mod. Phys., vol. 5, p. 141, 1933.

[20] L. Bergmann, "Uber eine neue Selen- Sperrschicht Photozelle," Physikalische Zeitschrift, vol. 32, p. 286, 1931.

[21] F. C. Nix and A. W. Treptwo, "A Thallous Sulphide Photo EMF Cell," Journal Opt. Society of America, vol. 29, p. 457, 1939.

[22] Chapin, Daryl M., Calvin S. Fuller, and Gerald L. Pearson. "A new silicon p-n junction photocell for converting solar radiation into electrical power." *Journal of Applied Physics* 25.5 (1954): 676-677.

[23] Shockley, William, and Hans J. Queisser. "Detailed balance limit of efficiency of p-n junction solar cells." *Journal of applied physics* 32.3 (1961): 510-519.

[24] Peter, Laurence M. "Towards sustainable photovoltaics: the search for new materials." *Philosophical Transactions of the Royal Society A: Mathematical, Physical and Engineering Sciences* 369.1942 (2011): 1840-1856.

[25] Green, Martin A. "Third generation photovoltaics." (2006).

[26] Nelson, Cory A., Nicholas R. Monahan, and X-Y. Zhu. "Exceeding the Shockley–Queisser limit in solar energy conversion." *Energy & Environmental Science* 6.12 (2013): 3508-3519.

[27] Brunetti, Fulvio G., Rajeev Kumar, and Fred Wudl. "Organic electronics from perylene to organic photovoltaics: painting a brief history with a broad brush." *Journal of Materials Chemistry* 20.15 (2010): 2934-2948.

[28] Delgado, Juan Luis, et al. "Organic photovoltaics: a chemical approach." *Chemical communications* 46.27 (2010): 4853-4865.

[29] Mazzio, Katherine A., and Christine K. Luscombe. "The future of organic photovoltaics." *Chemical Society Reviews* 44.1 (2014): 78-90.

[30] Kearns, David, and Melvin Calvin. "Photovoltaic effect and photoconductivity in laminated organic systems." *The Journal of chemical physics* 29.4 (1958): 950-951.

[31] Tang, Ching W. "Two-layer organic photovoltaic cell." *Applied physics letters* 48.2 (1986): 183-185.

[32] Yu, Gang, et al. "Polymer photovoltaic cells: enhanced efficiencies via a network of internal donor-acceptor heterojunctions." *Science* 270.5243 (1995): 1789-1791.

[33] Hiramoto, Masahiro, Hiroshi Fujiwara, and Masaaki Yokoyama. "Three-layered organic solar cell with a photoactive interlayer of codeposited pigments." *Applied physics letters* 58.10 (1991): 1062-1064.

[34] Halls, J. J. M., et al. "Efficient photodiodes from interpenetrating polymer networks." *Nature* 376.6540 (1995): 498-500.

[35] Hadipour, Afshin, Bert de Boer, and Paul WM Blom. "Organic tandem and multi-junction solar cells." *Advanced functional materials* 18.2 (2008): 169-181.

[36] Ameri, Tayebeh, et al. "Organic tandem solar cells: A review." *Energy & Environmental Science* 2.4 (2009): 347-363.

[37] Li, Ning, et al. "Towards 15% energy conversion efficiency: a systematic study of the solution-processed organic tandem solar cells based on commercially available materials." *Energy & Environmental Science* 6.12 (2013): 3407-3413.

[38] Riede, Moritz, et al. "Efficient organic tandem solar cells based on small molecules." *Advanced Functional Materials* 21.16 (2011): 3019-3028.

[39] Kim, Jin Young, et al. "Efficient tandem polymer solar cells fabricated by all-solution processing." *Science* 317.5835 (2007): 222-225.

[40] Sista, Srinivas, et al. "Tandem polymer photovoltaic cells—current status, challenges and future outlook." *Energy & Environmental Science* 4.5 (2011): 1606-1620.

[41] You, Jingbi, et al. "Recent trends in polymer tandem solar cells research." *Progress in polymer science* 38.12 (2013): 1909-1928.

[42] Tregnago, Giulia, et al. "The power of intermolecular interactions in organic semiconductors: from threaded molecular wires to P3HT nanofibres and PCBM single crystals."

[43] Brabec, Christoph J., N. Serdar Sariciftci, and Jan C. Hummelen. "Plastic solar cells." *Advanced functional materials* 11.1 (2001): 15-26.

[44] Peet, Jeffrey, et al. "The role of processing in the fabrication and optimization of plastic solar cells." *Advanced Materials* 21.14-15 (2009): 1521-1527.

[45] Brabec, Christoph J., et al. "Polymer–fullerene bulk-heterojunction solar cells." *Advanced Materials* 22.34 (2010): 3839-3856.

[46] Gendron, David, and Mario Leclerc. "New conjugated polymers for plastic solar cells." *Energy & Environmental Science* 4.4 (2011): 1225-1237.

[47] Peet, Jeffrey, Alan J. Heeger, and Guillermo C. Bazan. "“Plastic” solar cells: self-assembly of bulk heterojunction nanomaterials by spontaneous phase separation." *Accounts of Chemical Research* 42.11 (2009): 1700-1708.

[48] Roncali, Jean, et al. "Molecular and supramolecular engineering of π-conjugated systems for photovoltaic conversion." *Thin solid films* 511 (2006): 567-575.

[49] Walker, Bright, Chunki Kim, and Thuc-Quyen Nguyen. "Small molecule solution-processed bulk heterojunction solar cells." *Chemistry of Materials* 23.3 (2011): 470-482.

[50] Mishra, Amaresh, and Peter Bäuerle. "Small molecule organic semiconductors on the move: promises for future solar energy technology." *Angewandte Chemie International Edition* 51.9 (2012): 2020-2067.

[51] Wang, Mingfeng, and Fred Wudl. "Top-down meets bottom-up: organized donor–acceptor heterojunctions for organic solar cells." *Journal of Materials Chemistry* 22.46 (2012): 24297-24314.

[52] Lin, Yuze, Yongfang Li, and Xiaowei Zhan. "Small molecule semiconductors for high-efficiency organic photovoltaics." *Chemical Society Reviews* 41.11 (2012): 4245-4272.

[53] Hu, Wenping, et al. *Organic optoelectronics*. John Wiley & Sons, 2012.

[54] Chen, Yongsheng, Xiangjian Wan, and Guankui Long. "High performance photovoltaic applications using solution-processed small molecules." *Accounts of chemical research* 46.11 (2013): 2645-2655.

[55] Ala'a, F. Eftaiha, et al. "Recent advances of non-fullerene, small molecular acceptors for solution processed bulk heterojunction solar cells." *Journal of Materials Chemistry A* 2.5 (2014): 1201-1213.

[56] Roncali, Jean, Philippe Leriche, and Philippe Blanchard. "Molecular materials for organic photovoltaics: small is beautiful." *Advanced Materials* 26.23 (2014): 3821-3838.

[57] You, Jingbi, et al. "A polymer tandem solar cell with 10.6% power conversion efficiency." *Nature communications* 4.1 (2013): 1-10.

[58] Heliatek GmbH, Heliatek consolidates its technology leadership by establishing a new world record for organic solar technology with a cell efficiency of 12%, 2013. Available at: http://www.heliatek.com/newscenter/latest_news/neuer-weltrekord-fur-organische-solarzellenheliatek-behauptet-sich-mit-12-zelleffizienz-als-technologiefuhrer/?lang=en (Accessed Jan. 2015).

[59] Mitsubishi Chemical Corporation, Achieved power conversion efficiency of 11.7%, the highest in the world!, Available at : http://www.m-kagaku.co.jp/english/r_td/strategy/topics/opv/index.html (Accessed Jan.2015)

[60] Hagfeldt, Anders, et al. "Dye-sensitized solar cells." *Chemical reviews* 110.11 (2010): 6595-6663.
[61] Nazeeruddin, Md K., Etienne Baranoff, and Michael Grätzel. "Dye-sensitized solar cells: A brief overview." *Solar energy* 85.6 (2011): 1172-1178.

[62] O'regan, Brian, and Michael Grätzel. "A low-cost, high-efficiency solar cell based on dye-sensitized colloidal TiO 2 films." *nature* 353.6346 (1991): 737-740.

[63] Mathew, Simon, et al. "Dye-sensitized solar cells with 13% efficiency achieved through the molecular engineering of porphyrin sensitizers." *Nature chemistry* 6.3 (2014): 242-247.

[64] Odobel, Fabrice, et al. "Recent advances and future directions to optimize the performances of p-type dye-sensitized solar cells." *Coordination Chemistry Reviews* 256.21-22 (2012): 2414-2423.

[65] Docampo, Pablo, et al. "Lessons learned: from dye-sensitized solar cells to all-solid-state hybrid devices." *Advanced Materials* 26.24 (2014): 4013-4030.

[66] Fakharuddin, A. "Jose R. Brown TM Fabregat-Santiago F. Bisquert J." *Energy Environ. Sci* 7 (2014): 3952.

[67] Hernandez, Rebecca R., et al. "Environmental impacts of utility-scale solar energy." *Renewable and sustainable energy reviews* 29 (2014): 766-779.

[68] Brabec, Christoph J. "Organic photovoltaics: technology and market." *Solar energy materials and solar cells* 83.2-3 (2004): 273-292.

[69] Benanti, Travis L., and D. Venkataraman. "Organic solar cells: An overview focusing on active layer morphology." *Photosynthesis research* 87.1 (2006): 73-81.

[70] Williams, A. Organic PV: can UK start-ups carve out a niche? 2012; Available from: http://optics.org/indepth/3/6/2_/ Nunzi, J.-M., Organic photovoltaic materials and devices. C. R. Physique, 2002. 3(4): p. 523–542

[71] Nunzi, Jean-Michel. "Organic photovoltaic materials and devices." *Comptes Rendus Physique* 3.4 (2002): 523-542.

[72] Oxford English Dictionary, OxfordUniversity Press.

[73] http://en.wikipedia.org/wiki/Hybridwikipageshybrids

[74]/http://www.gazelle.nl/nl/collectie/fietsen/hybride/ultimate-xtra.html.

[75] Shen, Jun, et al. "A coupled cluster approach with a hybrid treatment of connected triple excitations for bond-breaking potential energy surfaces." *The Journal of chemical physics* 132.11 (2010): 114115.

[76] Fan, Changjun, et al. "High-efficiency phosphorescent hybrid organic–inorganic light-emitting diodes using a solution-processed small-molecule emissive layer." *ACS applied materials & interfaces* 7.37 (2015): 20769-20778.

[77] Kelley, Tommie W., et al. "Recent progress in organic electronics: Materials, devices, and processes." *Chemistry of Materials* 16.23 (2004): 4413-4422.

[78] Hung, L. S., and C. H. Chen. "Recent progress of molecular organic electroluminescent materials and devices." *Materials Science and Engineering: R: Reports* 39.5-6 (2002): 143-222.

[79] Ali, Roushown, and Masatomo Yashima. "Space group and crystal structure of the perovskite CaTiO3 from 296 to 1720 K." *Journal of Solid State Chemistry* 178.9 (2005): 2867-2872.

[80] Jonker, G. H. "van Santen." *Physica* 16 (1950): 337.

[81] Buschow, K. H. J., P. A. Naastepad, and F. F. Westendorp. "Preparation of SmCo5 permanent magnets." *Journal of Applied Physics* 40.10 (1969): 4029-4032.

[82] Goldschmidt, V. M. "Naturwissenschaften." *Naturwissenschaften* 21 (1926): 477-485.

[83] Megaw, Helen D. "Crystal structure of barium titanate." *Nature* 155.3938 (1945): 484-485.

[84] Wiley, John. *Sons*. Vol. 1. No. 11. New York; NY: Inc, 2001.

[85] Ahmad, S., Husain, A., Khan, M. M. A., Khan, I., Khan, A., & Asiri, A. M. (2021). Perovskite-based material for sensor applications. In *Hybrid Perovskite Composite Materials* (pp. 135-145). Woodhead Publishing.

[86] Tarragó, D. P., Moreno, B., Chinarro Martín, E., & Sousa, V. C. D. (2016). Perovskites used in fuel cells. *Pan, Likun; Zhu, Guang (ed.). Perovskite materials: synthesis, characterisation, properties, and applications [recurso eletrônico].[Rijeka, Croatia]: InTech, 2016. ch. 21, p. 619-637.*

[87] Li, Bixin, et al. "Metal halide perovskites for resistive switching memory devices and artificial synapses." *Journal of Materials Chemistry C* 7.25 (2019): 7476-7493.

[88] Petrović, Miloš, Vijila Chellappan, and Seeram Ramakrishna. "Perovskites: solar cells & engineering applications–materials and device developments." *Solar Energy* 122 (2015): 678-699.

[89] Singh, Pramod K., et al. "New class of lead free perovskite material for low-cost solar cell application." *Materials Research Bulletin* 97 (2018): 572-577.

[90] Kojima, Akihiro, et al. "Organometal halide perovskites as visible-light sensitizers for photovoltaic cells." *Journal of the American Chemical Society* 131.17 (2009): 6050-6051.

[91] Burschka, Julian, et al. "Sequential deposition as a route to high-performance perovskite-sensitized solar cells." *Nature* 499.7458 (2013): 316-319.

[92] Correa-Baena, Juan-Pablo, et al. "The rapid evolution of highly efficient perovskite solar cells." *Energy & Environmental Science* 10.3 (2017): 710-727.

[93] Bullis, Kevin (8 August 2013). *"A Material That Could Make Solar Power "Dirt Cheap""*. *MIT Technology Review*. *Retrieved 8 August 2013*.

[94] Li, Hangqian, et al. "A modified sequential deposition method for fabrication of perovskite solar cells." Solar Energy 126 (2016): 243-251.

[95] Xiao, Y., Han, G., Li, Y., Li, M., Chang, Y., & Wu, J. (2014). Preparation of high performance perovskite-sensitized nanoporous titanium dioxide photoanodes by in situ method for use in perovskite solar cells. *Journal of Materials Chemistry A*, *2*(39), 16531-16537.

[96] *"Research Cell Efficiency Records" (PDF)*. Office of Energy Efficiency & Renewable Energy. 2020.

[97] Eames, Christopher, et al. "Ionic transport in hybrid lead iodide perovskite solar cells." *Nature communications* 6.1 (2015): 1-8.

[98] Luo, Jingshan, et al. "Water photolysis at 12.3% efficiency via perovskite photovoltaics and Earth-abundant catalysts." *Science* 345.6204 (2014): 1593-1596.

[99] https://www.greencarcongress.com/2014/09/20140926-epfl.html.

[100] P. J. Dereń, A. Bednarkiewicz et al. Laser action in LaAl O3: Nd3+ single crystal. Journal of Applied Physics, 103, 4, 2008.

[101] Deschler, Felix, et al. "High photoluminescence efficiency and optically pumped lasing in solution-processed mixed halide perovskite semiconductors." *The journal of physical chemistry letters* 5.8 (2014): 1421-1426.

[102] Zhuang, W. W., et al. "Novel colossal magnetoresistive thin film nonvolatile resistance random access memory (RRAM)." *Digest. International Electron Devices Meeting,*. IEEE, 2002.

[103] Jang, Chan Wook, et al. "Significantly-enhanced stabilities in flexible hybrid organic-inorganic perovskite resistive random access memories by employing multilayer graphene transparent conductive electrodes." *Journal of the Korean Physical Society* 73.7 (2018): 934-939.

[104] Meyer, Jens, et al. "Transition metal oxides for organic electronics: energetics, device physics and applications." *Advanced materials* 24.40 (2012): 5408-5427.

[105] Greiner, Mark T., et al. "Transition metal oxide work functions: the influence of cation oxidation state and oxygen vacancies." *Advanced Functional Materials* 22.21 (2012): 4557-4568.

[106] Macco, Bart, Bas WH van de Loo, and Wilhelmus MM Kessels. "Atomic layer deposition for high efficiency crystalline silicon solar cells." *Atomic Layer Deposition in Energy Conversion Applications* (2017): 41-99.

[107] Greiner, Mark T., and Zheng-Hong Lu. "Thin-film metal oxides in organic semiconductor devices: their electronic structures, work functions and interfaces." *NPG Asia Materials* 5.7 (2013): e55-e55.

[108] Wu, Hongbin, and Lai-Sheng Wang. "A study of nickel monoxide (NiO), nickel dioxide (ONiO), and Ni (O 2) complex by anion photoelectron spectroscopy." *The Journal of chemical physics* 107.1 (1997): 16-21.

[109] Mews, Mathias, Lars Korte, and Bernd Rech. "Oxygen vacancies in tungsten oxide and their influence on tungsten oxide/silicon heterojunction solar cells." *Solar Energy Materials and Solar Cells* 158 (2016): 77-83.

[110] Liu, Rui, et al. "Water splitting by tungsten oxide prepared by atomic layer deposition and decorated with an oxygen-evolving catalyst." *Angewandte Chemie International Edition* 50.2 (2011): 499-502.

[111] Hohenberg, P., and W. Kohn. "Inhomogeneous Electron Gas Phys. Rev. 136." *B864* (1964).

[112] Schrödinger, Erwin. "An undulatory theory of the mechanics of atoms and molecules." *Physical review* 28.6 (1926): 1049.

[113] Seminario, Jorge M., ed. *Recent developments and applications of modern density functional theory*. Elsevier, 1996.

[114] Daniel, C. "Density Functional Theories and Coordination Chemistry." (2020).

[115] [M. Born, R. Oppenheimer, Quantum Theory of Molecules, Annalen Der Physik 84 (1927) 0457-0484.

[116] Fock, Vladimir. "Näherungsmethode zur Lösung des quantenmechanischen Mehrkörperproblems." *Zeitschrift für Physik* 61.1-2 (1930): 126-148.

[117] Slater, John C. "Note on Hartree's method." *Physical Review* 35.2 (1930): 210.

[118] Lennard-Jones, John E. "The electronic structure of some diatomic molecules." *Transactions of the Faraday Society* 25 (1929): 668-686.

[119] Szabo, Attila, and Neil S. Ostlund. *Modern quantum chemistry: introduction to advanced electronic structure theory*. Courier Corporation, 2012.

[120] Engel, Thomas. "Basic overview of chemoinformatics." *Journal of chemical information and modeling* 46.6 (2006): 2267-2277.

[121] Thomas, Llewellyn H. "The calculation of atomic fields." *Mathematical proceedings of the Cambridge philosophical society*. Vol. 23. No. 5. Cambridge University Press, 1927.

[122] Fermi, Enrico. "Eine statistische Methode zur Bestimmung einiger Eigenschaften des Atoms und ihre Anwendung auf die Theorie des periodischen Systems der Elemente." *Zeitschrift für Physik* 48.1-2 (1928): 73-79.

[123] Tsuneda, Takao. "Density functional theory in quantum chemistry." (2014): 978-4.

[124] Mardirossian, Narbe, and Martin Head-Gordon. "Thirty years of density functional theory in computational chemistry: an overview and extensive assessment of 200 density functionals." *Molecular Physics* 115.19 (2017): 2315-2372.

[125] Kohn, Walter, and Lu Jeu Sham. "Self-consistent equations including exchange and correlation effects." *Physical review* 140.4A (1965): A1133.

[126] Vosko, Seymour H., Leslie Wilk, and Marwan Nusair. "Accurate spin-dependent electron liquid correlation energies for local spin density calculations: a critical analysis." *Canadian Journal of physics* 58.8 (1980): 1200-1211.

[127] Mardirossian, Narbe, and Martin Head-Gordon. "Thirty years of density functional theory in computational chemistry: an overview and extensive assessment of 200 density functionals." *Molecular Physics* 115.19 (2017): 2315-2372.

[128] J.P. Perdew, K. Burke, M. Ernzerhof, Generalized Gradient Approximation Made Simple, Physical Review Letters 77 (1996) 3865-3868.

[129] A.D. Becke, Density-Functional Exchange-Energy Approximation with Correct Asymptotic-Behavior, Physical Review A 38 (1988) 3098-3100.

[130] J.P. Perdew, J.A. Chevary, S.H. Vosko, K.A. Jackson, M.R. Pederson, D.J. Singh, C. Fiolhais, Atoms, Molecules, Solids, and Surfaces - Applications of the Generalized Gradient Approximation for Exchange and Correlation, Physical Review B 46 (1992) 6671-6687.

[131] C.T. Lee, W.T. Yang, R.G. Parr, Development of the Colle-Salvetti CorrelationEnergy Formula into a Functional of the Electron-Density, Physical Review B 37(1988) 785-789.

[132] J.P. Perdew, J.A. Chevary, S.H. Vosko, K.A. Jackson, M.R. Pederson, D.J. Singh, C. Fiolhais, Atoms, Molecules, Solids, and Surfaces - Applications of the Generalized Gradient Approximation for Exchange and Correlation, Physical Review B 46 (1992) 6671-6687.

[133] H. J. F. Jansen and A. J. Freeman, \Total-energy full-potential linearized augmented-plane-wave method for bulk solids: Electronic and structural properties of tungsten,“Phys.Rev. B, vol. 30, pp. 561{569, Jul 1984.

[134] J. C. Slater, \An augmented plane wave method for the periodic potential problem, “Phys. Rev., vol. 92, pp. 603{608, Nov 1953.

[135] Schwarz, Karlheinz, and Peter Blaha. "Solid state calculations using WIEN2k." *Computational Materials Science* 28.2 (2003): 259-273.

[136] Yu, Rici, D. Singh, and H. Krakauer. "All-electron and pseudopotential force calculations using the linearized-augmented-plane-wave method." *Physical Review B* 43.8 (1991): 6411.

[137] Bylander, D. M., and Leonard Kleinman. "Exact Phillips-Kleinman-like pseudopotential for transition metals." *Physical Review B* 46.15 (1992): 9837.

[138] Smallwood, C. Jay, et al. "A computationally efficient exact pseudopotential method. I. Analytic reformulation of the Phillips-Kleinman theory." *The Journal of chemical physics* 125.7 (2006): 074102.

[139] Likos, Christos N., et al. "Why do ultrasoft repulsive particles cluster and crystallize? Analytical results from density-functional theory." *The Journal of chemical physics* 126.22 (2007): 224502.

[140] Askerov, Bachram M. *Electron transport phenomena in semiconductors*. World scientific, 1994.

[141] Kaviany, Massoud. *Heat transfer physics*. Cambridge University Press, 2014.

[142] C. Hamaguchi. Basic semiconductor physics. Springer Science & Business Media, 2009.

[143] Madsen, Georg KH, and David J. Singh. "BoltzTraP. A code for calculating band-structure dependent quantities." *Computer Physics Communications* 175.1 (2006): 67-71.

[144] Habibi, Mehran, et al. "Progress in emerging solution-processed thin film solar cells–Part II: Perovskite solar cells." *Renewable and Sustainable Energy Reviews* 62 (2016): 1012-1031.

[145] Spanopoulos, Ioannis, et al. "Unraveling the chemical nature of the 3D "hollow" hybrid halide perovskites." *Journal of the American Chemical Society* 140.17 (2018): 5728-5742.

[146] Yi, Zhijun, and Zhou Fang. "Theoretical studies on the structural, electronic and optical properties of orthorhombic perovskites CH3NH3PbX3 (X= I, Br, Cl)." *Journal of Physics and Chemistry of Solids* 110 (2017): 145-151.

[147] Burschka, Julian, et al. "Sequential deposition as a route to high-performance perovskite-sensitized solar cells." *Nature* 499.7458 (2013): 316-319.

[148] Lee, June Ho, et al. "The nature of hydrogen-bonding interaction in the prototypic hybrid halide perovskite, tetragonal CH3NH3PbI3." *Scientific reports* 6.1 (2016): 1-12.

[149] Salehi, Hamdollah, and Hosein Tolabinejad. "First-principles study of the optical properties of SrHfO3." *Optics and Photonics Journal* 1.2 (2011): 75-80.

[150] Arar, R., et al. "Structural, mechanical and electronic properties of sodium based fluoroperovskites NaXF3 (X= Mg, Zn) from first-principle calculations." *Materials Science in Semiconductor Processing* 33 (2015): 127-135.

[151] Khan, Banaras, et al. "Structural and thermoelectric properties of pure and La, Y doped HoMnO3 for their use as alternative energy materials." *Computer Physics Communications* 187 (2015): 1-7.

[152] Diao X-F, Tang Y-L and Xie Q 2019 Theoretical Analysis of Organic–Inorganic Metal Halide Perovskite Materials for Solar Cell *J. Nanoelectron. Optoelectron.* **14** 456–63

[153] Zhu, Sinan, et al. "Optical properties of photovoltaic materials: Organic-inorganic mixed halide perovskites CH3NH3Pb (I1-yXy) 3 (X= Cl, Br)." *Computational and Theoretical Chemistry* 1144 (2018): 1-8.

[154] Kojima, Akihiro, et al. "Highly luminescent lead bromide perovskite nanoparticles synthesized with porous alumina media." *Chemistry Letters* 41.4 (2012): 397-399.

[155] Etgar, Lioz, et al. "Mesoscopic CH3NH3PbI3/TiO2 heterojunction solar cells." *Journal of the American Chemical Society* 134.42 (2012): 17396-17399.

[156] Blaha, Peter, et al. "Full-potential, linearized augmented plane wave programs for crystalline systems." *Computer physics communications* 59.2 (1990): 399-415.

[157] Perdew, John P. "Generalized gradient approximations for exchange and correlation: A look backward and forward." *Physica B: Condensed Matter* 172.1-2 (1991): 1-6.

[158] Kawamura, Yukihiko, Hiroyuki Mashiyama, and Katsuhiko Hasebe. "Structural study on cubic-tetragonal transition of CH 3 NH 3 PbI 3." *Journal of the Physical Society of Japan* 71.7 (2002): 1694-1697.

[159] Oku, Takeo. "Crystal structures of CH3NH3PbI3 and related perovskite compounds used for solar cells." *Solar Cells-New Approaches and Reviews* 1 (2015).

[160] Baikie, Tom, et al. "Synthesis and crystal chemistry of the hybrid perovskite (CH3NH3)PbI3 for solid-state sensitised solar cell applications." *Journal of Materials Chemistry A* 1.18 (2013): 5628-5641.

[161] Stamplecoskie, Kevin G., Joseph S. Manser, and Prashant V. Kamat. "Dual nature of the excited state in organic–inorganic lead halide perovskites." *Energy & Environmental Science* 8.1 (2015): 208-215.

[162] Jishi, Radi A., Oliver B. Ta, and Adel A. Sharif. "Modeling of lead halide perovskites for photovoltaic applications." *The Journal of Physical Chemistry C* 118.49 (2014): 28344-28349.

[163] Shirayama, Masaki, et al. "Optical transitions in hybrid perovskite solar cells: ellipsometry, density functional theory, and quantum efficiency analyses for CH 3 NH 3 PbI 3." *Physical Review Applied* 5.1 (2016): 014012.

[164] Xing, Guichuan, et al. "Low-temperature solution-processed wavelength-tunable perovskites for lasing." *Nature materials* 13.5 (2014): 476-480.

[165] Ball, James M., et al. "Optical properties and limiting photocurrent of thin-film perovskite solar cells." *Energy & Environmental Science* 8.2 (2015): 602-609.

[166] Shi-Ming, Liu, et al. "InxGa1− xN/GaN multiple quantum well solar cells with conversion efficiency of 3.77%." *Chinese Physics Letters* 32.8 (2015): 088401.

[167] Konovalov, Igor, and Vitali Emelianov. "Hot carrier solar cell as thermoelectric device." *Energy Science & Engineering* 5.3 (2017): 113-122.

[168] Tavakoli, Mohammad Mahdi, et al. "Fabrication of efficient planar perovskite solar cells using a one-step chemical vapor deposition method." *Scientific reports* 5.1 (2015): 1-9.

[169] Abbas, Hisham A., et al. "High efficiency sequentially vapor grown nip CH3NH3PbI3 perovskite solar cells with undoped P3HT as p-type heterojunction layer." *APL materials* 3.1 (2015): 016105.

[170] Jahandar, Muhammad, et al. "High-performance CH3NH3PbI3-inverted planar perovskite solar cells with fill factor over 83% via excess organic/inorganic halide." *ACS applied materials & interfaces* 9.41 (2017): 35871-35879.

[171] Gueymard, Christian A. "The sun's total and spectral irradiance for solar energy applications and solar radiation models." *Solar energy* 76.4 (2004): 423-453.

[172] Lin, Qianqian, et al. "Electro-optics of perovskite solar cells." *Nature Photonics* 9.2 (2015): 106-112.

[173] Qarony, Wayesh, et al. "Optical analysis in CH3NH3PbI3 and CH3NH3PbI2Cl based thin-film perovskite solar cell." *Am. J. Energy Res* 3.2 (2015): 19-24.

[174] Umari, Paolo, Edoardo Mosconi, and Filippo De Angelis. "Relativistic GW calculations on CH3NH3PbI3 and CH3NH3SnI3 perovskites for solar cell applications." *Scientific reports* 4.1 (2014): 1-7.

[175] Stoumpos, Constantinos C., Christos D. Malliakas, and Mercouri G. Kanatzidis. "Semiconducting tin and lead iodide perovskites with organic cations: phase transitions, high mobilities, and near-infrared photoluminescent properties." *Inorganic chemistry* 52.15 (2013): 9019-9038.

[176] Quarti, Claudio, et al. "Structural and optical properties of methylammonium lead iodide across the tetragonal to cubic phase transition: implications for perovskite solar cells." *Energy & Environmental Science* 9.1 (2016): 155-163.

[177] Amat, Anna, et al. "Cation-induced band-gap tuning in organohalide perovskites: interplay of spin–orbit coupling and octahedra tilting." *Nano letters* 14.6 (2014): 3608-3616

[178] Zhu, Xi, et al. "Computed and experimental absorption spectra of the perovskite CH3NH3PbI3." *The journal of physical chemistry letters* 5.17 (2014): 3061-3065.

[179] Santoni, Marie-Pierre, Garry S. Hanan, and Bernold Hasenknopf. "Covalent multi-component systems of polyoxometalates and metal complexes: Toward multi-functional organic–inorganic hybrids in molecular and material sciences." *Coordination Chemistry Reviews* 281 (2014): 64-85.

[180] Lu, Ting, et al. "Four Strandberg-type polyoxometalates with organophosphine centre decorated by transition metal-2, 2'-bipy/H2O complexes." *Journal of Solid State Chemistry* 253 (2017): 52-57.

[181] Kurth, Dirk G., et al. "Biologically inspired polyoxometalate–surfactant composite materials. Investigations on the structures of discrete, surfactant-encapsulated clusters, monolayers, and Langmuir–Blodgett films of (DODA) 40 (NH 4) 2 [(H 2 O) n⊂ Mo 132 O 372 (CH 3 CO 2) 30 (H 2 O) 72]." *Journal of the Chemical Society, Dalton Transactions* 21 (2000): 3989-3998.

[182] Coronado, Eugenio, Carlos Giménez-Saiz, and Carlos J. Gómez-García. "Recent advances in polyoxometalate-containing molecular conductors." *Coordination Chemistry Reviews* 249.17-18 (2005): 1776-1796.

[183] Hasenknopf, Bernold. "Polyoxometalates: introduction to a class of inorganic compounds and their biomedical applications." *Front. Biosci* 10.275 (2005): 10-2741.

[184] Wang, Xiang, et al. "Two polyoxomolybdate-tuned hybrids composed of tripodal star-like ligand copper complexes." *Inorganica Chimica Acta* 392 (2012): 160-164.

[185] Dimitris, E. K. "A survey of application of polyoxometalates." *Chem. Rev* 98.1 (1998): 359.

[186] Clemente-Juan, Juan M., Eugenio Coronado, and Alejandro Gaita-Ariño. "Magnetic polyoxometalates: from molecular magnetism to molecular spintronics and quantum computing." *Chemical Society Reviews* 41.22 (2012): 7464-7478.

[187] Lyxell, D-G., and R. Strandberg. "The structure of tetraguanidinium pentamolybdodiphenylphosphonate." *Acta Crystallographica Section C: Crystal Structure Communications* 44.9 (1988): 1535-1538.

[188] Song, Yu-Fei, and Ryo Tsunashima. "Recent advances on polyoxometalate-based molecular and composite materials." *Chemical Society Reviews* 41.22 (2012): 7384-7402.

[189] Shestimerova, Tatiana A., and Andrei V. Shevelkov. "Metal-inorganic frameworks with pnictogen linkers." *Russian Chemical Reviews* 87.1 (2018): 28.

[190] You, Zhuchai, et al. "Synthesis, structure and character of three new Strandberg type molybdophenylphosphonates." *Inorganica Chimica Acta* 421 (2014): 160-168.

[191] Wang, Shi-Ming, Jongun Hwang, and Eunkyoung Kim. "Polyoxometalates as promising materials for electrochromic devices." *Journal of Materials Chemistry C* 7.26 (2019): 7828-7850.

[192] Pradeep, Chullikkattil P., De-Liang Long, and Leroy Cronin. "Cations in control: crystal engineering polyoxometalate clusters using cation directed self-assembly." *Dalton Transactions* 39.40 (2010): 9443-9457.

[193] Ammam, Malika. "Polyoxometalates: formation, structures, principal properties, main deposition methods and application in sensing." *Journal of Materials Chemistry A* 1.21 (2013): 6291-6312.

[194] Ma, Ying, et al. "Hydrothermal synthesis and crystal structure of a novel three-dimensional supramolecular network containing cyclic water hexamers:[Co (en) 3] 4 [P2Mo5O23] 2· 9H2O (en= ethylenediamine)." *Journal of molecular structure* 784.1-3 (2006): 18-23.

[195] Kuznetsov, Aleksey E., et al. "Dioxygen and water activation processes on multi-ru-substituted polyoxometalates: comparison with the "blue-dimer" water oxidation catalyst." *Journal of the American Chemical Society* 131.19 (2009): 6844-6854.

[196] Nishimoto, Yoshio, et al. "Super-reduced polyoxometalates: excellent molecular cluster battery components and semipermeable molecular capacitors." *Journal of the American Chemical Society* 136.25 (2014): 9042-9052.

[197] H. Yoshikawa, K. Awaga, 1358. Agawa-ja12-POM EXAFS.pdf, (2012).

[198] Macht, Josef, et al. "Catalytic consequences of composition in polyoxometalate clusters with Keggin structure." *Angewandte Chemie* 119.41 (2007): 8010-8014.

[199] Kawasaki, Naoya, et al. "Nanohybridization of polyoxometalate clusters and single-wall carbon nanotubes: applications in molecular cluster batteries." *Angewandte Chemie* 123.15 (2011): 3533-3536.

[200] Upreti, Shailesh, and A. Ramanan. "Role of hydrogen-bonded interactions in the crystal packing of phenylenediammonium phosphomolybdates." *Crystal growth & design* 6.9 (2006): 2066-2071.

[201] Yoon, Minjoong, et al. "Heteropoly acid-incorporated TiO2 colloids as novel photocatalytic systems resembling the photosynthetic reaction center." *The Journal of Physical Chemistry B* 105.13 (2001): 2539-2545.

[202] Ozer, Ruya R., and John L. Ferry. "Investigation of the photocatalytic activity of TiO2− polyoxometalate systems." *Environmental science & technology* 35.15 (2001): 3242-3246.

[203] Parayil, Sreenivasan Koliyat, Yu Min Lee, and Minjoong Yoon. "Photoelectrochemical solar cell properties of heteropolytungstic acid-incorporated TiO2 nanodisc thin films." *Electrochemistry communications* 11.6 (2009): 1211-1216.

[204] Bridgeman, Adam J., and Germán Cavigliasso. "Electronic structure of Mo and W [M 7 O 24] 6− isopolyanions." *Journal of the Chemical Society, Dalton Transactions* 10 (2002): 2244-2249.

[205] Spanopoulos, Ioannis, et al. "Unraveling the chemical nature of the 3D "hollow" hybrid halide perovskites." *Journal of the American Chemical Society* 140.17 (2018): 5728-5742.

[206] López, Xavier, et al. "Structure, properties and reactivity of polyoxometalates: a theoretical perspective." *Chemical Society Reviews* 41.22 (2012): 7537-7571.

[207] López, X., et al. "Electronic and Magnetic Properties of α-Keggin Anions: A DFT Study of [XM 12 O 40] n-,(M= W, Mo; X= Al III, Si IV, P V, Fe III, Co II, Co III) and [SiM 11 VO 40] m-(M= Mo and W)." *J. Am. Chem. Soc* 123 (2001): 3749-3758.

[208] Ammari, Y., et al. "Structure, optical and magnetic properties of a novel homometallic coordination polymers: Experimental and Computational studies." *Scientific reports* 10.1 (2020): 1-12.

[209] Kaminsky, Werner. "From CIF to virtual morphology using the WinXMorph program." *Journal of Applied Crystallography* 40.2 (2007): 382-385.

[210] Herzfeld, Karl F., and Maria Goeppert-Mayer. "On the theory of dispersion." *Physical Review* 49.4 (1936): 332.

[211] Toll, John S. "Causality and the dispersion relation: logical foundations." *Physical review* 104.6 (1956): 1760.

[212] Hassanien, A. S., and Alaa A. Akl. "Effect of Se addition on optical and electrical properties of chalcogenide CdSSe thin films." *Superlattices and Microstructures* 89 (2016): 153-169.

[213] Hassanien, Ahmed Saeed, K. A. Aly, and Alaa A. Akl. "Study of optical properties of thermally evaporated ZnSe thin films annealed at different pulsed laser powers." *Journal of Alloys and Compounds* 685 (2016): 733-742.

[214] Mott, Nevill Francis, and Edward A. Davis. *Electronic processes in non-crystalline materials*. Oxford university press, 2012.

[215] Banerjee, B. K. "On a generalised approach to first and second order magnetic transitions." *Physics letters* 12.1 (1964): 16-17.

[216] Arrott, Anthony, and John E. Noakes. "Approximate equation of state for nickel near its critical temperature." *Physical Review Letters* 19.14 (1967): 786.

[217] Ding, N., G. S. Armatas, and M. G. Kanatzidis. "Metal inorganic frameworks: dynamic flexible architecture with extended pore order built from [Se {sub 3}]{sup 2-} linkers and [Re {sub 6} Se {sub 6} Br {sub 8}]{sup 2-} clusters." *J. Am. Chem. Soc.* 132.ANL/MSD/JA-69076 (2010).

[218] Shestimerova, Tatiana A., and Andrei V. Shevelkov. "Metal-inorganic frameworks with pnictogen linkers." *Russian Chemical Reviews* 87.1 (2018): 28.

[219] Tian, Chongbin, Huabin Zhang, and Shaowu Du. "Acentric and chiral heterometallic inorganic–organic hybrid frameworks mediated by alkali or alkaline earth ions: synthesis and NLO properties." *CrystEngComm* 16.20 (2014): 4059-4068.

[220] Pch SO, Co CH, Stock N, et al(2000) The hybrid open-framework of tin (II) phosphonopropionate oxalate ,. 4:2277–2278. https://doi.org/10.1039/b006511k.

[221] Gao, Yue-Qiang, et al. "Syntheses, Structures and Magnetic Behaviours of two Mixed-Metal Inorganic-Organic Hybrid Frameworks with N-(Phosphonomethyl) iminodiacetate." *Zeitschrift für anorganische und allgemeine Chemie* 634.11 (2008): 1961-1964.

[222] Singh, N. B., et al. "Nonlinear optical characteristics of binary organic system." *Journal of crystal growth* 128.1-4 (1993): 976-980.

[223] Rajasekaran, R., et al. "Growth and characterization of zinc thiourea chloride (ZTC): a semiorganic nonlinear optical crystal." *Journal of crystal growth* 229.1-4 (2001): 563-567.

[224] Peh, Shing Bo, and Dan Zhao. "Synthesis and development of metal–organic frameworks." *Nanoporous Materials for Molecule Separation and Conversion*. Elsevier, 2020. 3-43.

[225] Li, S. L., and Q. Xu. "Metal-organic frameworks as solid magnesium electrolytes." *Energy Environ. Sci* 6 (2013): 1656-1683.

[226] Baaalla, N., et al. "Study of optical, electrical and photovoltaic properties of CH3NH3PbI3 perovskite: ab initio calculations." *Physica Scripta* 95.9 (2020): 095104.

[227] Adler-Abramovich, Lihi, and Ehud Gazit. "The physical properties of supramolecular peptide assemblies: from building block association to technological applications." *Chemical Society Reviews* 43.20 (2014): 6881-6893.

[228] Nilsson, K. Peter R., et al. "Self-assembly of synthetic peptides control conformation and optical properties of a zwitterionic polythiophene derivative." *Proceedings of the National Academy of Sciences* 100.18 (2003): 10170-10174.

[229] Dong, Xu, Jiang Min-Hua, and Tan Zhong-Ke. "A new phase matchable nonlinear optical crystal—L-arginine phosphate monohydrate (LAP)." *Acta Chimica Sinica English Edition* 1.2 (1983): 230-233.

[230] Mathias, B. T., C. E. Miller, and J. P. Remeika. "Ferroelectricity of glycine sulfate." *Phys. Rev.* 104 (1956): 849-850.

[231] Bergman Jr, J. G., and S. K. Kurtz. "Nonlinear optical materials." *Materials Science and Engineering* 5.5 (1970): 235-250.

[232] Meera, K., R. Muralidharan, and R. Dhanasekaran. "Prapun Manyum and Ramasamy P." *J Cryst Growth* 263.1-4 (2004): 510-516.

[233] Powers, Ian G., and Christopher Uyeda. "Metal–metal bonds in catalysis." *Acs Catalysis* 7.2 (2017): 936-958.

[234] Ence, Chloe C., et al. "Synthesis of chiral titanium-containing phosphinoamide ligands for enantioselective heterobimetallic catalysis." *Tetrahedron* 75.24 (2019): 3341-3347.

[235] Pal, Tanusri, and Tanusree Kar. "Wang. D., Cheng, X.-F. & Yang, Z.-H.(2002)." *J. Cryst. Growth* 235: 523-528.

[236] Yamauchi, Osamu, Akira Odani, and Masako Takani. "Metal–amino acid chemistry. Weak interactions and related functions of side chain groups." *Journal of the Chemical Society, Dalton Transactions* 18 (2002): 3411-3421.

[237] Valverde, Clodoaldo, et al. "Effect of the crystalline environment on the third-order nonlinear optical properties of L-arginine phosphate monohydrate: a theoretical study." *Journal of molecular modeling* 23.4 (2017): 122.

[238] Stone, Diane L., David K. Smith, and Adrian C. Whitwood. "Copper amino-acid complexes–towards encapsulated metal centres." *Polyhedron* 23.10 (2004): 1709-1717.

[239] de Farias, Robson F., Leandro Martínez, and Claudio Airoldi. "A calorimetric investigation into copper–arginine and copper–alanine solid state interactions." *Transition Metal Chemistry* 27.3 (2002): 253-255.

[240] Masuda, Hideki, et al. "Structures and stabilities of ternary copper (II) complexes containing an acidic and a basic amino acid. Evidence for arginine side chain involvement in intermolecular interactions and its biological implication." *Inorganic Chemistry* 32.7 (1993): 1111-1118.

[241] Viera, Inés, et al. "Structural and spectroscopic characterization of aqua-diargininate-copper (II) carbonate monohydrate." *Journal of inorganic biochemistry* 99.5 (2005): 1250-1254.

[242] Hemissi, Hanène, Ahmed Nasri, and Mohamed Rzaigui. "Chiral self-assembly of a novel (CuII/ReVII)-heterobimetallic l-Arginine complex: Crystal structure, Hirshfeld surface analysis, spectroscopic properties and biochemical studies." *Journal of Molecular Structure* 1186 (2019): 307-316.

[243] Schwarz, Karlheinz, Peter Blaha, and Georg KH Madsen. "Electronic structure calculations of solids using the WIEN2k package for material sciences." *Computer physics communications* 147.1-2 (2002): 71-76.

[244] Van Mourik, Tanja, Michael Bühl, and Marie-Pierre Gaigeot. "Density functional theory across chemistry, physics and biology." (2014): 20120488.

[245] Ambrosch-Draxl, Claudia, and Jorge O. Sofo. "Linear optical properties of solids within the full-potential linearized augmented planewave method." *Computer physics communications* 175.1 (2006): 1-14.

[246] Baaalla, N., et al. "The novel material based on strandberg-type hybrid complex (C6H10N2) 2 [Co (H2O) 4P2Mo5O23]. 6H2O: Experimental and simulations investigation on electronic, optical, and magnetocaloric properties." *Ceramics International* 47.2 (2021): 2338-2346.

[247] Sheik-Bahae, Mansoor, et al. "Dispersion of bound electron nonlinear refraction in solids." *IEEE Journal of quantum electronics* 27.6 (1991): 1296-1309.

[248] Christy, Alfred A., Olav M. Kvalheim, and Rance A. Velapoldi. "Quantitative analysis in diffuse reflectance spectrometry: a modified Kubelka-Munk equation." *Vibrational Spectroscopy* 9.1 (1995): 19-27.

[249] Tkalčević, Marija. *Određivanje energije zabranjene zone Taucovom metodom*. Diss. University of Zagreb. Faculty of Chemical Engineering and Technology, 2016.

[250] Syarif, Nirwan, et al. "The Effects of Grain Size, Oxidizers and Catalysts on Band Gap Energy of Gelam-Wood Carbon." *International Journal of Sustainable Transportation Technology* 2.2 (2019): 63-70.

[251] Tauc, J., Radu Grigorovici, and Anina Vancu. "Optical properties and electronic structure of amorphous germanium." *physica status solidi (b)* 15.2 (1966): 627-637.

[252] Praveen, K. H., and Arun S. Prasad. "Chrysin mediated synthesis, crystallographic structure and optical emission characteristics of ZnO nanoparticles." *Materials Today: Proceedings* 41 (2021): 590-595.

[253] Prasad, Arun S. "Green synthesis of nanocrystalline manganese (II, III) oxide." *Materials Science in Semiconductor Processing* 71 (2017): 342-347.

[254] Davis, E. A., and NFf Mott. "Conduction in non-crystalline systems V. Conductivity, optical absorption and photoconductivity in amorphous semiconductors." *Philosophical magazine* 22.179 (1970): 0903-0922.

[255] Coulter, Jennifer B., and Dunbar P. Birnie III. "Assessing Tauc plot slope quantification: ZnO thin films as a model system." *physica status solidi (b)* 255.3 (2018): 1700393.

[256] Yuan, Changzhou, et al. "Mixed transition-metal oxides: design, synthesis, and energy-related applications." *Angewandte Chemie International Edition* 53.6 (2014): 1488-1504.

[257] Yang, Zhenguo Gary. "Electrochemical Energy Storage for Green Grid: Status and Challenges." *ECS Meeting Abstracts*. No. 4. IOP Publishing, 2011.

[258] Cook, Timothy R., et al. "Solar energy supply and storage for the legacy and nonlegacy worlds." *Chemical reviews* 110.11 (2010): 6474-6502.

[259] Tan, Hui Teng, et al. "2D transition metal oxides/hydroxides for energy-storage applications." *ChemNanoMat* 2.7 (2016): 562-577.

[260] Rešček, Ana, et al. "Development of double-layered PE/PCL films for food packaging modified with zeolite and magnetite nanoparticles." *Advances in Polymer Technology* 37.3 (2018): 837-842.

[261] Bodurov, Georgi, Tatyana Ivanova, and Kostadinka Gesheva. "Technology and application of transition metal oxide of WVO as functional layers and NiO thin films as counter electrode material in electrochromic “Smart Windows”." *Physics Procedia* 46 (2013): 149-158.

[262] Qu, Bingyan, et al. "How to predict the location of the defect levels induced by 3d transition metal ions at octahedral sites of aluminate phosphors." *Journal of Materials Chemistry C* 7.1 (2019): 95-103.

[263] Wei, Wei, et al. "Transition metal oxide hierarchical nanotubes for energy applications." *Nanotechnology* 27.2 (2015): 02LT01.

[264] Lee, Jeongjae, et al. "A systematic study of 25 Mg NMR in paramagnetic transition metal oxides: applications to Mg-ion battery materials." *Physical Chemistry Chemical Physics* 19.1 (2017): 613-625.

[265] Shao, Yuyan, et al. "Electrocatalysts for nonaqueous lithium–air batteries: status, challenges, and perspective." *Acs Catalysis* 2.5 (2012): 844-857.

[266] Whangbo, M. H. "Science 252 96 Crossref PubMed Google Scholar Canadell E and Whangbo M 1990." *Phys. Rev. B* 43 (1991): 1894.

[267] Tokito, Shizuo, Koji Noda, and Yasunori Taga. "Metal oxides as a hole-injecting layer for an organic electroluminescent device." *Journal of Physics D: Applied Physics* 29.11 (1996): 2750.

[268] Simon, Patrice, and Yury Gogotsi. "Materials for electrochemical capacitors." *Nanoscience and technology: a collection of reviews from Nature journals* (2010): 320-329.

[269] Manthiram, A. V. M. A., et al. "Nanostructured electrode materials for electrochemical energy storage and conversion." *Energy & Environmental Science* 1.6 (2008): 621-638.

[270] Gautam, Gopalakrishnan Sai, and Emily A. Carter. "Evaluating transition metal oxides within DFT-SCAN and SCAN+ U frameworks for solar thermochemical applications." *Physical Review Materials* 2.9 (2018): 095401.

[271] Goodenough, John B., and Kyu-Sung Park. "The Li-ion rechargeable battery: a perspective." *Journal of the American Chemical Society* 135.4 (2013): 1167-1176.

[272] Wang, Wei, et al. "Progress in solid oxide fuel cells with nickel-based anodes operating on methane and related fuels." *Chemical reviews* 113.10 (2013): 8104-8151.

[273] Ulutagay-Kartin, M., Etheredge, K. M., Schimek, G. L., & Hwu, S. J. (2002). Synthesis, structure, and magnetic properties of two quasi-low-dimensional antiferromagnets, NaMnAsO4 and β-NaCuPO4. *Journal of alloys and compounds*, *338*(1-2), 80-86.

[274] Weil, Matthias, and Théo Veyer. "A new form of NaMnAsO4." *Acta Crystallographica Section E: Crystallographic Communications* 75.7 (2019): 969-971.

[275] Absike, H., et al. "Strain effects on the electronic and thermoelectric properties of copper oxide." *Computational Condensed Matter* 16 (2018): e00322.

[276] Hajji, M., et al. "Strain effects on the electronic and thermoelectric properties of Bi2Te3: A first principles study." *Computational Condensed Matter* 16 (2018): e00299.

[277] mana Al-anazy, M., Zelai, T., Rahim, A., AlObaid, A. A., Al-Muhimeed, T. I., Aljameel, A. I., ... & Nazir, G. (2021). First principle study of optoelectronic and thermoelectric properties of magnesium based MgX2O4 (X= Sb, Bi) spinels. *Journal of Solid State Chemistry*, *303*, 122480.

[278] Li, Wu, et al. "ShengBTE: A solver of the Boltzmann transport equation for phonons." *Computer Physics Communications* 185.6 (2014): 1747-1758.

[279] Lucarini, V., Saarinen, J. J., Peiponen, K. E., & Vartiainen, E. M. (2005). *Kramers-Kronig relations in optical materials research* (Vol. 110). Springer Science & Business Media.

[280] Ambrosch-Draxl, Claudia, and Jorge O. Sofo. "Linear optical properties of solids within the full-

potential linearized augmented planewave method." *Computer physics communications* 175.1 (2006): 1-14.

[281] Kumar, Sachin, et al. "DFT investigations on optoelectronic spectra and thermoelectric properties of barium cadmium disulphide (BaCdS2)." *Optik* 207 (2020): 163797.

[282] Hutchings, D. Crichton, et al. "Kramers-Krönig relations in nonlinear optics." *Optical and Quantum Electronics* 24.1 (1992): 1-30.

[283] DONCEAN, Gheorghe. "COLORIMETRIC CHARACTERISATION OF TRICHROMATIC RGB DIGITAL IMAGES. II. CIE COLORIMETRIC CHARACTERISTICS." *Agronomy Series of Scientific Research/Lucrari Stiintifice Seria Agronomie* 56.2 (2013).

[284] Xu, Qianqian, et al. "Temperature-dependent luminescence properties of lanthanide (III) β-diketonate complex-doped LAPONITE®." *Photochemical & Photobiological Sciences* 15.3 (2016): 405-411.

[285] Hao, Qing, Dongchao Xu, and Hongbo Zhao. "Computation-Driven Materials Search for Thermoelectric Applications." *ECS Journal of Solid State Science and Technology* 6.3 (2017): N3095.

[286] Absike, H., et al. "Ab initio calculations on electronic, optical, and thermoelectric properties of (Si, Pb)(co)-doped ZnS for solar cell device applications." *Journal of Physics and Chemistry of Solids* 132 (2019): 10-17.

Abstract

Organic-inorganic hybrid materials and transition metal oxide materials have attracted intensive interest due to their multifunctional properties. This present thesis work was focused on well-understanding the different properties of these materials. We have explored the possibilities of organic-inorganic hybrids and transition metal oxide materials for diverse applications such as photovoltaics and optoelectronic devices. Those materials could be of interest for applications in cheap and printable single-use electronics that require both data storage and data processing. Moreover, this combination of unique parameters is rarely observed in conventional materials and is, therefore, also from a fundamental point of view, an interesting place to start the exploration of the field of organic-inorganic hybrids and transition metal materials.

This thesis is of scientific interest and considers a study of the correlation between the electronic structure of materials and their efficiency in a photovoltaic device. By calculating the open-circuit voltage V_{oc} and the short circuit current J_{sc} with the density functional theory. This new method opens the possibility to rapidly estimate the efficiency of a given material without the necessity to realize a photovoltaic device as well as to optimize the size of an already existing photovoltaic device.

The first part of this thesis deals with the modeling of the structural, electronic, and optical properties of hybrid organic-inorganic materials. The calculations are based on the ab-initio method within the framework of the density functional (DFT) implemented in the WIEN2K code. The results found are in agreement with the experimental measurements. This demonstrates that these materials are promising in optoelectronic and photovoltaic applications.

The objective of the second part of this thesis is to study the electronic, optical, magnetic and thermoelectric properties of sodium manganese (II) arsenate $NaMnAsO_4$ using DFT. The density of state, as well as the band structure calculation, revealed that the studied material can be identified as a ferromagnetic semiconductor. Optical properties show that $NaMnAsO_4$ has potential application in optoelectronics. The electrical conductivity obtained as well as the figure of merit suggests that this material could be new potential for an optoelectronic-thermoelectric device

Keywords: Organic- Inorganic hybrid, Transition metal TM-oxide, DFT, electronic and optical properties, thermo-electrical properties, DFT, BoltzTraP

Résumé

Les matériaux hybrides organiques-inorganiques et les oxydes de métal de transition ont suscité un vif intérêt en raison de leurs propriétés multifonctionnelles. Ce présent travail de thèse s'est concentré sur la compréhension des différentes propriétés de ces matériaux. Nous avons exploré les possibilités des hybrides organiques-inorganiques et des matériaux d'oxyde de métaux de transition pour diverses applications telles que le photovoltaïque et les dispositifs optoélectroniques. Ces matériaux pourraient être intéressants pour des applications dans des appareils électroniques à usage unique et imprimables qui nécessitent à la fois le stockage et le traitement de données. De plus, cette combinaison de paramètres est rarement observée dans les matériaux conventionnels, et constitue donc d'un point de vue fondamental également, un point de départ pour commencer l'exploration du domaine des hybrides organiques-inorganiques et des matériaux de métaux de transition.

Cette thèse est d'intérêt scientifique et envisage une étude de la corrélation entre la structure électronique des matériaux et leur efficacité dans un dispositif photovoltaïque. En calculant la tension en circuit ouvert V_{oc} et le courant de court-circuit J_{sc} avec la théorie fonctionnelle de la densité. Cette nouvelle méthode ouvre la possibilité d'estimer rapidement l'efficacité d'un matériau donné sans qu'il soit nécessaire de réaliser un dispositif photovoltaïque ainsi que d'optimiser la taille d'un dispositif photovoltaïque déjà existant.

La première partie de cette thèse porte sur la modélisation des propriétés structurales, électroniques et optiques de matériaux hybrides organiques-inorganiques. Les calculs sont basés sur la méthode ab-initio dans le cadre de la fonctionnelle de densité (DFT) implémentée dans le code WIEN2K. Les résultats trouvés sont en accord avec les mesures expérimentales. Cela démontre que ces matériaux sont prometteurs dans les applications optoélectroniques et photovoltaïques.

L'objectif de la deuxième partie de cette thèse est d'étudier les propriétés électroniques, optiques, magnétiques et thermoélectriques de l'arséniate de sodium manganèse (II) $NaMnAsO_4$ à l'aide de la DFT. La densité d'état, ainsi que le calcul de la structure de bande, ont révélé que le matériau étudié peut être identifié comme un semi-conducteur ferromagnétique. Les propriétés optiques montrent que $NaMnAsO_4$ a une application potentielle en optoélectronique. La conductivité électrique obtenue ainsi que le facteur de mérite suggèrent que ce matériau pourrait être un nouveau potentiel pour un dispositif optoélectronique-thermoélectrique.

Mots-clés : Les matériaux Hybride organiques-inorganiques, les matériaux d'oxyde de métal de transition, DFT, propriétés électroniques, propriétés optiques, propriétés thermoélectriques, BoltzTraP.